Morphological Computation in Active Haptic Embodied Perception

Sornkarn, Nantachai

Awarding institution:
King's College London

Morphological Computation in Active Haptic Embodied Perception

Nantachai Sornkarn

Supervisor: Dr Thrishantha Nanayakkara

Department of Informatics, Faculty of Natural and Mathematical Science

King's College London

This dissertation is submitted for the degree of

Doctor of Philosophy

King's College London December 2016

I would like to dedicate this thesis to my loving parents ...

Declaration

I hereby declare that except where specific reference is made to the work of others, the contents of this dissertation are original and have not been submitted in whole or in part for consideration for any other degree or qualification in this, or any other university. This dissertation is my own work and contains nothing which is the outcome of work done in collaboration with others, except as specified in the text and Acknowledgements.

Nantachai Sornkarn

December 2016

Acknowledgements

First of all, I would like to express my sincere appreciation and special gratitude to my supervisor Dr. Thrishantha Nanayakkara, who has been extremely patient with my development towards this degree for the past years. I would like to thank you for your advice in both academic and personal matters. Your encouragement, support, and opportunities have been priceless. You have inspired me in many aspects in life. I would not have come this far without your support. I would also like to thank Prof. Kaspar Althoefer and Prof. Prokar Dasgupta for their support throughout. I would like to also thank Dr Helmut Hauser and Dr Giuseppe Carbone for accepting to review my thesis and be my examiners.

I am thankful to all my colleagues Allen Jiang, Dr. Anuradha Ranasinghe, Dr. Dimitri Ognibene, Sara Adela Abad Guamán, Dhireshan Gadiagellan, Brendan Michael, Ashraf Weheliye, Hasitha Wegiriya, Junghwan Back, Giuseppe Cotugno, Jelizaveta Konstantinova Yohan Noh, Ali Shiva, Hadi Sadati, Elham Hamid, Angela Fragasso, and others in Thrish lab and CoRE at King's College London, who have been very helpful, supportive, and encouraging. Also, I would like to thank all my friends here in the United Kingdom, who have been supporting and enduring me for the past years. I would like to express my special thanks to Dr Kiattisak Tangrungreungyoo, Napadanai Chatrabhuti, and Pimpimon Pattanavimon who always believe in me and have been very supportive.

A special thanks to my family. Words cannot express how grateful I am to my mother, Pathita Sornkarn, my father, Karan Sornkarn, and my family for all of the sacrifices that you've made on my behalf. Especially, my deepest gratitude goes to my younger brother, Nitiphat Sornkarn for your moral support, constant enthusiasm, happiness, and inspiration throughout my life. I feel so blessed having you as my brother.

Abstract

This thesis presents a study on the role of internal impedance control in embodied perception. This study gives a novel perspective on how action and perception are coupled in a shared embodiment like a tendon in muscles used for both action and perception.

The mode of perception discussed in this thesis is the sense of touch or "haptic perception" of both human and biologically inspired artificial systems. Firstly, this thesis explores the internal impedance control behavior of humans in haptic exploration during manual palpation of a soft phantom (presented by a soft silicone phantom) to detect and estimate the depth of an abnormality (presented by a hard nodule). The muscle actuation levels of humans were measured across human subjects to learn the pattern of such regulations. It was found that humans perform voluntary modulation of muscle co-contraction level during haptic exploration of a soft tissue. In addition, it was found that these regulations of muscle co-contraction can be learned and mapped using a Markov decision matrix. This raised the question, which became the main focus of this thesis, as to why humans perform such regulations of muscle co-contraction levels during haptic exploration. The influence of proprioceptive information and the muscular activity on the interpretation of the environment during haptic exploration is not understood yet. Therefore, the objective of this thesis is to understand the role of internal impedance and behavioral variables control during embodied sensing and haptic exploration.

Secondly, it was found using a robotic manipulator with variable joint stiffness that the information-gain of the perception of its internal state can be maximized by controlling the joint's stiffness (internal impedance). This leads to an enhanced accuracy in the estimation of its internal state. It was also found that the sensing of external environment, in this case,

through haptic perception during robotic palpation could also benefit from this principle. The information gain about the environment can be maximized through the modulation of the internal stiffness.

Thirdly, a Bayesian inference mechanism was used in addition to the information metrics in the robotic palpation task to infer real-time estimates of the depth of abnormality in soft silicone phantom based on past experience. The stiffness control pattern found in human's manual palpation was implemented in the robotic probe to investigate whether controlling the probe's internal impedance to follow the transition patterns of human's co-contraction levels can enhance the nodule depth estimation accuracy. In comparison to the static stiffness; it was shown that this strategy of stiffness control in the robotic probe significantly improved the estimation accuracy of hard nodule's depth.

Lastly, this thesis also investigated both individual and collective roles of robotic probe's internal stiffness, indentation level, and probe sweeping speed in the estimation of the nodule's depth during haptic exploration. The results from the experiments have confirmed the hypothesis that by allowing the probe to vary its internal stiffness and behavioral variables, the estimation process can enhance the accuracy in haptic perception. Using artificial system as an abstraction of biological counterparts, this thesis has, for the first time, explained the possible reason as to why biological systems, humans, for instance, actuate both internal parameter (like stiffness of the joint) and the behavioral variables during haptic exploration of the environment.

Table of contents

List of figures

List of tables

Nomenclature

Acronyms / Abbreviations

ABS Acrylonitrile butadiene styrene plastic

ANOVA Analysis of variance

DTS Desktop direct transmission system

EDC Extensor digitorum communis

EMG Electromyography

EP Exploratory process

F/T Force/torque

FDS Flexor digitorum superficialis

MCP Metacarpophalangea

MVC Maximum voluntary contraction

RMIS Robot-assisted minimally invasive surgery

RMS Root-mean-square

SEA Series Elastic Actuator

VSJ Variable stiffness joint

PSV Probe sweeping velocity

Chapter 1

Introduction and motivation

Abstract—*Internal impedance is one of the key factors determining the quality of embodied perception and action in biological organisms and robots. Though the role of impedance control in robotic actuation has been well studied, its significance in the accuracy of proprioception with embodied sensors is not well known yet. If the relationship between the entropy of sensory information and the internal impedance as well as behavioral variable control are well understood, a better artificial perception system, especially for haptic perception in robotic applications, can be designed. Therefore, it is important to characterize the relationship between the entropy of sensory information and the impedance of their physical embodiment, through which sensors feel the internal state of the body and the environment. This thesis explores how humans control their internal impedance in haptic exploration and investigates how this similar behavior can be implemented in an artificial system like a robotic probes for physical examination of soft objects.*

1.1 Introduction

During interaction with the external environment, biological systems, like humans, perceive the information about the environment through biological sensory receptors and then take some desired action based on the perception. However, it is not only action or movement that requires muscle activation; but also so does proprioception. There is compelling biological evidence suggesting that humans dynamically change the level of activation of muscles, spindles, and tendons in order to condition the proprioceptive feedback during interaction with the external environment [1]. In this thesis, this is defined as "embodied sensing" or "embodied perception".

Embodied sensing in a biological system such as mechanoreceptors in the hand [2], are modulated by the physical changes of the body [3]. This in-turn influences the sensorimotor coupling network resulting in changes in behavior [1]. In fact, many sensory receptors in human are embedded or attached to the very muscles exploited for actuation. Therefore, the way the sensory receptor feels any action or movement is very much influenced by how the muscle is actuated, which leads to the change in the internal impedance (internal stiffness) of the body. The structural variation of embodied sensors is one of the most important features in biological systems, which is often used to enhance the interpretation of the perceived information of its own behavioral variables and the environment [4]. Hence, the quality of both action and perceived information are influenced by the internal impedance of the physical embodiment, which mediates both sensing and actuation. As signified in [5], it is the adaptive behaviour of the embodiment that can simplify the control of dynamic interaction with the environment. If the interplay between the proprioceptive feedback and the internal impedance states can be well described and understood, this can be skilfully utilized to maximize information gain in sensing to control underactuated robots.

Fig. 1.1 illustrates how perception and action are coupled when they share a common embodiment. In biological systems, proprioceptive sensors such as spindle sensors (sense the amount and speed of muscle contraction) and tendon sensors (sense force) are located in the very muscles that are used to actuate joints. Therefore, the way controllers in the central

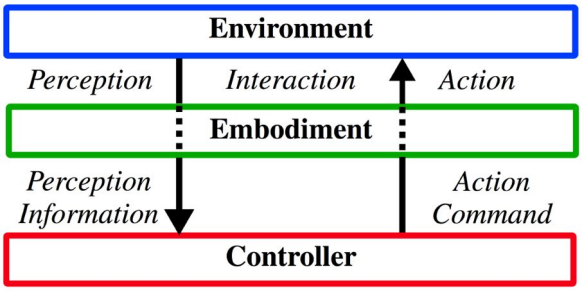

Fig. 1.1 The system interacts with the environment through its embodiment. The internal impedance required for accurate perception through its embodied sensor can differ from that required to take appropriate action. Likewise an action taken with appropriate impedance could affect the quality of perception of the environment.

nervous system perceive the environment depends on the actuation state of the muscles and muscle actuation in turn depends on perception [6]. The scope of this thesis lies around the investigation of the influence of internal impedance's regulation inside a body as well as the behavior of the agent on the perception.

1.2 Motivation

During the interaction between an agent and the environment, it is very essential for the agent, whether it is biological creature (human in particular) or an artificial system, to be able to gather and derive information from sensory data during interaction with the environment. These sensations can be classified in two different classes according to the well established Sherrington's lectures summarized in [7], namely: "exteroceptive" and "proprioceptive" sensation. The exteroceptive sensation encapsulates the sensory feedback obtained from the environment, such as: olfactory, auditory, visual, and tactile perception. On the other hand, proprioceptive sensation refers to the sensory feedback measured at musculoskeletal level delivering the information that arises due to the activation of the agent's own movement, such as: the joint's inertia, velocity, position, force, and etc.

Of all sensations available, haptic sensation (or sense of touch), although often underrated, is one of the most important sensations in humans' each and everyday life. Due to its complexity, the scientific understanding of haptic perception is unfortunately limited in

comparison to other "more apparent" senses, like hearing or vision. Haptic perception involves the intergration of the information acquired from both exteroceptive (tactile) and proprioceptive cues. In the past, the functionality of tactile perception in human has been extensively studied. Vallbo and Johanson [2, 3] have provided extensive studies on the properties and the role of the mechanoreceptors on the hand used for tactile perception. It is well understood how the afferent responses perceived through the mechanoreceptors at glabrous skin [8], containing different information, such as: force [9], shape [10], surfaces's texture [11, 12], and position, are processed and relayed to the central nervous system. To be able to perceive more complex information about the environment, such as: mechanical properties of an object, orientation of an object [13], and dynamics of continually moving environment [14], the proprioceptive cues play a very crucial role in the haptic perception. The proprioceptive information is perceived through the receptors located at the muscle spindles of the hand and arm. Therefore, the way the hand is controlled during object manipulation can influence the quality of the proprioceptive information perceived through the muscle spindles. Unfortunately, it is not yet clear how the proprioceptive information and the muscle actuation level during manipulation are correlated. Also, it is also not clear whether the regulation of the muscle could influence the proprioceptive cues and hence the haptic perception.

1.2.1 Understanding human's active haptic exploration during manual palpation

It is important to first explore the human's behavior in regulating co-contraction (muscle activity) during haptic exploration task. The active haptic exploration task discussed in this thesis is the task of physical examination of soft objects. Physical examination of soft objects to identify hidden mechanical features can be seen in a variety of areas like minimally invasive surgery, medical physical examination, security, quality assurance in food industry, entertainment, etc. When people are asked to explore a novel soft object to identify its physical properties, they regulate both apparent behaviors, such as: movement speed, force, as well as internal states like antagonistic muscle co-contraction level. It is supposed that such

behavior tries to enhance haptic perception by regulating the function of mechanoreceptors at different depths of the fingertips and proprioceptive sensors such as tendon and spindle sensors located in muscles. Hence, the interplay between motor control and internal mechanics (muscles and reflexes) [15, 16] play an important role in both action and perception [17]. The notion - *morphological computation* - in soft robotics and biological systems views the mechanical circuits in the embodiment as a computational resource for both perception and action.

1.2.2 Role of variable internal impedance in soft robotic probe for soft tissue examination

Due to the complexity of the proprioceptive sensation in haptic perception, it is not easy to understand the relationship between the voluntary regulation of muscle (muscle spindles) and the processed proprioceptive signal generated during the interaction with an object. It is also not clear as to how the regulation of proprioceptive cues could maximise the information gain perceived in active haptic exploration using a biological approach. This thesis therefore proposes to use the robotic approach to explain this. If this could be well understood, it could lead to a better understanding of how the proprioceptive information is correlated and combined with other cutaneous information in haptic perception. Furthermore, this understanding could also provide the opportunity to design, develop, and build a better artificial system, such as: biologically-inspired sensing system for robotics system.

1.3 Aims and objectives

This thesis aims to firstly understand how humans voluntarily control their proprioceptive perception through modulation of joint stiffness during active haptic exploration task like in manual palpation. The muscle co-contraction activity can be captured through the surface electromyography (EMG), which shows the level of actuation of the muscle pair responsible for controlling the stiffness of the finger joint. This thesis further explores that if such

activity can be captured, is there any control pattern in the co-contraction given different environmental variables.

In haptic perception, the role of proprioceptive cues and the regulation of the muscle spindle and tendon, in which the proprioceptors are embedded, are not well understood. In addition, the relationship between proprioceptive information and the muscle co-contraction activity cannot be easily explained using conventional biological approach. This thesis addresses this question by testing a set of hypotheses in a robotic counterpart that allows to isolate and test different phenomena. It is important to first understand the influence of internal stiffness of the variable stiffness joint manipulator on the proprioceptive sensation from a very minimalistic perspective, i.e. angular displacement of the joint. The relationship between the internal stiffness and proprioceptive information can be quantified using information gain metrics. The aim here is to explore whether the information gained of minimal proprioception can be maximised by controlling the internal stiffness; and if so, whether the haptic perception of the environment could also benefit from this. The thesis proposes the use of a robotic probe as an abstracted human finger to understand how the regulation of internal impedance affect the quality of haptic perception in manual palpation. This thesis also investigate the individual and collective role of internal impedance (internal stiffness) and the robot's behavioral variables control to understand their influences in enhancing haptic perception.

1.4 Contributions

The contributions of this thesis are:

- During human's haptic exploration for the case of manual palpation presented in this thesis, humans voluntarily modulate the stiffness of their fingers' metacarpophalangea (MCP) joint by regulating the voluntary contractions of the flexor digitorum superficialis and extensor digitorum communis muscle pair. It was found that apart from the configuration of the finger, the regulation of this muscle pair (controlling internal impedance) plays an important role in the efficacy of the active haptic exploration. This is because of that the proprioceptive sensory receptors (like tendons) are embedded in

the very muscle responsible for controlling the stiffness of the finger's joint. Therefore, the way these receptors feel the environment very much depends on the state of the muscle pair's contraction [18].

- The regulation of humans' muscle co-contraction during active haptic exploration for the case of manual palpation to estimate the depth of the nodule in a soft phantom can be extracted and learned using Markov chains. The regulation pattern given different environments can be represented in Markov state transition probability matrix. It was found that humans prefer to regulate the muscle co-contraction level in small steps within the local muscle co-contraction region over the large sudden changes. The investigation of the Eigen information of the state transition probability matrices also suggested that on average humans usually take longer time regulating the finger's stiffness (level of muscle co-contraction) during manual palpation before converging to an absorbing state when the depth of the hard nodule inside soft silicone phantom increases [18].

- This thesis has shown that humans regulate their internal impedance (finger's stiffness) during active haptic exploration of soft tissue to locate and estimate the depth of a hard nodule. However, this cannot provide definite explanation as to how the regulation of internal impedance could lead to the enhancement in the exploration and interpretation of the environment. Furthermore, it is not yet clear how the regulation of the muscular activity which modulates the prioprioceptive information could enhance the haptic perception [19]. This thesis proposes to exploit a robotic manipulator as an alternative approach to conventional biological study to explain the influence of internal impedance on the information gain in the embodied perception. It was found using the robotic manipulator with variable joint stiffness that the stiffness of the joint can be tuned in order to maximise the information gain (transfer entropy) in the estimation of the internal state of the manipulator (joint angular displacement). The results suggest that transfer entropy can be used as an indicator to search for optimal stiffness of the joint (internal impedance) in order to improve the accuracy of perception [20].

- Since the relationship between the internal impedance and the perceptual information can be used to enhance the estimation of internal state of the body through the maximization of information gain, this thesis further explores whether the estimation of the environmental variable (like the depth of hard nodule in soft silicone phantom, similar to manual palpation) can also benefit from the regulation of the internal impedance as well. This experiment used the robotic finger as an abstraction of a human finger with variable joint stiffness (representing the MCP joint) and a force sensor at the base (representing tendon sensor). Extracted humans' MCP joint stiffness control strategies in the form of Markov decision matrices were used to control the stiffness of the robotic finger under the active exploration in a Bayesian inferencing framework. It was found that the internal stiffness control plays an important role in the haptic perception. The experimental results suggest that the variation of internal stiffness of the probe leads to an improvement in the estimation of the nodule's depth embedded inside soft silicone phantom. These results provide the scientific evidence for the first time suggesting the reason as to why humans might be regulating the proprioception through the stiffness control of the muscle pair (resulting in change of finger's stiffness) that carry proprioceptive sensors [18, 21].

- It was also found that apart from the stiffness of the finger, humans also regulate probing behavioral variables during manual palpation. While it was proved using robotic approach that the internal stiffness plays an important role in haptic perception; there may also be some other behavioral factors that also contribute to the enhancement of the interpretation of the environment as well. It was found in the final experiment that allowing the combination of probe's internal impedance, indentation level, and probe's sweeping velocity to randomly vary across explorative iteration, the estimation accuracy of the nodule's depth estimation increases to almost 100% [22]. This thesis provides important explanation about the role of morphological computation in active haptic exploration of soft object in both biological system as well as in biologically-inspired artificial system.

1.5 Contributed publications

Journal publications:

- [22] **N. Sornkarn**, P. Dasgupta, and T. Nanayakkara, "Morphological computation of haptic perception of a controllable stiffness probe," PloS one, vol. 11, no. 6, p. e0156982, 2016.
- [18] **N.Sornkarn**, and T. Nanayakkara, "Can a soft robotic probe use stiffness control like a human finger to improve efficacy of haptic perception?," IEEE Transactions on Haptics, 2016.
- [23] A. Ranasinghe, **N. Sornkarn**, P. Dasgupta, K. Althoefer, J. Penders, and T. Nanayakkara, "Salient feature of haptic-based guidance of people in low visibility environments using hard reins," IEEE Transactions on Cybernetics, vol. 46, pp. 568–579, Feb 2016.

Conference proceedings:

- [20] **N. Sornkarn**, M. Howard, and T. Nanayakkara, "Internal impedance control helps information gain in embodied perception," in 2014 IEEE International Conference on Robotics and Automation (ICRA), 2014, pp. 6685–6690, May 2014.
- [21] **N. Sornkarn** and T. Nanayakkara, "The efficacy of interaction behavior and internal stiffness control for embodied information gain in haptic perception," in 2016 IEEE International Conference on Robotics and Automation (ICRA), pp. 2657–2662, May 2016.
- [24] H. B. Wegiriya, **N. Sornkarn**, H. Bedford, and T. Nanayakkara, "A Biologically Inspired Multimodal Whisker Follicle," in 2016 IEEE International Conference on Systems, Man, and Cybernatics (SMC), October 2016.
- [25] S. A. A. Guaman, **N. Sornkarn**, H., and T. Nanayakkara, "The role of morphological computation of the goat hoof in slip reduction," in 2016 IEEE/RSJ International Conference on Intelligent Robots and Systems (IROS), October 2016.

1.6 Thesis structure

The structure of this thesis is summarized in Figure 1.2

- Chapter 1 outlines the overall scope of this thesis. The motivations, objectives, and contributions of the materials presented in this thesis are discussed.
- Chapter 2 presents state of the art and current understanding under the framework outlined in this thesis. This includes the discussion of the embodiment and motor-sensory coupling in biological system. It is discussed how the knowledge and understanding of this in biological system could be employed under the context of morphological computation for action and perception. This chapter also discusses the concept of morphological computation under the context of both biology and artificial systems; and how the process of outsourcing the computation to the morphological structure occurred in nature could inspire the development of artefacts. The importance of such concept under the context of active haptic perception is also discussed. Lastly, this chapter discusses the possible implementation of this concept in a case study of haptic perception in minimally invasive surgery.
- Chapter 3 presents how humans control the internal impedance (stiffness) of the finger during haptic perception. This chapter takes the task of soft object examination (palpation) as the case study. This chapter observes the pattern of internal impedance regulation of humans given different environmental parameters.
- Chapter 4 presents the design and numerical model of the robotic manipulator and robotic probe used in the experiments presented in the later chapters in this thesis.
- Chapter 5 discusses the role of internal impedance in information gain in an embodied perception. The chapter presents the experimental results suggesting the influence of internal impedance control on the information gain in the observation of internal state variable. This chapter presents, for the first time, that non-linear static memory primitives relating internal impedance, internal kinematic variables, and forces felt at

the base of the manipulator - similar to the functionality of tendon organs of biological counterparts - can be used to tune optimal internal impedance parameters to maximize the accuracy of internal state estimation during external perturbations.

- Chapter 6 investigates under the information gain metrics framework, whether the ability for the soft robotic probe to vary its internal impedance is a necessary feature in the active exploration of the environment. Based on the directional information transfer, the results suggest that by allowing the probe to vary its stiffness, it can gain information about the environment during the explorative process. The results also signify that the soft probe is therefore preferred over the probe with rigid body.

- Chapter 7 presents a robotic probe with controllable stiffness joint and controllable behavioral variables as an abstraction of human finger in a palpation task. This chapter uses the robotic probe to explain why humans regulate the internal stiffness and behavior during manual palpation shown in Chapter 3. The pattern of humans' finger stiffness regulation extracted from Chapter 3 is implemented in the robotic probe in this chapter. The performance of active haptic perception is assessed against the passive haptic perception for the task of estimating the depth of an abnormality embedded inside a soft silicone phantom.

- Chapter 8 summarizes all the findings and contributions presented in this thesis and discuss potential applications and future works under the framework outlined in this thesis.

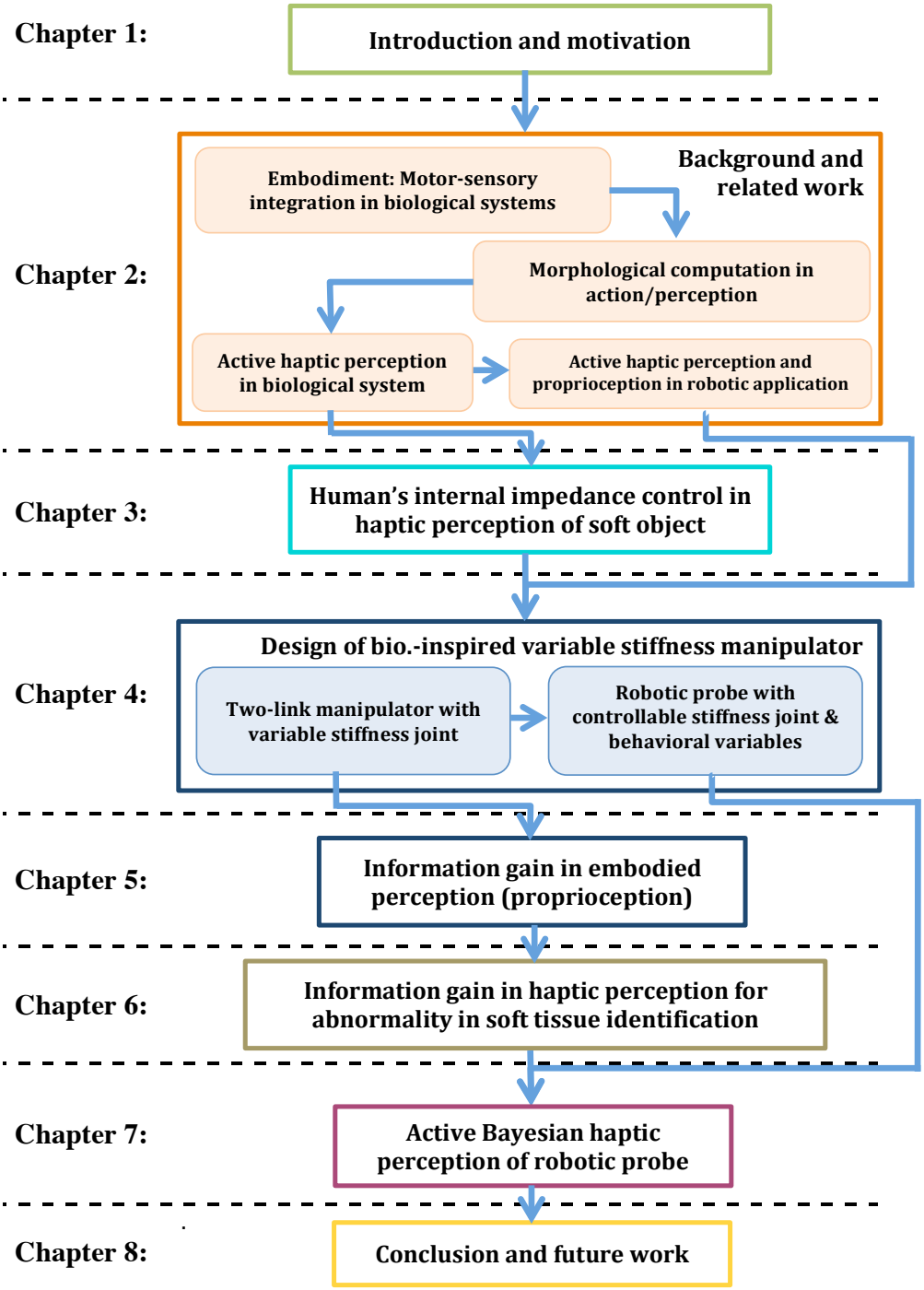

Fig. 1.2 Thesis outline

Chapter 2

Background and related work

Abstract— *This chapter provides the discussion of the background and related work of the internal impedance control to enhance the proprioceptive information perceived during the active exploration of the environment. First, this chapter discusses the biological embodied system, how the motor and sensory entities in biological system, particularly in human, are coupled and share the embodiment. This is followed by the background of how internal impedance control relates to the concept of morphological computation, and how this could help enhance the quality of both action and perception, if it is properly tuned. The exploitation of this concept in robotics field, especially in the area of actuation, is discussed. Lastly, this chapter explores the possibility of the implementation of the concept of internal impedance control for proprioception in the the active haptic exploration.*

2.1 Embodiment and motor-sensory coupling in biological systems

For biological organisms, evolution of life depends greatly on the interaction with the environment, and hence environmental adaptability, in which this extends further to the individual adaptive behaviour [26, 27]. The processing of information exchange between the world and the agent through its adaptive morphology (behavior) connected to the brain can be understood as 'embodiment'. It is generally acceptable to classify biological organisms, like human, to be an embodied intelligent agent [28]. The ideas of "embodiment" and for a system "to be embedded" have expanded beyond the study of cognitive science towards the area of artificial systems [29] and has drawn a lot of attention from various fields in the past decade, though with various interpretations [30]. The adaptive behaviour of the embodiment, which mediates both sensory and motor functions, allows the simplification of the control of dynamic interaction with the environment [5]. In general, sensing and motor functions in a biological system are combined and often co-ordinated in order to improve the quality of action and maximize the sensory information gained [15].

The integration of sensory and motor function in human's brain was first described in 1870s, when John Hughling Jackson proposed that the cortex of the human's brain is hierarchically organized and that some cortical areas are responsible for higher-order associative sensory-motor functions. These cortical areas are used to perform the associative tasks and mental processes including the sensory information interpretation, association of perceptual information with past experience, and exploration of the environment. Human's grasping task serves as a very good example to explain the co-ordination between sensing and motor functions. It was shown in previous study [31] that humans can induce learning and dexterity in object manipulation through the coordination of sensorimotor memories with haptic sensory feedback. This influences how the information flow is organised and structured within the sensorimotor network. It was further found that the organization of the information flow structure also depends on the placement and the controlled state of the body ("Morphological computation") [1].

In the recent decades, the concept of embodiment and how action and perception in intelligent agents, like humans, are reciprocally coupled is widely accepted [32, 33] to have significant contribution towards the perceptual, action, and cognitive processes in maintaining the autonomy of an agent [34, 35]. Nonetheless, the nature of sensorimotor coupling and its implications on the very nature of computation of action-perception arbitration in biological motor control is not well understood yet [14]. Biological creatures perceive information about the prevailing environmental states through embedded sensory receptors systematically scattered around the body to take the appropriate actions. However, muscle activity modulation (internal mechanism of the body) while taking actions also affect the functionality of sensory receptors coupled with the muscles, and therefore the sensory information feedback. For example, the spindle sensors (provide position and velocity feedback) and tendons (provide force/torque feedback) are physically embedded and connected among muscle fibres. This results in sensing entangled with action, offering opportunities to take control over haptic perception by changing muscle co-contraction. For instance, as people are required to estimate the weight of an object, they would not hold it with a stiff hand. Instead, they regulate the internal impedance of their hand by gently bobbing the object up and down to use proprioceptive feedback to estimate its weight.

In 1980s Vallbo et. al [2, 3] provided compelling evidence suggesting that the associative modulation of physical properties of the body in biological systems can enhance the proprioceptive feedback. This also suggests that the internal impedance state of the body, which mediates both sensing and actuation of an agent, can influence the quality of both action and perceived information [1]. The regulation of internal impedance state and behavior of the body to enhance perception can be understood in general as “active sensing”. For example, in active haptic sensing, human would modulate the internal state of the body (muscle co-contraction) in order to regulate proprioceptive feedback [36, 37, 15]. This way, humans can build associations between haptic information with the palpation behavioral variables to estimate a physical property of the environment [38–40]. Recent studies [41] show that humans use different force/velocity control strategies during manual palpation to detect abnormality inside a soft silicon phantom. These strategies are also accompanied by

other behavioral variations like the movement of fingers in different trajectories, velocities, frequencies, and regulation of applied pressure and force at the finger tip [42].

The understanding of the sensory-motor function coordinations can be skilfully utilized to maximize information gain in sensing to control biologically-inspired artificial systems, like underactuated robots. As signified in recent findings in passive compliance of biological musculoskeletal systems [5], control of dynamic interactions with the environment can be simplified through the embodiment itself. Therefore, recent findings in the emergence of adaptive behaviors of muscular-hydrostats like octopus due to its ability to control the stiffness distribution and morphology of the body [15], has caught a lot of attention among the robotics research community [43, 44].

2.2 Morphological computation in action and perception

From the perspective on the traditional robotic and artificial intelligence study, the computation, sensing, and action functions are usually facilitated by different peripherals and often viewed as separate entities. However, the implementation of such concept on a natural agents responsible for multiple complex tasks embedded in highly unstructured environment could lead to the instability and large performance error in the system. Though there have been many studies exploring the possibility of exploiting multiple controllers with machine learning algorithms to process the large flow of information; the focus of these studies were mainly on a single function, i.e. the controller [45]. However, the morphology of a system can also be viewed as tools that can contribute to and facilitate control burdens and cognitive tasks, which have traditionally been attributed to the controller alone [46, 47]. When the computational problem becomes too complex, control/computational problem is delegated from the brain to the local level of the system like at the musculoskeletal level. This concept encapsulates around the idea that during an interaction between a natural system (whether it is biological organism or artefact), and the environment; the brain (or controller), body (morphology), and the environment are coupled and influencing each other. The benefit of exploiting the adaptability of the morphology as an additional tool in cognition and control

has recently caught attentions across various disciplines, including but not limited to robotics [25, 48, 49], artificial intelligence, cognitive science [50], psychology[51], and neuroscience [52].

In general, the notion - *morphological computation* - refers to the ability of a natural agent to outsource some of the computational effort to the morphology, which can help simplifying the control task. Morphological computation appreciates the system's natural dynamics, which is usually dampen in traditional control scheme, during the interaction with the world and exploits them as tools in the computation process [53]. The ability of the agent to control or vary its physical structure (morphology) can facilitate the computational effort during the interaction with the world [54]. These include the variation in basic physical structure of the agent, change of the material properties of the agent, the geometrical properties of the agent adaptation of dynamic behavior through the physical interaction with environment, the regulation of internal mechanical properties of the body, and etc.

This thesis views the internal mechanical circuits in the embodiment as a potential computational resource for both perception and action. The internal mechanical circuits in the embodiment involves the regulation of body's stiffness and damping parameters and can often be described as mass-spring-damper problem [55, 56]. The modelling of such parameters and the evaluation of the stiffness performance in multibody robotic systems were presented and validated based on model with lumped stiffness parameters [57]. Since the mechanical impedance of the embodiment changes the functionality of those mechanical circuits, it is important to explore its role in regulating perception and action functionalities. An essential set of mathematical tools to understand the role of internal impedance in control of dynamic systems were first laid down by Hogan in [58–60]. Hogan's theory proposes that a body in dynamic contact with the environment should be able to adapt its internal impedance (stiffness, damping, and inertia parameters) in order to maintain a stable dynamic coupling with the environment.

2.2.1 Internal impedance control in action

In the artificial system, it has been well established in previous studies that allowing the compliance in the morphology of a system to shape itself to the task-specific-environment can be viewed as an extra potential computational resource [55] and can lead to a simplification of the complex learning and controlling tasks[61]. In passive dynamics based locomotion, the interaction between the physical structure and the environment was viewed as a powerful infrastructure to emerge natural-like behavior with less control effort and yet higher efficiency. Metastable passive biped walker establishes a very good example in the sense of exploiting the dynamics interaction between the properly tuned physical structure and the environment. Passive dynamic walkers presented in [62] use solely the interaction between the walker and the environment to emerge a metastable walking behavior with no sensing at all. This together with some necessary actuation, the robust biped robot yet with natural-like movement can be achieved [63]. Since the ability to exploit the morphology as additional computational resource can simplify the control task; therefore the learning task could be simplified as well. In addition to passive dynamic biped walkers, it was found in [64] that the proposed passive walker can learn to adapt to the unstructured environment while executing the walking task efficiently.

In fact, it seems that biological evolution also solves the problem of energy efficient locomotion by tuning the embodiment to be able to harness energy from the environment as shown in an experiment with a dead trout swimming against a water stream [65]. As opposed to a fully actuated robotic fish [66]; an underactuated robotic fish that utilizes the passive dynamics of the embodiment with single actuator and multiple passive variable stiffness joint, is proven to be more energy efficient while being able to emerge more natural movements [67].

The concept of internal impedance control could also be implemented in the context of manipulation or contact task during tele-operation, such as impedance control in the joint space for rigid body robotic digging in bilateral tele-operated excavation [68]. By allowing the internal impedance between the master and slave to match, the bilateral tele-operated

excavator can ensure the safe, effective, and stable operation during the contact with extreme environmental conditions [69]. Similarly, in the object manipulation task, the implication of internal impedance control could lead to an improvement in the stability during the interaction between the agent and environment. While this seems obvious in biological agents, e.g. humans usually pose little to no challenge in self-stabilization during object manipulation; rigid robots may not able to maintain their stability during intermittent contact with the environment. It was found in [70] that internal impedance control can be used in robot or artificial system to maintain the self-stability during the contact with object or environment.

The implementation of the morphological computation concept in human-robot interaction has recently attracted a lot of attention. In order for the robot to ensure safe and stable contact with human and environment, and yet be able to perform tasks that require high rigidity; it should be able to control its compliancy through the adaptation of internal impedance [71]. The ability to modulate the internal impedance of the body can also enhance the interaction quality during contact with humans in robotic massage systems [72].

In fact, the implementation of internal impedance control can be found in many disciplines. This also includes the robot-assisted medical rehabilitation devices. With an adaptive exoskeleton proposed in [73], patients with lower limb injury can improve their agility of motion and enhance dynamic response. Patients suffering from injury around the upper limbs of the body, or debilitating illness such as stroke, could use the system proposed in [74], of which the internal impedance can be varied depending on the degree of injury or required training, in order to rehabilitate their movements [75]. This concept extends further to the development of prosthetic limbs. Inspired by observing how humans regulate internal stiffness of their upper limb during force/movement control task, it was found that the robotic/prosthetic arm could also benefit from the ability to regulate the internal impedance to improve the performance in different control tasks [76], as well as to enhance stability of prosthetic devices [77].

2.2.2 Morphological computation in perception

In the context of perception, despite the advanced development of the passively functioning sensory devices, obtaining the reliable and precise sensory information in a highly unstructured environment still poses a great challenge in robotic community. The ability to adapt sensor morphology and flexible robotic morphology [78] could also be seen as a potential tool to improve the performance of sensory acquisition. Researchers have taken a number of different approaches on the active adaptation of sensor morphology to alter or enhance the physical stimuli retrieved from the dynamic environment to obtain reliable desired information [37]. An agent can therefore, through an implementation of an appropriate morphological computation strategy, maximise the sensory information gained (transfer entropy) during the exploration of the environment. The studies of adaptation of sensor morphology include the change of physical structure of the sensor itself, such as: size [79], sensor's placement, dimension [80], shape [81], orientation [82], material properties [83], and etc.

One of the very first sensory modalities that was seen as a potential perception sensation area for the implementation of morphological computation concept was vision. Inspired by observing how the sensory receptor cells, ommatidium, are scattered and organised inside the compound eyes of arthropods, i.e. insects, scientists have developed the artificial sensory system comprising of elementary motion detectors [84]. The system is allowed to adjust the orientation between the artificial detectors automatically. The system results in a non-homogeneous arrangements of the receptor cells distribution with higher number of receptors facing towards the frontal part of the system [85]. This leads to the compensation in motion parallax during the movement of the system. It is important to note here that such system can use the adaptation of the sensory morphology, i.e. orientation and the arrangement of the receptor cells, in order to compensate the motion parallax (similar to the flying insects) [86], the process of which is normally attributed to the controller at computational level.

There are many examples in nature showing how the physical stimuli in somatosensory perception during the dynamic interaction is converted and modified to the usable sensory information. The active tactile sensing apparatus that attracts a lot of attention in the field

of biology and artificial systems in the recent years, is the biological whiskers [87] found in rodents and most mammals (except human). It was found that the stiffness properties of the whisker and the interaction dynamics with the environment play significant role in the surface identification/classification. The mechanical properties of the whisker can be tuned to enhance the accuracy in the perception of the environment [82, 88]. Similar approach are used in locomotion of 4-legged robot to allow the recognition of physical properties of the environment [89] and the observation/estimation of internal state of the body [90].

As stated earlier, the perception in biological system is usually coupled and combined with actuation and motion. Therefore, the richer and more structured information can be obtained through the coordination of sensory and motor (embodiment) functions [15, 91, 92]. For example, the way humans feel the environment though sensory receptors depends on many extrinsic and intrinsic behavioral factors, such as: interaction force, tangential velocity, finger's stiffness, orientation, and etc. [39, 40, 93, 94]. This is because of that the physical stimuli during the interaction are pre-processed internally inside the morphology given different states of the body, which allows the conversion of the physical stimuli to the useful signals before passing to the receptors. This suggests that human's haptic perception does not rely solely on the tactile cues at the contact point, but also proprioceptive cues [7, 95], which involves the sensory-motor coordination, in order to obtain more complex information [96]. Therefore, apart from the changes at the physical structure level of the sensor morphology, the control of the internal embodied structure coupled between the action and perception also play important role in perception [97].

While the implication of morphological computation under the modulation of internal impedance, embodiment structure, and sensory motor coordination plays crucial role in the biological sensory systems; the implications of the embodiment concept are mostly studied in the context of enhancing the actuation, visual perception, or as an assistive element in granting or enhancing stability in locomotion, than understanding its role in perception or action-perception coupling in biological systems. They take advantage of passive body dynamics and the interaction with environment to achieve the required goals without a rather

high-level cognitive processes [36]. Therefore, this thesis investigates and attempts to explain the implication of internal impedance control in an active perception.

2.3 Biological active haptic sensing

The ability of an agent to adapt its morphology and behavior to highly unstructured environment and to simplify the computational effort under the context of perception, can be recognised as "active sensing". The concept of active perception in biological organism is not new. In biological systems, perception is commonly recognised as an "active" process rather than a "passive" one. This indicates that for a system to sense or perceive the environment, sensory-motor coordination is the key feature [98]; that is one must act upon the environment to sense it. In 1966, Gibson [91] described the perceptual information as "imposed" and "obtained" information, where the latter refers to the information perceived through the activities with the intention of information seeking. He further explained this concept of information seeking in perceptual system using visual perception. Biological organism's visual perception of the environment begins with having a specific tasks, which guides one's action and the discovery of environmental properties. Therefore, "Perceiving gets wider and finer and longer and richer and fuller as the observer explores the environment." [99].

The activity of information seeking in the context of perceptual activity is not limited only to vision, but also extends to other sensation modalities, such as active haptic perception. This thesis is particularly interested in the human active touch sensation. Human active touch has been described by Bell in 1865 in his book [100] as the intergration of cutaneous sensations at both the contact point with the external stimuli and the internal muscular activity (proprioceptive information) resulting from the manipulation of the sensing organs [96, 101].

It was found in Gibson's "Observation of active touch" that with active touch (active motion of hand), humans can identify six different objects with 95% accuracy; while this resulted in 49% with passive touch [102]. Though, it is generally believed that the motion of sensory receptors during active touch could enhance the perception, it is in fact the control of

sensory system in a purposive and information-seeking manner, that enhance the stimulation [37, 103]. Therefore, haptic perception can be viewed as comprising of a coupled system, where the sensory unit is carried by the motor control unit. Apart form the information processing of physical stimulation, the way the motor control is executed with the intention to obtain and extract those stimulations also is essential in the active haptic perceptual process [104, 105]. Hence, it is commonly recognised in biological haptic perception that both tactile cues and proprioceptive cues play significant and integrative roles in haptic perception. This was evidenced in many studies relating to the influence of proprioceptive stimuli on the touch sensation, such as: in the estimation of object's geometrical property [106, 107]. The active sensing under proprioception involves the actuation of muscles and the activation of embedded somatosensory receptors (for proprioception) [108].

Proprioceptive mechanoreceptors such as spindle sensors (sense the amount and speed of muscle contraction) and tendon sensors (sense force) are located in the very muscles that are used to actuate joints [109]. Therefore, controllers in the central nervous system perceive the environment depending on the actuation state of the muscles and muscle actuation in turn depends on perception [6]. It was found that during human's active touch, humans would modulate the internal state of the body (muscle co-contraction) in order to regulate proprioceptive feedback [36, 37, 15]. This way, humans can build associations between haptic information with the behavioral variables to estimate the physical property of the environment [38–40]. The recent study [41] shows that humans use different force/velocity control strategies during manual palpation to detect abnormality inside a soft silicon phantom. The regulation of these strategies are accompanied by behavioral variations like movement of fingers in different trajectories, velocities, frequencies, regulation of finger's joint stiffness, and regulation of applied pressure and force at the finger tip [42].

Active haptic exploration is one of the most evident and frequent sensing activity performed by humans in each and every day apart from vision. In addition to vision, haptic perception allows the agent to perceive more complex mechanical and physical properties of the world or manipulated object, which can be extracted only upon physical interaction. This includes roughness, stiffness, mass, texture, friction, elasticity and etc. One of the most interesting

tasks in active haptic exploration is the examination of non-rigid object or environment. Physical examination of soft objects to identify hidden mechanical features can be seen in a variety of areas like minimally invasive surgery, medical physical examination, security, quality assurance in food industry, entertainment, etc. Manual examination involves variation of both behavioral and internal impedance levels of the fingers [41, 110], because the interplay between motor control and internal mechanics (muscles and reflexes) [15, 16] play an important role in both action and perception [17].

This poses an interesting question as to how the internal impedance of the finger are modulated during such exploration. It is also intriguing to understand how the interplay between motor control and internal impedance influences the proprioceptive information. These are not fully understood under the study of biology and cognitive science. The question as to how the interplay among muscle actuation behavior, environment, and co-contraction of antagonistic muscles affect the accuracy of proprioception is not well quantified yet [1]. Although it is known that proprioceptive cues play important roles in extracting complex physical properties from the environment, its influence and how its information is combined with other cutaneous sensation are not yet well understood [19, 111].

2.4 Active haptic sensing in robotics application

"Active sensing" or "active perception" in robotics refers to the modulation and adaptation of the sensor's state and the behavior of the system, in which the sensor is embedded, according to the environmentally suitable strategies [112]. Robotic active perception has attracted recent attention especially in the context of vision [113]. Though active exploration for visual cues in the external world has been widely studied for instance in recognition and exploration of robot's activities while interacting with environment [114, 115], active exploration in the internal impedance domain for enhanced haptic perception, especially in proprioceptive cue has not been studied so far.

Haptic perception in artificial autonomous agent, like robot, can provide useful information about the environment during the interaction. Haptic perception is often seen as an additional

perception channel to augment visual sensation [116–118] and to improve robotic dexterous task [119]. The information provided by haptic perception can be used to recognise the physical, geometrical, and interaction dynamic properties of the object and the world [120]. This information provides the fundamental knowledge for object recognition [121], surface [122], and texture [123] classification. As mentioned in previous section that human's active haptic exploration involves motion control of the body and the co-ordination of sensory-motor control [39]. Therefore, human's motion control in haptic exploration is executed to obtain the information according to the desired information about the environment's properties [104, 124]. The exploratory process, EP, in robotic haptic system, inspired by the biological active haptic exploration, has been long-standing and fundamental implementation concept. Scientists have developed haptic sensing apparatuses with the integration of different active algorithms and motion control strategies to acquire different information [125]. It was shown that through the implication of different strategies, the machine can obtain higher dimensional haptic information about the properties of the interacted environment [114, 117, 121–123, 126].

Another equally important factor in determining the quality of haptic information obtained from the environment, in biological active haptic exploratory process, is the control of internal parameter of the receptor-embedded morphology. For example, it was shown under the context of artificial tactile modality that the compliance of the sensory system and the deformation of the sensor pad could be used to extract some useful low-level tactile information, such as: the edge and orientation of object [127]. Given the highly complex nature of the biological active haptic sensing process, it is interesting to study the role of the internal parameters (internal impedance) during such exploratory process, in both biological and artificial science perspective. Particular attention in this thesis is given to the proprioceptive cues, at which there exists the relationship between sensory and motor functions (embodiment). Therefore, during such motor command accompanied by the information-seeking intention, the associated musculature, at which numbers of mechanoreceptors are embedded, are regulated to condition the proprioceptive feedback. Though, many studies explored the role of exploratory processes in the robotic active haptic perception, these studies only discussed the movement behaviors

rendered from the apparent behaviors observed in biological organisms. It is, however, important to take into account the internal impedance control strategy used to actuate the movement as well.

2.5 Haptic perception in minimally invasive surgery

One of the most interesting and challenging applications concerning the haptic perception in robotics can be found in the exploration and determining physical properties of soft object. Physical examination of soft objects to identify hidden mechanical features can be seen in a variety of areas like minimally invasive surgery, medical physical examination, security, quality assurance in food industry, entertainment, etc. Manual examination involves variation of both behavioral and internal impedance levels of the fingers [41, 110], because the interplay between motor control and internal mechanics (muscles and reflexes) [15, 16] play an important role in both action and perception [17]. In this thesis, the focus is mainly concentrating on the implementation of active haptic exploration under the proprioceptive cues for the detection of mechanical stiff inclusion inside a sample soft tissue, similar to medical manual palpation. One of the objectives of this thesis, apart from understanding the relationship between the internal impedance and the proprioceptive cues during active haptic exploration, is the exploration into the possibility of the implementation of such concept in the soft robotic probe that could be used in robot-assisted minimally invasive surgery to enable the surgeons the sense of touch.

In the recent years there is an increased attention towards the development of soft robots that enable new capabilities for robotic systems. The main features can be considered as an increased safety, better dexterity and high flexibility. Various works and projects present the concept and latest developments on surgical flexible robots [128]. Many of the flexible robotic systems aim for the final use in robot-assisted minimally invasive surgery (RMIS). This procedure has various benefits for the patient, such as smaller blood loss, reduced amount of medication and shorter recovery stage. Surgical manipulations are performed via trocar ports with the help of miniature instruments. High resolution three-dimensional visual

information is the main real-time source of the information about the surgical site. However, it has been shown that the presence of tactile feedback during RMIS can also improve the clinical outcomes [129]. Specifically, haptic sensing can be used to detect collisions between instruments and soft tissue, measure the pressure applied during gripping or dissection, as well as help to find hard abnormalities in soft tissue, such as tumors.

On the contrary, in the traditional open surgery, surgeons can directly investigate mechanical properties of soft tissue by directly palpating on the target area [130]. Palpation, or manual examination techniques, is used to assess the physical properties of soft tissue. Clinically defined palpation movements and strategies are specifically designed for the target area of examination [110, 131]. In addition the common practice is to combine various examination strategies during one single examination. For instance, global scanning of an organ is combined with local examination techniques, such as vibration or sliding. The effectiveness of palpation to detect abnormalities in soft tissues is limited both by palpation experience and by limits of human tactile perceptive system. Previous studies [132, 41] have indicated the importance of the applied examination strategy during probing of soft non-homogeneous environment. Specifically, it was defined that the modulation of force and velocity in the vicinity of non-homogeneity (hard nodule) significantly influences the detection and localization of the nodule.

The area of haptic sensing for RMIS has been extensively studied in the recent years. Various devices have been developed for probing or palpation of soft tissue [133]. Some of them have been tested in-vivo. However, tactile palpation of soft tissues is not yet implemented for real-life surgery. Variability of measurement data caused by environmental disturbances, as well as certification and lack of testing are the main reasons for that.

Similar to the problem with rigid surgical robots, soft robotic devices developed for RMIS have a potential need to be equipped with tactile sensing probes. However, a great majority of the available tactile devices, including palpation probes, have rigid structures. The current technique of using rigid tactile probes for soft robotics manipulator mainly relies on the probing behaviors and the sensitivity of the sensor to perform an accurate identification and

hence reduces the importance and benefits of soft robotics, as the tool is in the direct contact with the tissue.

Chapter 3

Human's internal impedance control during haptic perception

Abstract— *When humans are asked to palpate a soft tissue to locate a hard nodule, they regulate the stiffness, speed, and force of the finger during examination. If the relationship between these behavioral variables and haptic information gain during manual probing can be well understood, the efficacy of proprioceptive sensation for soft tissue palpation, such as in tumor localization in minimally invasive surgery, can be improved. This chapter explores how human's use the proprioceptive sensation through the regulation of finger's stiffness during manual palpation to interpret the perceived information based on the prior experience. During the experiment, the muscle co-contraction activity of the finger was recorded using EMG sensors to investigate whether joint stiffness control during manual palpation plays an important role in the haptic information gain. A Markov chain was trained using muscle co-contraction patterns of human subjects to extract generic strategy employed by human. The experimental results revealed that during the exploration of the environment, the control of the finger's stiffness in general occurs in small step. The Eigenvalues and Eigenvectors corresponding to the state transition matrices also suggest that the duration of the exploration depends on the physical properties of the environment.*

3.1 Introduction

Although it is evidenced in many studies that the integration of the information perceived through both tactile and proprioceptive sensation can enhance the haptic perception, the questions as to why human regulates the internal impedance to condition the proprioceptive sensors and how the pattern of this regulation is organised remain unanswered [19]. It is important to note here that the objective of this chapter alone is not to fully address these questions; however the theme of this chapter is stemmed from these two important questions.

The theme of this chapter is to investigate the role of proprioceptive sensation during human's manual palpation on the interpretation of perceived information based on prior experience. The experiments presented in this chapter begin with the observation of muscle co-contraction strategies during human's manual palpation to estimate the depth of a hard nodule embedded in a soft silicone phantom. The experiment involved in total of 6 healthy participants and 3 soft silicone phantoms with a nodule embedded at 3 different depths. Each participant was given 5 learning iterations per soft silicone phantom to explore the differences between the depth levels. After a learning phase, participants were blindfolded and asked to palpate the silicone phantom to estimate the depth of the embedded nodule. The electromyography (EMG) signals show that participants regulated their muscle co-contraction states during probing. Human's antagonistic muscle co-contraction strategy was abstracted in the form of a Markov decision process from the electromyography (EMG) signals recorded from the human subjects.

This raises the question as to whether the humans employ different muscle co-contraction strategies to gain transfer entropy of haptic perception by recruiting finger's stiffness dependent past haptic memory primitives during manual palpation. This stems from the premise that finger stiffness modulates the functionality of tendon and mechanoreceptors.

3.2 Experimental setup and methodology

3.2.1 Design of the experiment

In this chapter, manual palpation task was used to derive deeper insights into possible reasons as to why humans control finger stiffness during soft tissue palpation by testing their strategy in a controllable stiffness soft robotic probe to do the same task. Here 3 soft silicone phantoms were as the samples in the experiments, where each contains a plastic bead embedded at 2, 4, and 8 mm beneath the exposed surface of the phantom (see Figure 3.1). The silicone phantom is made from a soft clear silicone elastomer gel RTV27905 from Techsil.

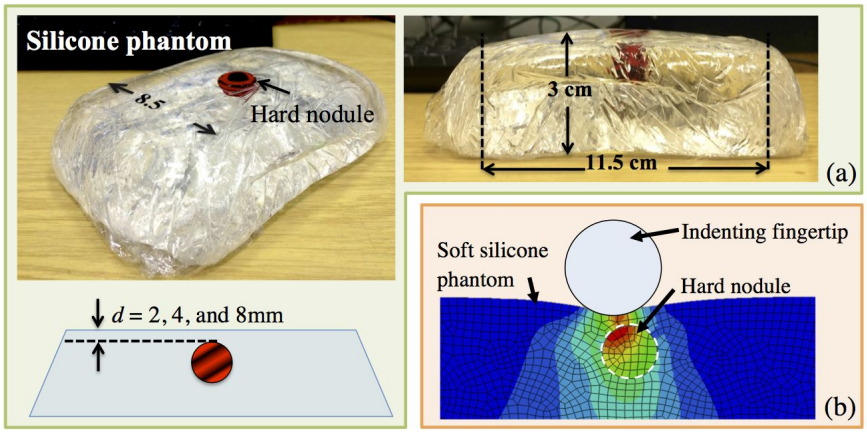

Fig. 3.1 (a) A soft silicone phantom fabricated using soft clear silicone elastomer gel with a spherical plastic bead of size 15 mm diameter embedded inside at the depth of d =2, 4, and 8 mm. (b) Example of the finite element simulation of soft silicone phantom with an embedded hard nodule being palpated using a an indenting fingertip [132].

The ABS plastic bead, which hereafter in this thesis refers as “hard nodule”, was embedded between two layers of silicone phantom - top and bottom layer. The hard nodule is stiffer than the soft silicone phantom used in this study. Therefore the contrast between the stiffness of the soft silicone phantom and the hard nodule represents a good approximation of the difference in the stiffness between the malignant tumor and healthy fibroglandular breast tissue [134]. In addition, according to the studies in human biology, the typical tumor in soft tissue has roughly spherical shape [135] and at T1 stage can vary in size between 0.5

to 20 mm [136]. Hence a spherical plastic bead with a diameter of 15 mm was chosen and embedded inside each phantom at different depths.

In the fabrication process of each phantom, the given chemical substances (Part A and B) were mixed in 1:1 ratio according to fabricants specification. First, the top layer was created by pouring the mixture into the mold until the depth reaches the desired nodule's depth, i.e. 2, 4, and 8 mm. This layer is allowed to rest until completely cured. The nodule is then placed in the middle of the mold on this layer. Then the bottom layer was created by pouring the rest of the mixture into the same mold until the total height of the phantom reaches the height of 3 cm. The whole phantom is allowed to cure until completely solid.

The dynamic of the interaction behavior between the soft silicone phantom and hard nodule during palpation was simulated using finite element analysis in [132]. The simulation result is shown in Figure 3.1 (b). This illustrates the distribution of stress and strain in FEM analysis during the contact between simulated phantom with hard nodule and the simulated finger tip. It is shown that the interaction is dynamic and not only the nodule is being felt; but also the combination of interaction behavior between the nodule and the tissue. This results in the dynamic response in the human's finger.

3.2.2 Methodology

The main focus of this experiment was to understand how the muscle co-contraction level of the human forearm corresponding to the finger stiffness affects the estimation accuracy of depth of a hard nodule buried inside a soft silicone phantom. Here, the focus was on the abduction and adduction activity of the finger, for which the metacarpophalangeal (MCP) joint is mainly responsible. It was shown in previous studies [138, 139] that the MCP joint of the index finger can be modulated by the co-contraction of the flexor and extensor muscle in the arm. Therefore this activity can be quantified through measurement of the muscle surface electromyography (EMG) of the major finger antagonistic muscle pair, namely: flexor digitorum superficialis (FDS) and extensor digitorum communis (EDC) muscles [140]. The location of this muscle pair is shown in the anatomical structure in Figure 3.2 (a). The activity of the individual muscle is directly related to the muscle force. Since these two

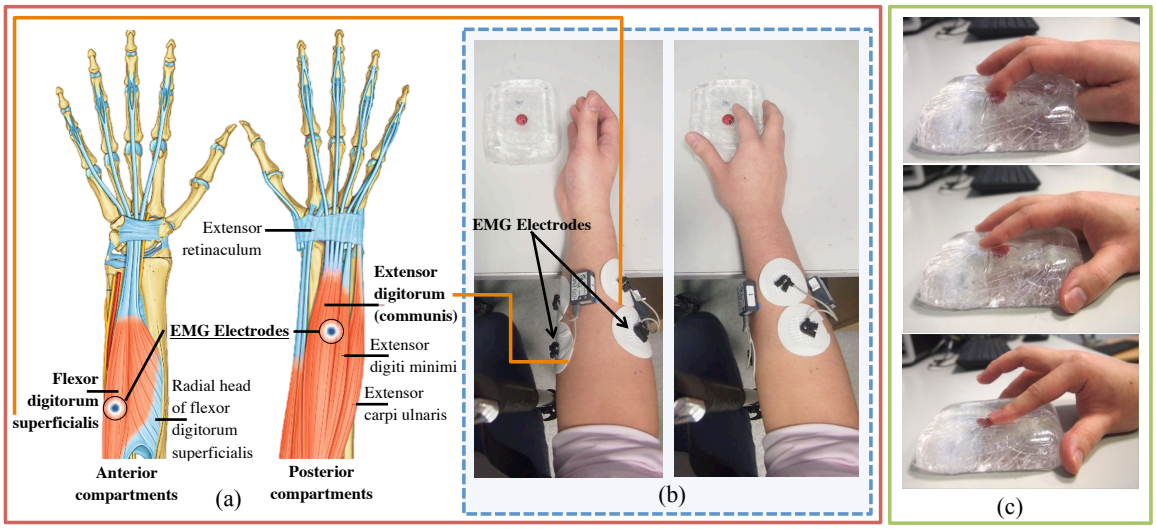

Fig. 3.2 (a) Anatomical structure of posterior and anterior compartments of superficialis muscle layer of forearm with the indication of the EMG electrodes placement locations at the surface level of EDC and FDS. This figure is modified from Chapter 7 of [137]. (b) Photos of the human's forearm with the EMG electrodes attached to EDC and FDS muscles in the experiment. (c) Photos of human's finger using various finger stiffness levels and postures during palpation.

muscles are coupled with the MCP joint, the force from each muscle antagonistically affects the joint torque. Therefore, the internal impedance (stiffness) of the finger's joint increases with simultaneous increase of both FDS and EDC muscles' activity.

The experiment involved 6 healthy subjects with no hand/wrist injury, in the age group of 20 - 43 years. This experimental protocol was approved by Kings College London Biomedical Sciences, Medicine, Dentistry, and Natural and Mathematical Sciences research ethics committee. The corresponding information sheet and consent form provided for human subjects can be found in Appendix A.1. During the experiment, subject was asked to sit in a relaxed posture with the dominant forearm resting on a lab desk. The subject's dominant hand was placed directly on top of the soft silicone phantom to palpate a soft tissue. A pair of wireless Desktop Direct Transmission System (DTS) for wireless EMG electrodes from NORAXON U.S.A, Inc. (16 bits resolution) were attached to the subject's arm to capture the EMG signals at 1500 Hz at FDS and EDC area as shown in Figure 3.2 (b). In order to properly locate the location of both FDS and EDC muscles, participants were asked to

contract the forearm so that the location of both muscles become more apparent and easier to identify. To avoid noise and crosstalk from the EMG sensor, the skin was cleaned with alcohol before the electrodes were attached.

During the experiment, the EMG signal can be affected by many factors, both extrinsic and intrinsic. These include the placement of the electrodes, skin's temperature and humidity [141], subject's individual muscle fiber composition [142], and anatomical structure of each individual. This can lead to the high variability of the EMG signal among subjects. Therefore the magnitude of muscle coactivation can differ between subjects due to aforementioned reasons. Hence, prior to conducting the experiment, each subject was asked to perform a reference test. A reference test was conducted by asking each subject to hold and freely manipulate a mass weighing 5 kg. The EMG signal from both FDS and EDC muscles were recorded during maximum voluntary contraction (MVC).

Training phase

The experiments were divided into two phases for all subjects, namely: the training phase and the nodule's depth estimation phase. Firstly, in the training phase, subjects were asked to palpate the soft silicone phantoms with hard nodule embedded at different depths (shown in Figure 3.2 (c)). Subjects were informed about the nodule's depth in each palpation trial. The training phase was carried out for five trials per nodule's depth level, where in each trial, human subjects were given the time of maximum one minute. Subjects were allowed to rest between each trial. The order of the phantom samples presentation in the training phase is shown in Table 3.1.

Table 3.1 The order of presentation of phantom samples in the training phase of manual palpation experiment

Trial	1	2	3	4	5	6	7	8	9	10	11	12	13	14	15
Depth [mm]	2	4	8	2	4	8	2	4	8	2	4	8	2	4	8

Assessment phase

In the nodule's depth estimation stage, subjects were asked to estimate the depth of a hard nodule during manual palpation. Subjects were blindfolded to mitigate the aid of visual perception in the estimation of nodule's depth. The identical set of phantoms used in training phase were presented to the subject one at a time in a random order (with 5 repetitions per each phantom sample) to avoid any bias learned during the first training phase. The order of the phantom samples presentation in the estimation phase is shown in Table 3.2. The maximum amount of time given to each human subject in each estimation trial was one minute to estimate the depth of the nodule. At the end of each trial, subjects were asked to estimate the depth of the buried nodule. The question was "Please estimate the depth of a hard nodule based on your haptic perception". The estimated depth was verbally given to the experiment instructor at the end of each trial. The EMG signals during the estimation were recorded to explore the strategy used by human to estimate the nodule's depth.

Table 3.2 The order of presentation of phantom samples in the estimation phase of manual palpation experiment

Trial	1	2	3	4	5	6	7	8	9	10	11	12	13	14	15
Depth [mm]	2	8	2	4	4	8	4	2	8	4	8	4	2	8	2

3.3 Results

3.3.1 Manual palpation results

The raw EMG signals from both EDC and FDS muscles captured during MVC and palpation activity of each subject were pre-processed by applying rectification and smoothing method with the use of Root-Mean-Square (RMS) processing, in order to remove the noise interference and signal artifacts that may be present in the raw EMG signal. During MVC activity, the maximum value of the processed EMG signals, s_i^{max}, from both FDS and EDC muscles, where $i = FD$ and ED respectively, were recorded for each subject. s_i^{max} were used as referencing value in the normalization of the EMG signal obtained during palpation trials.

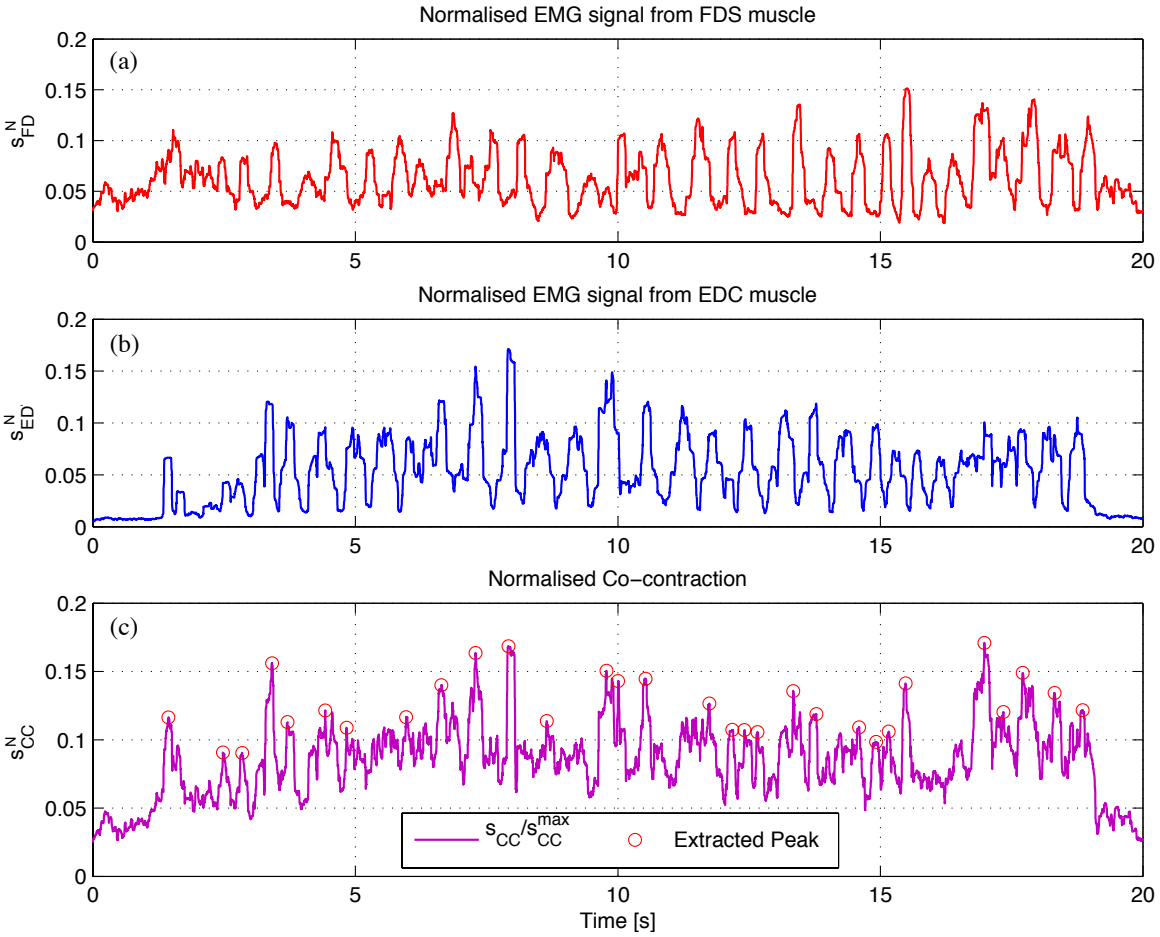

Fig. 3.3 Sample of muscle activity quantified by the EMG signal during a human manual palpation trial to estimate the depth of a hard nodule. The EMG signals measured, s_i ($i = FD$ and ED), from FDS and EDC muscle of the subject's dominant forearm were normalised against the respective EMG signals during MVC (a) and (b) show the normalised EMG signal, $s_i^N = \frac{s_i}{s_i^{max}}$ from both FDS and EDC muscle pair respectively. The combination of the activities contributed from both muscles can be described as the co-contraction behavior of the muscle. The normalised co-contraction EMG signal, $s_{CC}^N = \frac{s_{CC}}{s_{CC}^{max}}$ is shown in magenta curve in (c); whereas the red circles indicate the extracted peaks.

The pre- processed signals from both EDC and FDS muscle obtained during palpation are represented by s_i.

The pre-processed signals were normalized against the referencing values obtained during MVC activity, s_i^{max}.

$$s_i^N = \frac{s_i}{s_i^{max}}, \tag{3.1}$$

where s_i^N represents the normalised EMG signal of each muscle. The example of the normalized EMG signals from FDS and EDC from one of the subjects during a palpation trial are shown in Figure 3.3 (a) and (b). As mentioned previously in Section 3.2.2, the stiffness of the MCP finger joint increases with the simultaneous increase in muscle activity of antagonistically coupled FDS-EDC muscle pair (co-contraction). The total EMG can be computed by the summation of the rectified EMG signal from the FDS-EDC muscle pair [143]. This results in the co-contraction activity, which is similar to the way used to compute the stiffness synergy in the control of robot hand using EMG signal from FDS-EDC [144]. The EMG of co-contraction activity can therefore be represented by:

$$s_{CC} = \sum_i s_i, \tag{3.2}$$

Hence, the normalised EMG of co-contraction activity can be computed as following:

$$s_{CC}^N = \frac{\sum_i s_i}{\sum_i s_i^{max}}. \tag{3.3}$$

The sample of normalised co-contraction signal is shown in Figure 3.3 (c). The peak activation of the co-contraction during palpation can be directly extracted from the normalized co-contraction to observe the strategy employed for each trial given different sets of the environment. As highlighted in the sample signals shown in Figure 3.3 (c), human modulates co-contraction activity of the muscles during estimation of the nodule's depth.

The average estimation accuracy for each depth level at each trial across all subjects are shown in Figure 3.4 (a). The average estimation accuracy of nodule's depth at d =2 mm increases from 65% to above 80% after first estimation trial; whereas the accuracy in estimation at other depth levels reaches maximum after second estimation trial. The average of estimation accuracy when nodule is buried at depth, d = 4 and 8 mm, reaches 65% at the 3rd estimation trial. The standard error for the nodule's depth estimation tends to decrease slightly across trials.

The overall accuracy from the estimation of the nodule's depth embedded inside a soft silicone phantom across all 6 subjects and all trials for each depth level is shown in Figure

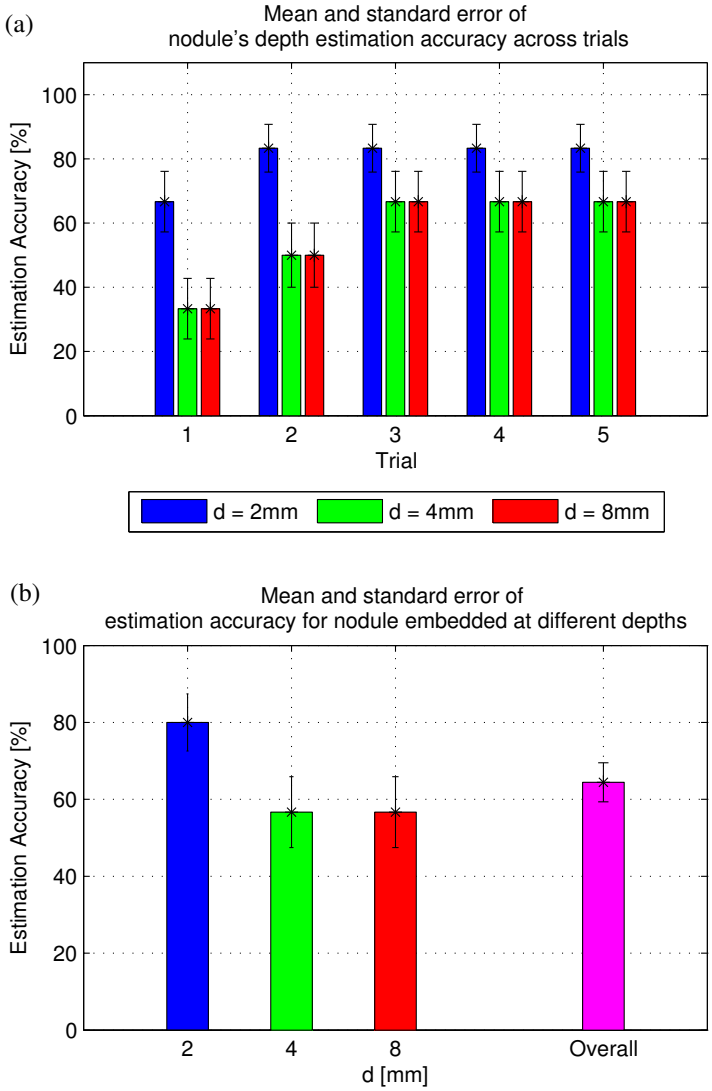

Fig. 3.4 (a) The mean percentage and standard percentage error of nodule's depth estimation accuracy across trials for the nodule embedded at $d = 2$, 4, and 8 mm are explicitly shown in blue, green, and red bar. (b) The overall mean and standard error of nodule's depth estimation accuracy for across all trials and subjects.

3.4 (b). It is shown that on average human can correctly estimate the depth of the nodule embedded at 2 mm in 4 out of 5 trials (shown in blue bar); while the nodule buried at 4 mm and deeper (shown in green and red bar respectively), the accuracy in nodule's depth estimation drops to 56.7%. These result in the overall average estimation accuracy of around 65% (shown in magenta bar). Two-way ANOVA with post hoc Bonferroni correction was performed to examine the effect of variation of nodule's depth and number of trial on the

nodule's depth estimation accuracy. The two-way ANOVA showed no significant influence of the nodule's depth level ($p > 0.05$), the number of trials ($p > 0.05$), and the interaction between the nodule's depth level and number of trials ($p > 0.05$) on the accuracy of estimation. Since, both nodule's depth level and the number of trials do not statistically influence the nodule's depth estimation accuracy, it is interesting to further explore as to which factor may influence the estimation accuracy.

This leads to a question as to whether humans use different muscle co-contraction strategies as shown in Figure 3.3 to obtain the accurate estimation of the environment (measured in transfer entropy of haptic perception) by recruiting finger's internal stiffness dependent past haptic memories during soft tissue palpation. Therefore, it is interesting to explore the pattern of finger's stiffness control strategy employed by humans during such task, and repeat the strategy on a controllable stiffness robotic probe to check if it can improve the estimation accuracy of haptic perception by following the same approach.

3.3.2 Extraction of muscle co-contraction pattern

This section focuses on the extraction and derivation of the generic pattern of finger's stiffness control strategy derived from the subjects to the experiments given soft phantoms with nodule embedded at different depths. The strategy employed by human can be represented in a Markov chain which quantifies probability of moving from one level of muscle co-contraction to another (hereafter referred as "state"). The probability of the change in co-contraction level between the current state to the next state across all subjects during the nodule's depth estimation for d =2, 4, and 8 mm were normalized and presented in Figure 3.5 (a), (b), and (c) respectively.

Therefore, if it is assumed that the initial co-contraction state S of the muscle pair is randomly sampled in each trial t from distribution $P_{S,t}$ the probability distribution of next co-contraction state can be computed from the Markov Decision Matrix (state transition probability matrix), M_{mk} as given by:

$$P_{S,t+1} = M_{mk} P_{S,t} \tag{3.4}$$

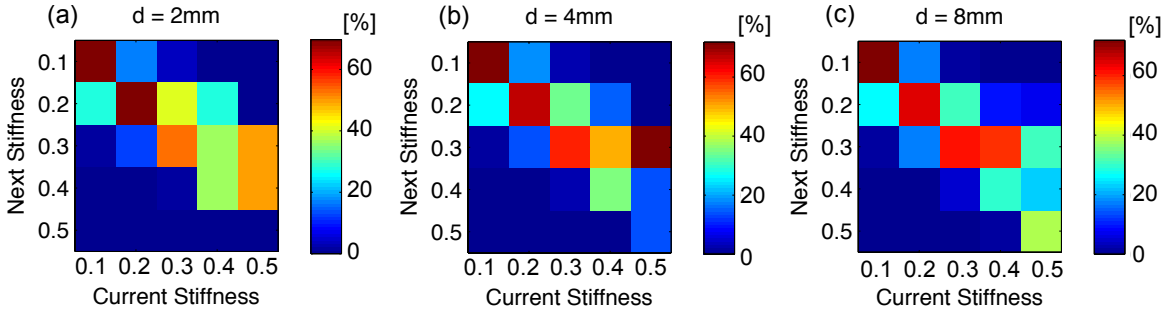

Fig. 3.5 From the extracted peaks of the normalised co-contraction signal, s^N_{CC}, across all subjects and all nodule's depth estimation assessment trials, the strategy employed by human to change co-contraction level from current stiffness to next stiffness when exploring the soft phantom with a nodule embedded at d =2 mm (a), d =4 mm (b), and d =8 mm (c), can be summarized in Markov decision matrices.

It was found in [145] that the probability distribution of the surface EMG signal tends to be either super-Gaussian or Gaussian, depending on the contraction levels. Therefore for the simplicity, in this case, the probability distribution of the state S was assumed to be Gaussian of the form:

$$P_{S,t} = \frac{1}{\sigma_S\sqrt{2\pi}} e^{\frac{(S_t-\bar{S}_t)^2}{2\sigma_S^2}}, \tag{3.5}$$

with the expected value $\bar{S}_{t=1}$ and a standard deviation σ_S. Since $P_{S,t+1}$ does not have the same standard deviation of $P_{S,t}$, only the expected value of $P_{S,t+1}$ was kept and the standard deviation was set back to σ_S in trial $t+1$ in equation (3.4) to prevent the distribution from converging to a uniform distribution across trials.

The state transition probability shows that on average the regulation of co-contraction transition level tend to be on a diagonal line between the current and next transition. This suggested that the change in the level of co-contraction with respect to the current state occurs in small steps within the local muscle co-contraction region and large sudden changes are less likely to occur. Apart from the overall trends of the muscle co-contraction strategy human employed, it is important to also investigate the characteristics of the strategy used during manual palpation given different nodule's depth levels by investigating each state transition probability matrix.

From the extracted Markov decision matrices, they can be viewed as the random walker as shown in Figure 3.6 (a). The characteristic behavior of each matrix can be explored through the corresponding eigeninformation. In a state transition probability matrix, the unit eigenvalue corresponds to the absorbing eigenvector. The rest of the eigenvalues correspond to the speed at which states converge to this absorbing vector. Since smaller eigenvalues make corresponding vector components to converge faster to the origin, the second largest eigenvalue dominates the overall behavior of the state transition probability matrix.

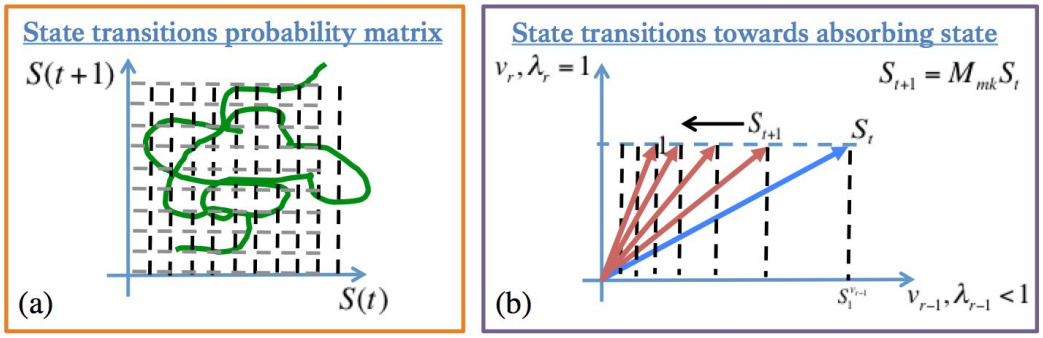

Fig. 3.6 (a) State transition probability matrix viewed random walker and (b) the convergence of the state vector towards the absorbing state.

For example, (as shown in Figure 3.6 (b)) if current (at time t) state vector S_t is assumed to project onto the eigenvector v_r corresponding to largest eigenvalue ($\lambda_r = 1$) and the eigenvector v_{r-1} corresponding to second largest eigenvalue $\lambda_{r-1} = 1$. By observing the second largest eigenvalue, it could be used to quantify how long it will take for the state vector to converge to the absorbing state. This means that the projection of the state vector S_n on the eigenvector corresponding to second largest eigenvalue ($S_n^{v_{r-1}}$) is close to 0. So if the current state S_t is continuously multiplied by the Markov matrix, the geometric series of the projection of the state vector onto the eigenvector v_{r-1} can be obtained as following:

$$\lambda_{r-1} S_1^{v_{r-1}} \quad \lambda_{r-1}^2 S_1^{v_{r-1}} \quad \ldots \quad \lambda_{r-1}^n S_1^{v_{r-1}}, \tag{3.6}$$

where the corresponding projection on the second vector at n^{th} step is

$$S_n^{v_{r-1}} = \lambda_{r-1}^n S_1^{v_{r-1}}. \tag{3.7}$$

Table 3.3 Eigenvalues of Markov State Transition Probability Matrix of extracted finger's stiffness control strategy employed by human during the interaction with soft phantom with nodule embedded at different depth levels

Nodule's depth, d [mm]	**Eigenvalues**	n ($\epsilon = 0.05$)
2	[-0.0006, 0.2945, 0.3936, 0.5984, 1.0000]	5.8340
4	[0.1393, 0.2772, 0.4069, 0.6628, 1.0000]	7.2839
8	[0.1958, 0.3468, 0.4270, 0.6992, 1.0000]	8.3722

It is assumed that ϵ is a very small number.

$$\lambda_{r-1}^{n} = \epsilon. \tag{3.8}$$

Therefore, the expected step, n, to the absorbing state can be obtained by:

$$n = \frac{\log|\epsilon|}{\log|\lambda_{r-1}|}. \tag{3.9}$$

The eigenvalues in Table 3.3 show a growth of the eigenvalues when the depth of the nodule increases. This indicates that regulation of stiffness (level of muscle co-contraction) undergoes a longer period of exploration before converging to an absorbing state when the depth increases.

3.4 Discussion

This chapter has explored the role of internal impedance (stiffness) control of human's finger in proprioception during the examination of soft object for estimating the its physical property - in this case, the depth of a hard nodule in a soft silicone phantom. The problem statement defined in this chapter is to investigate whether human modulates the internal stiffness of the finger in order to interpret the information perceived from sensory receptors and to enhance the accuracy in estimation of the physical properties of the environment, i.e. nodule's depth, during manual palpation.

The experiment presented in this chapter involved in total of 6 subjects in the manual palpation task. Each subject was asked to palpate three different soft silicone phantoms

with nodule embedded at three different depth levels. Each subject was informed about the depth of the nodule in the training phase. After the training phase, the EMG signals from the FDS and EDC muscle pair were recorded in the estimation phase, where the identical set of soft silicone phantom were presented to the subject in random order. In each trial in the estimation phase, the subject was asked to verbally estimate the depth of hard nodule. The estimation results given each depth level do not render statistically significant different estimation accuracy. Therefore, there may be some other factors during physical interaction between human's finger and the soft silicone phantom that influence the proprioceptive information. It is important to also note that this experiment involves low number of participants. It is therefore not possible to draw a statistically concrete and generalised conclusion about the muscle co-contraction strategy that humans employed to perform the manual palpation task. However, the fact that they regulate their finger's stiffness during the exploratory process is still valid.

It is noteworthy that in human, haptic perception is the result of the integration of both tactile and proprioceptive stimuli [146, 106]. The processing of both stimuli are always combined during haptic sensation, regardless of whether those information are relevant in a particular task [13]. It has been found in a previous study on the human's haptic perception [147] that the small number of different sensory stimuli (single channel of tactile and single channel of proprioception) is preferred over a large number of the same type of sensory stimuli (multiple channels of tactile) alone.

Since internal impedance determines how proprioception and action are coupled in a shared embodiment (tendon located in the very muscle used for actuation) , the internal stiffness control of the finger may offer the unique opportunity for sensory information processing system to infer the real-time proprioceptive information with the past experience to enhance the accuracy of estimation. Hence, it is interesting to observe the pattern of finger's stiffness control strategy employed by human during manual palpation. The muscle co-contraction strategies employed by each subject was extracted from the recorded EMG signals. The average strategy given different nodule's depth levels across subjects were presented in form of Markov decision matrices. The eigenvalues of the Markov matrices suggest that the regulation

of stiffness undergoes a longer period of exploration before converging to an absorbing state when the nodule's depth increases.

Up to this point, this thesis has not explained the reason behind the regulation of internal impedance in human during exploration of the environment; however, this chapter nonetheless provides some useful guideline and poses a very interesting theme of this thesis. As the thesis progress, the coming chapters investigate around the possible explanation as to how important is the active haptic exploration through the regulation of internal embodied system in the interaction with the environment. Since, it is difficult to understand the relationship between the internal impedance states and the proprioceptive signals and how the regulation of internal muscular activity, which modulates the proprioceptive cues, could enhance the haptic perception under the study of conventional biology [148]; this thesis proposes the robotic approach to understand this.

Chapter 4

Design & simulation of biologically-inspired controllable stiffness robotic manipulators

Abstract— *This chapter presents the design of the biologically-inspired controllable stiffness robotic manipulators used in the experiments presented in this thesis. This chapter proposes two different designs; one with manually adjustable joint stiffness and one with automated joint stiffness control mechanism. The mutual characteristic of both designs is that the sensing apparatus (force sensor) is coupled with variable stiffness joint. This is similar to the proprioceptive sensing system found in human's finger or arm, where tendon and spindle are embedded in the same musculoskeletal structure used to actuate (change the stiffness). The sensing information captured at the force sensor during its physical interaction with the external environment is therefore conditioned by the level of joint's stiffness rating. The simulation results predicted that the torque/force felt at the base of the manipulator can be controlled using variable stiffness joint. The relationship between the torque felt and the combinations of probe's stiffness, indentation level, and PSV are non-linear. This offers unique opportunity to implement the algorithms in stochastic machine learning and information gain metrics to allow the enhancement of the proprioception and haptic perception.*

4.1 Introduction

The design of the compliantly actuated joint can be categorized in four different groups [149] according to the working principle, namely: equilibrium-controlled stiffness, antagonistic-controlled stiffness, structure-controlled stiffness, and mechanically controlled stiffness. The concept of Equilibrium-controlled stiffness was employed by several systems, such as: "Series Elastic Actuator" or "SEA" [150], and "Spring Over Muscle" [151], which exploit a rather trivial dynamic equilibrium position control of the elastic element(s), i.e. spring, to regulate the required force to achieve the desired stiffness. However, the limitation of such a configuration lies in the controller's bandwidth. Secondly, the Antagonistic-controlled stiffness principle was inspired by the biological muscular system of human, where two muscles coactively govern the movement of one joint. Previous studies revealed that in order to be able to control the stiffness in a system exploiting such principle, non-linear elastic element is necessary [152–154]. Instead of adjusting the stiffness of the elastic element, structure controlled stiffness principle exploits the benefit in changing of the structures and properties of different elestic elements. One interesting example is "Jack Spring"™[155]. Lastly and seems to be today's most advanced technique in designing a passive compliant actuator is Mechanically controlled stiffness principle. This principle fundamentally exploits mechanical system to adjust the joint's stiffness by altering its state configuration [152]. One of the major challenges in controlling of some of today's passive-compliant actuators, such as: "Series Elastic Actuator (SEA)", is that some extra additional works are often required to adjust and regulate certain parameters, the internal impedance or regulate the position, i.e. stiffness.

The design of the manipulator discussed in this chapter involves two different designs; one with manually adjustable joint stiffness and one with automated joint stiffness control mechanism. The manipulator with manually adjustable joint stiffness will be used in the experiments investigating the influence of variable joint stiffness on the information gain during the estimation of its own internal variable and exploration of the external environment. In addition, it was shown in previous chapter that humans regulate their finger's stiffness during their exploratory process. Therefore, to abstractly replicate similar stiffness regulation during

the exploratory process, the manipulator, which will be used in the experiment as a robotic probe, with automated stiffness control mechanism shall be used in later experiments to verify and investigate the influence of such behavior on the estimation of external environmental variable.

4.2 Two-link manipulator with variable stiffness joint

4.2.1 Design

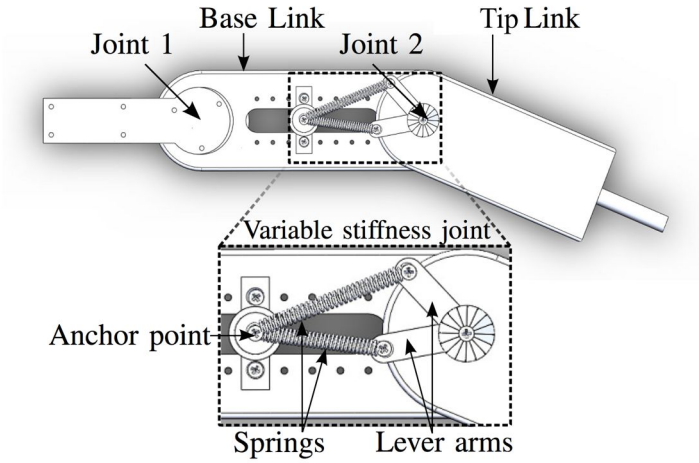

Fig. 4.1 Three dimensional design (Top view) of the antagonistic manipulator. The design comprises of two links and a variable stiffness joint (VSJ) in between. The force sensor is attached to the end of the base link. The stiffness of the joint can be controlled by changing the position of the anchor point and the opening angle of both lever arms.

Design of the first version of antagonistic manipulator presented in this chapter consists of two manipulator links - a base link of length $l_1 = 15$ cm, a tip link of length $l_2 = 17$ cm, and a variable stiffness joint (VSJ) between the two links as shown in Figure 4.1. Since the purpose of this manipulator is to be used in series of experiments investigating the effect and influence of the joint's stiffness on perception, the design of the manipulator represents the abstract version of human's controllable stiffness limb, like finger, and therefore comprises of only a single variable stiffness joint. The design of the VSJ in this platform is based on the "Mechanically Controlled Stiffness" approach [156]. The length of each lever arm in the

controllable stiffness joint is, $d_l = 3$ cm. The spring constant of both springs used in the experiment is $k_s = 0.7$ N/m. As depicted in Figure 4.1 the stiffness rating of the joint, K_s can be controlled by pre-loading the springs through changing the position of the anchor point, r_a, and changing the opening angle of lever arms, α. Apart from ball bearings, the whole system is designed in SolidWorks and fabricated from ABS plastic using the Dimension SST768 3D-printer.

4.2.2 Variable joint stiffness

From figure 4.2, the distance between the axis of the pivot joint and the anchor point of the two springs at rest is denoted by l_d. The resting lengths of each spring are equal and denoted as r. The length of the lever arms connected at the two free ends of the springs are $d_l = 3$ cm. The changes in the length of each spring are denoted by Δr_1 and Δr_2.

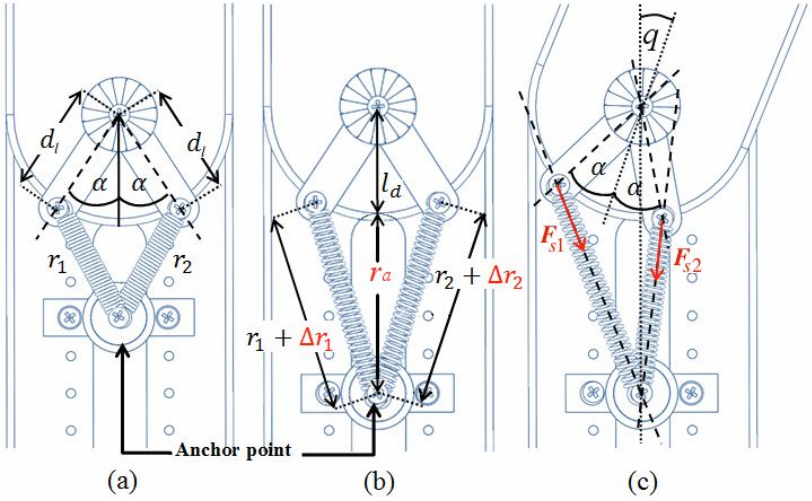

Fig. 4.2 Top view of the manipulator, focusing on the variable stiffness element at the joint. (a) Joint stiffness configuration, when $q = 0$ and the stiffness elements are mounted at the origin point. (b) Joint stiffness configuration, when $q = 0$ and both springs are extended by moving the anchor point. (c) Second joint is rotated at particular angle q.

From figure 4.2 (a), the resting lengths ($r_1 = r_2 = r$) of both springs can be computed as given by

$$r = \sqrt{{l_d}^2 + {d_l}^2 - 2 d_l l_d \cos\alpha}. \tag{4.1}$$

Hence, from figure 4.2 (b) and (c), the resulting length of both springs due to the change of both joint angular position, q, and the position of the anchor point, r_a, can be obtained as following.

$$\begin{aligned} r + \Delta r_1 &= \sqrt{(l_d + r_a)^2 + {d_l}^2 - 2d(l_d + r_a)\cos(\alpha + q)} \\ r + \Delta r_2 &= \sqrt{(l_d + r_a)^2 + {d_l}^2 - 2d(l_d + r_a)\cos(\alpha - q)} \end{aligned} \tag{4.2}$$

Given that each spring constant k_s of the stiffness elements are known, the force contribution $\boldsymbol{F}_{s1,2}$ by each spring at the pivot can be calculated based on the kinematic relations shown in figure 4.2 (c) as given by

$$\boldsymbol{F}_{s1,2} = \Delta r_{1,2} k_s. \tag{4.3}$$

Hence, the torques around the pivot axis developed by both stiffness elements can be found by

$$\tau_{s1,2} = \boldsymbol{F}_{s1,2} \times (l_d + r_a) = \boldsymbol{F}_{s1,2\perp}(l_d + r_a), \tag{4.4}$$

where $\boldsymbol{F}_{s1,2\perp}$ is the force acting perpendicular to the base link at the pivot joint given by

$$\frac{d_l \sin(\alpha + q)}{r + \Delta r_1} = \frac{\boldsymbol{F}_{s1\perp}}{\boldsymbol{F}_{s1}} \rightarrow \boldsymbol{F}_{s1\perp} = \boldsymbol{F}_{s1} \frac{d_l \sin(\alpha + q)}{r + \Delta r_1}, \tag{4.5}$$

$$\frac{d_l \sin(\alpha - q)}{r + \Delta r_2} = \frac{\boldsymbol{F}_{s2\perp}}{\boldsymbol{F}_{s2}} \rightarrow \boldsymbol{F}_{s2\perp} = \boldsymbol{F}_{s2} \frac{d_l \sin(\alpha - q)}{r + \Delta r_2}. \tag{4.6}$$

From equations (4.4), (4.5), and (4.6), the stiffness-element-contributed torque perceived at the base link can then be computed as given by

$$\tau_{s1} = \boldsymbol{F}_{s1} \frac{d_l \sin(\alpha + q)}{r_1 + \Delta r_1}(l_d + r_a), \tag{4.7}$$

$$\tau_{s2} = \boldsymbol{F}_{s2} \frac{d_l \sin(\alpha - q)}{r_2 + \Delta r_2}(l_d + r_a), \tag{4.8}$$

$$\tau_s = \tau_{s1} + \tau_{s2}. \tag{4.9}$$

Hence, the stiffness rating, K_s, can be computed from the derivatives of the torque contributed by variable stiffness mechanism, τ_s, with respect to the angular displacement, q:

$$K_s = \frac{\partial \tau_s}{\partial q}. \tag{4.10}$$

The simulation was carried out by changing the pre-tension state of $r_a \in (4:8)$ cm for $\alpha = 55°$ and $25°$ in order to ascertain the landscape of the joint torque contributed by controllable stiffness mechanism τ_s as a function of relative angular displacement q of the tip link and the pre-tension state r_a of the stiffness element. Figure 4.3 shows that the level of non-linearity in this landscape tends to decrease to almost a linear one when the angular configuration of the two lever arms α reduces.

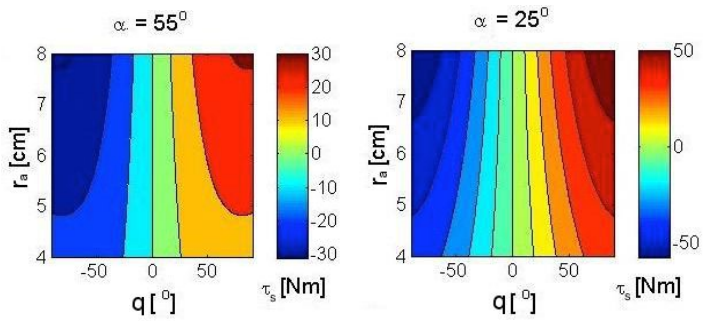

(a) (b)

Fig. 4.3 Contour plot of the torque contributed from the variable stiffness mechanism as r_a varies from 4 to 8 and $q = -90°, .., 90°$, when (a) $\alpha = 55°$ and (b) $\alpha = 25°$

4.3 Robotic probe with controllable stiffness joint and behavioral variables

4.3.1 Design

The purpose of developing this novel biologically-inspired controllable stiffness robotic manipulator was to be used as a robotic probe to palpate a soft object to understand the role of internal stiffness control on haptic perception. The design of this robotic probe was inspired by human's finger. It represents an abstracted version of human's finger with the main focus

on the variable joint stiffness. In addition, this design also comprises of an indentation and a velocity controller to allow the investigation of the influence of these variables on the haptic perception as well.

The overall design of the probe discussed in this thesis is depicted in Figure 4.4 (a). It is composed of two rigid links - tip link with length, $l_1 = 80$ mm, and base link with length, $l_2 = 70$ mm - made from ABS plastics. The joint connecting between these two links are coupled with a variable stiffness mechanism comprising of two identical linear ENTEX No.3552 stock springs ($k_s = 0.24$ N/mm) from Advanex Europe Ltd, to represent how antagonistic muscles control the stiffness of biological fingers. Both springs are situated in spring chambers inside the base link and suspended between the pivot joint (at the connecting location, at which the relative angle to the vertical axis of the tip link is zero) and the movable anchor ring through a micro-filament thread (see Figure 4.4 (b)). The stiffness of the joint can be regulated by changing the position of the anchor ring, r_a, which is controlled by a 50 mm-linear actuator L12-50-210-06-I (Firgelli Technologies Inc., repeatability of ± 0.3 mm). A six-axis ATI Nano17 Force/Torque (F/T) transducer (SI-12-0.12, ATI Industrial Automation, USA, resolution of 0.015 Nmm) is mounted at the top-end of the base link to measure the torque during the interaction with soft silicon phantom. This represents how the tendon sensor is located at the top end of a natural muscle.

The probe's indentation level, i, is controlled by a 30mm-linear actuator L12-30-100-06-I (Firgelli Technologies Inc., repeatability of ± 0.3 mm) mounted at the top of the base link. The total length of this mechanism when at rest is denoted by l_o and has the initial value of 140mm. Hence the total rest length of this probe when the angle of pivot joint, $q = 0$, is 290 mm. The probe structure is mounted on a flipped ANT130 XY-stage (Aerotech Inc., resolution of 1nm) as shown in Figure 4.4 (c), which allows the planar movement in x- and y-direction at a constant speed.

4.3.2 Variable joint stiffness

The detailed view of the variable stiffness joint is shown in Figure 4.4 (b). At rest (the angular displacement, $q = 0^\circ$ and the position of anchor ring, $r_a = 0$ mm), the rest length of

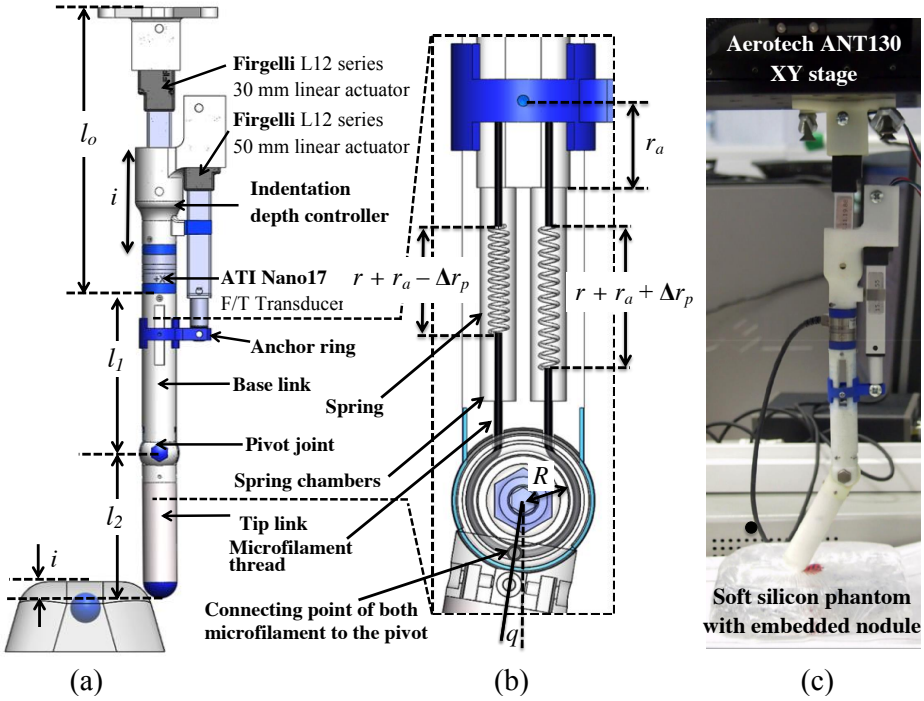

Fig. 4.4 (a) Shaded view of two-link probe's design. (b) Two springs located inside the spring chambers are attached with the anchor ring and the pivot joint through a microfilament thread. (Note that the springs shown here are for illustrative purpose only). The stiffness of the joint can be represented by the distance of r_a. (c) Photo of the complete experimental platform's design comprising of the variable stiffness probe mounted on XY-stage.

both springs are equal and denoted by r. Both springs can be extended from their rest by changing the position of the anchor ring, r_a. The change of the angular displacement of the joint, q, due to the passive interaction with the environment, depending on the direction, causes both springs to be compressed and extended by Δr_p, where $\Delta r_p = qR$. R is the radius of the pivot joint at which the microfilament is attached to. Hence the change of the length of the springs can be computed as following:

$$\Delta r_1 = r_a - qR \tag{4.11}$$

$$\Delta r_2 = r_a + qR. \tag{4.12}$$

Since both springs are identical, the force contributed from each spring to the probe's joint can be computed as follows:

$$\boldsymbol{f}_{s1,2} = \Delta r_{1,2} k_s. \tag{4.13}$$

Hence, the torque generated from both springs due to the change of joint's angular displacement and the position of the anchor ring is:

$$\tau_{s1,2} = \boldsymbol{f}_{s1,2} \times R = \boldsymbol{f}_{s1,2\perp} R, \tag{4.14}$$

where $\boldsymbol{f}_{s1,2\perp}$ is the force produced from each spring perpendicular to the rotational axis.

$$\boldsymbol{f}_{s1,2\perp} = f_{s1,2} \sin(q). \tag{4.15}$$

Therefore, the total torque developed due to both springs can be computed from Equation (4.13) to (4.15) as follows:

$$\begin{aligned} \tau_s &= \tau_{s1} + \tau_{s2} \\ &= R k_s \sin(q)(\Delta r_1 + \Delta r_2) \end{aligned} \tag{4.16}$$

and the stiffness at the joint, K_s, is the derivatives of torque produced with respect to the angular displacement of the pivot joint, q, from Equation (4.16)

$$K_s = \frac{\partial \tau_s}{\partial q} = 2 r_a R k_s \cos(q). \tag{4.17}$$

From Equation (4.16) and (4.17), the torque, τ_s, as well as the resulting joint stiffness, K_s, were simulated as the probe's variable stiffness joint undergoes the changes in the angular displacement of the pivot joint, q, and the linear displacement of the anchor ring, r_a. The simulation results shown in Figure 4.5 are generated from the following parameters: $r_a \in (0 : 15)$ mm, $R = 6.8$ mm, $q \in (-90 : 90)^\circ$, and $k_s = 0.24$ N/mm.

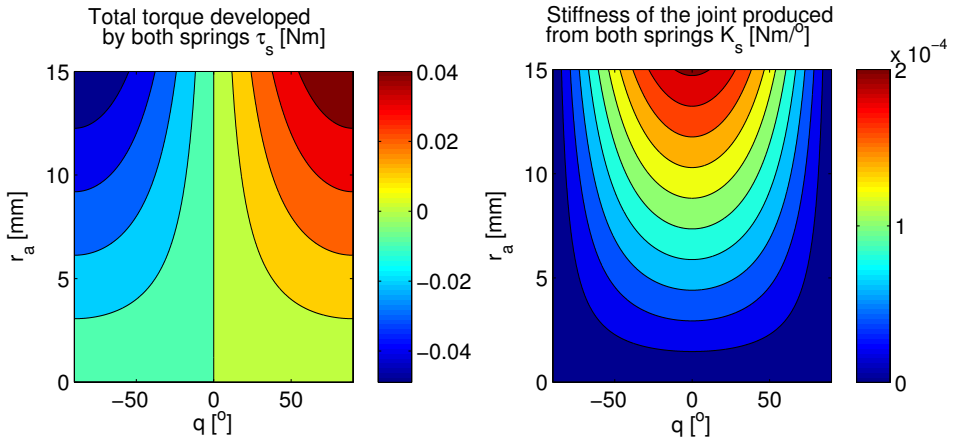

(a) (b)

Fig. 4.5 Torque (a) and the stiffness (b) produced at the pivot joint due to the changes in the displacement of the anchor ring, r_a, and the angular displacement of the joint, q

The resulting joint torque due to the changes of both parameters, q and r_a, is shown in Figure 4.5 (a). The extension of both springs by increasing r_a results in a change of the landscape of the relationship between τ_s and q. Taking derivatives of the simulated joint torque with respect to the angular displacement of the pivot joint results in the stiffness profile of the joint shown in Figure 4.5 (b). The stiffness of the joint becomes almost linear as the anchor ring approaches its origin. Since r_a can be controlled through the linear actuator, for the rest of this chapter, the joint's stiffness level is represented in term of the position of the anchor ring, r_a [mm].

4.3.3 Dynamics of two-link manipulator

The description of variables used in the system depicted in Figure 4.6 is shown in Table 4.1. The joint coupled between the tip and base link comprises of a variable stiffness element, which is represented by a variable spring-damper system. According to the derivation shown in Equation (4.17), the variable joint's stiffness, $K_s(r_a, q)$, is therefore a function of the position of anchor ring, r_a, and the angular displacement of the pivot joint, q.

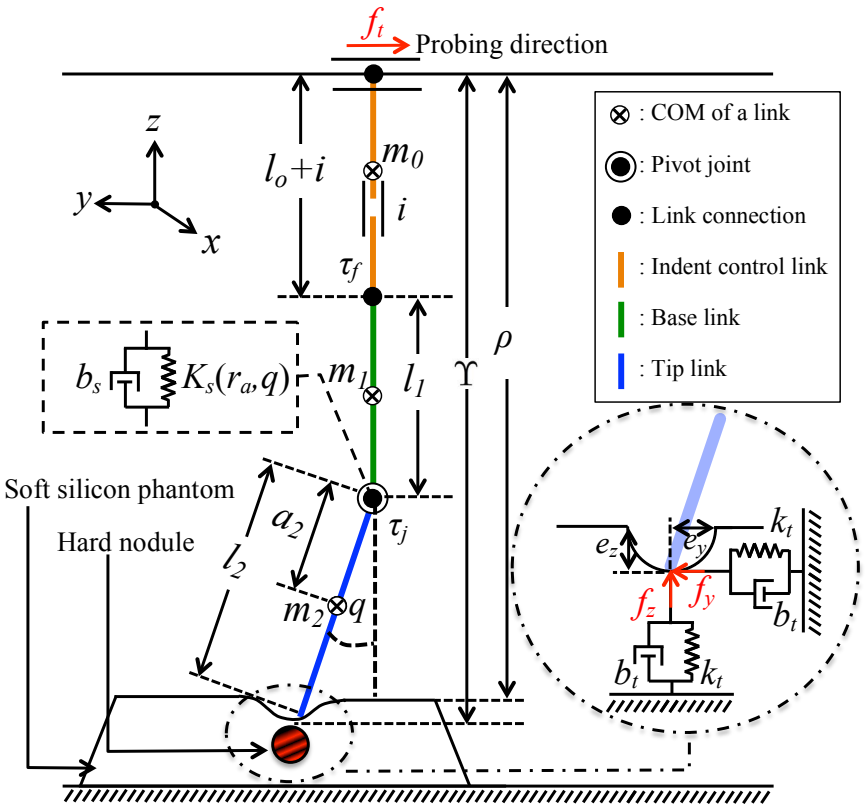

Fig. 4.6 The probe consists of two rigid manipulator links with a variable stiffness joint. In the experiment, τ_f is measured at the end of base link of the probe using ATI Nano17. The nodule embedded inside the phantom is shown in red-black spherical ball. The physical properties of phantom is described using spring-damper system. The variables used in the system is described in table 4.1

Equation of motion

The interaction dynamics of the system can be derived as follows:

$$m_2 a_2^2 \ddot{q} + m_2 g a_2 s + K_s q + b_s \dot{q} = \tau_j, \tag{4.18}$$

where τ_j is the torque at pivot joint. The torque, $\tau = (\tau_f, \tau_j)^\top$ can be resolved from the force components in y- and z-direction, $\mathbf{f} = (F_y, F_z)^\top$, at the probe's tip during the interaction with soft silicon phantom. τ_f denotes the measured torque at the end of base link. The

Table 4.1 System's variables of the probe interacting with soft phantom

System	Variables	Descriptions
Probe	τ_f	Torque measured at the end of base link
	τ_j	Torque at the pivot joint
	q	Angular displacement of pivot joint
	l_o	Length of the indentation control link
	l_1	Total length of base link
	l_2	Total length of tip link
	a_2	Distance to center of mass of tip link
	$m_{0,1,2}$	Mass of indent. control, base, and tip link
	i	Indentation
	g	Gravitational constant [9.81 ms^{-2}]
	b_s	Damping coefficient of variable stiffness joint
	$K_s(r_a, q)$	Joint's variable stiffness rating
	ρ	Distance from XY table to phantom's surface
	$e_{y,z}$	Phantom's deformation in y- and z-direction
	Υ	$\rho + e_z$
	f_t	Translational force in probing direction
Phantom	b_t	Damping coefficient of silicon phantom
	k_t	Stiffness of silicon phantom
	f_y	Restoring force from phantom in y-direction
	f_z	Restoring force from phantom in z-direction

descriptions of the variables used here are explained in Table 4.1. Note that in this thesis, the trigonometric functions are abbreviated as follow: $s = \sin(q)$ and $c = \cos(q)$.

In order to simplify the dynamic equations of the system, the restoring force of the silicon phantom on the probe during the interaction can be modeled using a linear spring-damper system, where the stiffness of the silicon depending on different depth levels of a hard nodule embedded in the sample phantom can be represented by varying the system's spring constant.

Assume that:

1. At rest (no contact between probe and sample phantom) the probe has length of $L = l_o + l_1 + l_2 + i$.

2. The base of the probe is fixed directly above the sample phantom at distance ρ.

3. The probe has stiffness K_s as a function of r_a and q.

4. The soft silicon phantom has uncertain stiffness k_t with Gaussian distribution.

5. The restoring force from the soft silicon phantom is in both y and z-direction.

6. The friction between the tip and soft phantom's surface is negligible.

7. The deformation of soft silicon phantom has a uniform curvature [157].

When the probe comes in contact with the sample phantom, both the probe and the phantom deform according to their relative stiffness as shown in Figure 4.6.

The depth of phantom sample deformation in y- and z-directions are denoted by e_y and e_z respectively. The probe length (compressed prismatically), Υ, can be expressed as a function of q as

$$\Upsilon = l_o + i + l_1 + l_2 c. \tag{4.19}$$

Since the base of the probe is fixed, the constraint

$$|e_z| = \Upsilon - \rho \tag{4.20}$$

is maintained. Furthermore, the deformation of the soft silicone phantom is assumed to have a uniform curvature (the magnitude of deformation in both y- and z-directions are equal). Therefore:

$$|e_y| = |e_z|. \tag{4.21}$$

By substituting equation (4.19) in equation (4.20), these can be obtained:

$$|e_y| = |e_z| = (l_o + i + l_1 + l_2 c) - \rho \tag{4.22}$$

$$\dot{e_y} = \dot{q} l_2 c \tag{4.23}$$

$$\dot{e_z} = -\dot{q} l_2 s. \tag{4.24}$$

The restoring force from the soft silicon phantom on the probe in both directions can be modelled as a spring-damper system as follows:

$$f_y = k_t e_y + b_t \dot{e_y} \tag{4.25}$$

$$f_z = k_t e_z + b_t \dot{e_z}. \tag{4.26}$$

Substituting equation (4.22) - (4.24) in (4.25) and (4.26), the restoring force can be obtained:

$$f_y = k_t(l_o + i + l_1 + l_2 c - \rho) + \dot{q} l_2 b_t c \tag{4.27}$$

$$f_z = k_t(l_o + i + l_1 + l_2 c - \rho) - \dot{q} l_2 b_t s. \tag{4.28}$$

Therefore the force component due to the interaction with soft silicon phantom at the tip is $\mathbf{f} = (F_y, F_z)^\top$, where

$$F_y = f_y - f_t$$

$$F_y = f_y - (m_0 + m_1 + m_2)\ddot{y} \text{ and} \tag{4.29}$$

$$F_z = f_z. \tag{4.30}$$

F_y and F_z are net force in y- and z-direction. f_t is the translational force in probing direction. $\ddot{y}$ denotes the translational acceleration. Note that f_y and f_z contain variables, dependent on the terms indicated, since it is a function of the random variable k_t. The terms $r_a, q, \dot{q}$, and i, can be thought of as parameters to the distribution. Adjusting any of these may have an effect on the information in samples of $\mathbf{f}$.

Torque measurement model

In the design of the probe shown in Figure 4.4 (a), torque, τ_f, is measured at the end of the base link. The Jacobian matrix, $\mathbf{J}$ of the system can therefore be expressed as:

$$\mathbf{J} = \begin{pmatrix} l_1 + l_2 c & l_2 c \\ -l_2 s & -l_2 s \end{pmatrix}. \tag{4.31}$$

The equations of torque resulting from the interaction with the soft silicon phantom can be computed as follows:

$$\boldsymbol{\tau} = \mathbf{J}^{\top}\mathbf{f}$$
$$\boldsymbol{\tau} = \begin{pmatrix} \tau_f \\ \tau_j \end{pmatrix} = \begin{pmatrix} l_1 + l_2 c & -l_2 s \\ l_2 c & -l_2 s \end{pmatrix} \begin{pmatrix} F_y \\ F_z \end{pmatrix}. \tag{4.32}$$

Hence the torque measured by the ATI Nano17 transducer mounted at the end of the base link can be derived as:

$$\tau_f = F_y(l_1 + l_2 c) - F_z l_2 s. \tag{4.33}$$

4.3.4 Simulation: Robotic palpation on soft silicone phantom

According to equations (4.18) and (4.33), the torque response due to the interaction between the probe and soft tissue is dependent on the soft silicon phantom's stiffness k_t, probe's stiffness r_a, and indentation level i. This simulation explores how different probing conditions such as: probe's joint stiffness, indentation, and PSV would affect the distribution of torque response at the probe's base during interaction with different phantom stiffness levels.

Table 4.2 Simulation parameters for robotic probe

System	Variables	Value
Probe	$l_{1,2}$	80, 70 [mm]
	$a_{1,2}$	40, 35 [mm]
	$m_{1,2}$	0.2, 0.3 [kg]
	b_s	0.02 [Ns/m]
	i	{3, 5, 7, 9, 11} [mm]
	v_{probe}	{10, 20, 30} [mm/s]
Joint Stiffness	R	6.8 [mm]
	r_a	{0, 4, 8, 12, 16} [mm]
	k_s	0.24 [N/mm]
Silicon Phantom	ρ	290 [mm]
	k_{tn}^m	{75, 85, 95, 105} [N/m]
	k_{to}^m	65 [N/m]
	$k_{tn,to}^s$	13.2 [N/m]
	$b_{tn,to}$	0.1[Ns/m]

The expected value of the stiffness of the phantom, k_{to}^m, is identified to be 65 N/m with a standard deviation of 13.2 N/m. The source of uncertainty in the simulation is limited to that from the phantom's stiffness. Based on the previous studies [41, 158], the variability of the phantom's stiffness can be approximated to be a Gaussian distribution, $k_t \sim N(k_t^m, k_t^{s2})$, with expected value, k_t^m, and standard deviation, k_t^s. The changes in phantom's stiffness, $\Delta k_t^m = k_{tn}^m - k_{to}^m = 10, 20,$ 30, and 40 N/m, represent the presence of a hard nodule at different depths respectively. The length of the nodule can be viewed as the contact duration with the probe; hence the longer this is, the slower the PSV (v_{probe}). In the simulation, v_{probe} is classified in three levels, namely: slow (10 mm/s), medium (20 mm/s), fast (30 mm/s).

The models of tissue's stiffness, in which the nodule is present, are given by

$$k_t^m = \begin{cases} k_{to}^m & \text{if } 0 \leq t < t_i \text{ and } t \geq t_f \\ k_{to}^m + \Delta k_t^m \sin \frac{\pi(t-t_i)}{t_f - t_i} & \text{if } t_i \leq t < t_f \end{cases}$$

where

$$t_i = \frac{1}{2}\frac{L_t}{v_{probe}} \text{ and } t_f = t_i + \frac{l_n}{v_{probe}}. \tag{4.34}$$

$L_t = 200$ mm, $l_n = 15$ mm, and t represent the length of the simulated phantom along the probing path, the diameter of the simulated nodule, and the simulation time respectively. t_i and t_f denote the time at which the probe's tip first contacts and leaves the nodule's area on the phantom's surface respectively. The dynamic torque response, τ_f, during interaction between the probe and the phantom was simulated under different conditions specified in table 4.2. The simulations were carried out using "ode45" in MATLAB R2013b, The Mathworks, Inc.

The sample of torque responses, τ_f, and the variability resulted from the variability presented in the stiffness of the soft silicon phantom undergoing different interaction conditions across 25 simulation trials are shown in Figure 4.7 (a-d). Figure 4.7 (a) represents the torque responses for different soft silicon phantom's stiffness, $k_{tn}^m = \{75, 85, 95, 105\}$ N/m; whereas the probe's internal stiffness, indentation level, and PSV are fixed. This shows the monotonic increase in torque response as the stiffness of the phantom increases. Figure 4.7 (b) to

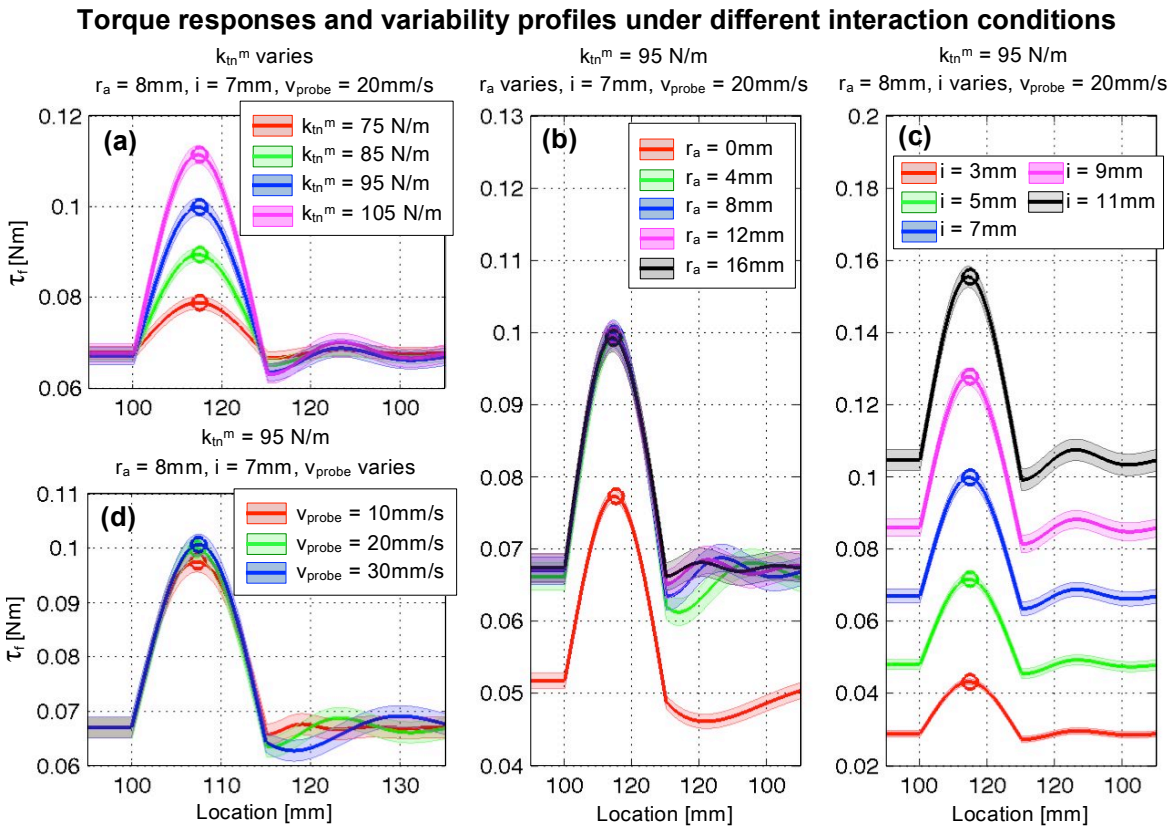

Fig. 4.7 The simulated spherical hard nodule is presented at location between 100 mm to 115 mm. The simulated interaction conditions for each sub-figure are as follows: (a) The average stiffness of soft silicon phantom is varied with the other parameters fixed at $r_a = 8$ mm, $i = 4$ mm, and $v_{probe} = 20$ mm/s. (b) Average Stiffness of the probe is varied keeping the other variables fixed at $k_{tn}^m = 95$ N/m, $i = 4$ mm, and $v_{probe} = 20$ mm/s. (c) The indentation level of the probe, i, is varied keeping the rest parameters fixed at $k_{tn}^m = 95$ N/m, $r_a = 8$ mm, and $v_{probe} = 20$ mm/s. (d) The probe sweeping velocity (PSV), v_{probe}, is varied and the other parameters are kept at $k_{tn}^m = 95$ N/m, $r_a = 8$ mm, and $i = 4$ mm. For each torque profile measured during palpation, the maximum torque at the location of simulated hard nodule is extracted.

(d) represent the torque responses for different combinations of probe's internal stiffness, indentation level, and PSV. As can be seen in Figure 4.7 (b), τ_f increases as the internal stiffness of the probe (controlled by the position of anchor ring, r_a) increases from r_a=0 to 4 mm. After that, τ_f tends to settle down. The increase of the probe's indentation level also elevates the torque responses as shown in Figure 4.7 (c). In Figure 4.7 (d), the influence of the PSV, v_{probe}, on the torque response, given the fixed values for the rest of the simulation parameters, cannot be visually assessed. Therefore, a statistical analysis was

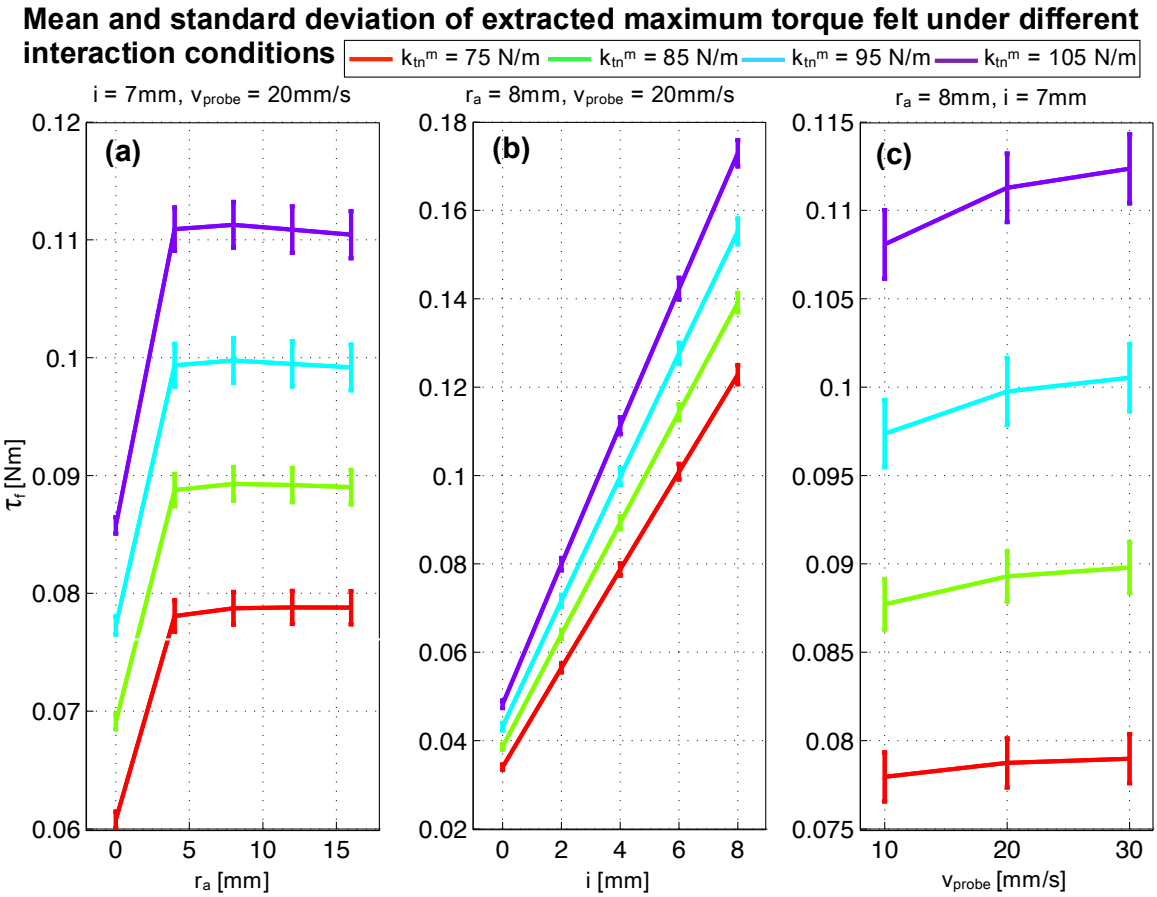

Fig. 4.8 The average maximum torque felt with error bars, under different combinations of probe's internal stiffness, indentation, and PSV, given different stiffness of soft silicone phantom with embedded hard nodule. (a) the probe's stiffness was varied, (b) the indentation level was varied, and (c) the PSV was varied.

applied to determine this. Since the simulated torque response is normally distributed (this was tested using Kolmogrov-Smirnov test for normality), ANOVA (Analysis of Variance) test was implemented. The result from the test signifies no statistically significant difference between these torque response distributions ($p > 0.05$). Therefore, the change in PSV, v_{probe} does not significantly affect the torque response.

From each torque response profile measured during palpation, the maximum torque at the location of simulated hard nodule was extracted as shown in 'circle' in Figure 4.7 (a-d). Figure 4.8 (a-c) depict the expected values and standard deviations of extracted maximum torque response given different combinations of probe's internal stiffness, indentation level, and PSV across 25 trials for $k_{tn}^m = \{75$(red line), 85(green line), 95(blue line), and 105(purple

line)} N/m. Figure 4.8 (a) presents the average maximum torque with standard deviation extracted from 25 simulation trials across different probe's internal stiffness levels presented by r_a. The average torque response increases as r_a increases from 0 to 4 mm. Then the average peak torque response settles down. Furthermore, Figure 4.8 (a) shows non-linear elevation of the torque standard deviation as the probe's stiffness level increases. On the other hand, the average peak torque and the corresponding standard deviation shown in Figure 4.8 (b) respectively tend to have a rather linear trend. Lastly, in Figure 4.8 (c) no statistically significant difference was presented in the average and standard deviation of peak torque response resulted from the change in the PSV.

These simulation results predict that the torque felt at the base of the probe can be controlled using probe stiffness, indentation level and PSV during the interaction with a soft tissue. The relationship between the torque felt and the combinations of probe's stiffness, indentation level, and PSV are non-linear. Furthermore, in reality the variability present in the system is non-deterministic and may arise from several sources such as the probing behavior, environment, and the probe itself. These raise the question as to how these non-linear relationships can be exploited to enhance the interpretation of the features in the environment using proprioceptive feedback from the torque sensor mounted at the base of the probe (representing how the tendon sensor is located in natural muscles). Since the relationship is stochastic and non-linear, the best way to preserve the interaction information is to present the relationship in the form of a probabilistic distribution. It provides us the opportunity to implement an appropriate stochastic machine learning technique to understand the role of individual factor in the interpretation of haptic perception.

4.4 Discussion

This chapter has proposed two different designs of controllable stiffness robotic manipulator. The design of these manipulators are inspired by the way humans observe the proprioceptive information and actively explore the environment through haptic perception. They used the concept of embodiment, where the sensing quality is determined by the level of actuated

joint stiffness. This is similar to human counterpart in the sense that in the proprioception of humans at the finger and arm level, tendon and spindle sensors are carried within the muscle that use to actuate the joint, governing the stiffness of the joints of the arm and finger.

The first version of controllable stiffness robotic manipulator discussed in this chapter presented the design of the variable stiffness joint with non-linear relationship between the stiffness rating and the angular displacement of the joint. The non-linear characteristics offers unique opportunity to implement the information metrics approach to analyse the possible exploitation in observing its own proprioceptive information as well as in the haptic perception. This manipulator platform will be used to investigate how internal impedance can be regulated to enhance the accuracy of proprioception. This is similar to the proprioceptive function of tendon sensor in humans counterparts. This will be explained in Chapter 5. In addition, this manipulator platform will be exploited as a probing device for detection of stiff abnormalities embedded in a soft silicon phantom during palpation in Chapter 6.

The results from the simulation of the controllable stiffness robotic probe explained in Section 4.3 suggest that 1) the torque felt at the base of the probe can be controlled using different combinations of probe's stiffness, indentation level, and PSV and 2) the relationships between the torque measured, the stiffness of the soft silicon phantom, and the combination of probe's internal stiffness, indentation level, and PSV are non-linear. While a variability in the simulated system from the Gaussian distribution of the phantom's stiffness is pre-defined; the variability in such a system in reality is non-deterministic and can arise from multiple sources. These brought into a question as to how these non-linear relationships in the experiment can be used to enhance the estimation of the environmental features. The automated control of the stiffness, indentation level, and PSV allow this robotic probe to perform the automated active haptic exploration similar to the process observed in human during manual palpation. The experiments involving the active haptic exploration with this robotic probe will be discussed in Chapter 7.

Chapter 5

Information gain via an embodiment with variable internal impedance

Abstract— *This chapter explores the role of internal impedance in the accuracy of embodied perception. To investigate this, this chapter poses the problem of using only torque data measured at the stationary base of a two-link controllable stiffness joint planar manipulator, to estimate the deflection caused by an external torque in the McKibben type pivot joint with variable stiffness. Based on experimental validation, this chapter presents, for the first time, that non-linear static memory primitives relating internal impedance, internal kinematic variables, and forces felt at the base of the manipulator - similar to the functionality of tendon organs of biological counterparts - can be used to tune optimal internal impedance parameters to maximize the accuracy of internal state estimation during external perturbations.*

5.1 Introduction

From embodied perception perspective, a major challenge in this study was to investigate how body's internal impedance can be regulated to gain the accurate perception. This chapter focuses on the role of internal impedance modulation in the embodied perception of a simple planar 2-links manipulator system with variable joint stiffness. The experimental results were used to approximate the stiffness calibration curve for different pre-tension states of the stiffness element. The experimental analysis section used the transfer entropy from Kullback Leibler divergence [159] approach as an indicator to the information gain across pre-tension state of the stiffness element. Newton-Raphson optimization [160] and Hooke-Jeeves pattern [161] search were compared to search for the best pre-tension state that maximizes transfer entropy to arrive at the best estimate for angular displacement of a joint between two links given the torque measured at the base.

This chapter is structured as follows. First the experimental platform is described, including the joint stiffness model's numerical simulation, followed by the methodology employed in the experiments. Thereafter, results and analysis are exhibited. The example application of using the ability to vary the internal stiffness of the body is discussed in context of haptic perception of the environment, particularly in the task of physical examination of soft object.

5.2 Experimental setup and methodology

5.2.1 Experimental setup

A design of the antagonistic manipulator used in the experiment consists of two manipulator links - base link of length $l_1 = 15$ cm, and an tip link of length $l_2 = 17$ cm. The design of the variable joint stiffness (VSJ) in this platform was based on the "Mechanically Controlled Stiffness" approach [156]. It comprises of two linear springs with spring constant rating of 0.007 N/m. The stiffness of the McKibben type pivot joint between these two links can be adjusted by moving the anchor point of the two springs as shown in Figure 5.1. Further

detail regarding the variable joint stiffness design can be found in Section 4.2.2. The angle α between each lever arm and the center of link 2 were pre-configured to $\alpha = 55°$; and the springs can be pre-loaded by changing the position of the anchor point, r_a. The system was mounted on a table and fixed with a clamp underneath. Apart from ball bearings, the whole system was designed in SolidWorks and fabricated from ABS plastic using the Dimension SST768 3D-printer. This experiment focused mainly on the perception of the angular displacement q of the tip link relative to the base link based on the torque τ_f sensed at the base of the manipulator around z-axis using a ATI Mini40 six axis force/torque (F/T) transducer (SI-20-1 from ATI Industrial Automation, resolution around z-axis: $1.25e^{-4}$ Nm) at 100 Hz. For verification of the accuracy of estimating q, an XSENS MTx wireless motion capturing sensor (Xsens Technologies B.V., angular resolution: 0.05°) sampled at 100 Hz was used as shown in Figure 5.1.

5.2.2 Methodology

The main purpose of the experiment presented in this chapter was to examine the role of body internal impedance in an accurate embodied proprioception. In this case, the experimental study was limited to embodied perception during slow movements, so that a static calibration of sensors can be used in a dynamic condition as static memory primitives of embodiment and kinematic variables. The relative angular displacement of the tip link and the torque felt at the base in a static condition are denoted as q^{sta} and ${\tau_f}^{sta}$ respectively, and those in a dynamic condition are denoted as q^{dyn} and ${\tau_f}^{dyn}$ respectively. This experiment investigated as to how the non-linear relationship between q^{sta} and ${\tau_f}^{sta}$ can be exploited to search for the optimal r_a to maximize information gained about q^{dyn} during a dynamic movement of the tip link (action).

Static movement

As described and illustrated in section 4.2.2, there is a non-linear characteristic presented in the design of variable joint stiffness. In order to identify the landscape of this nonlinear relationship and to construct the static memory primitives for internal state estimation, ${\tau_f}^{sta}$

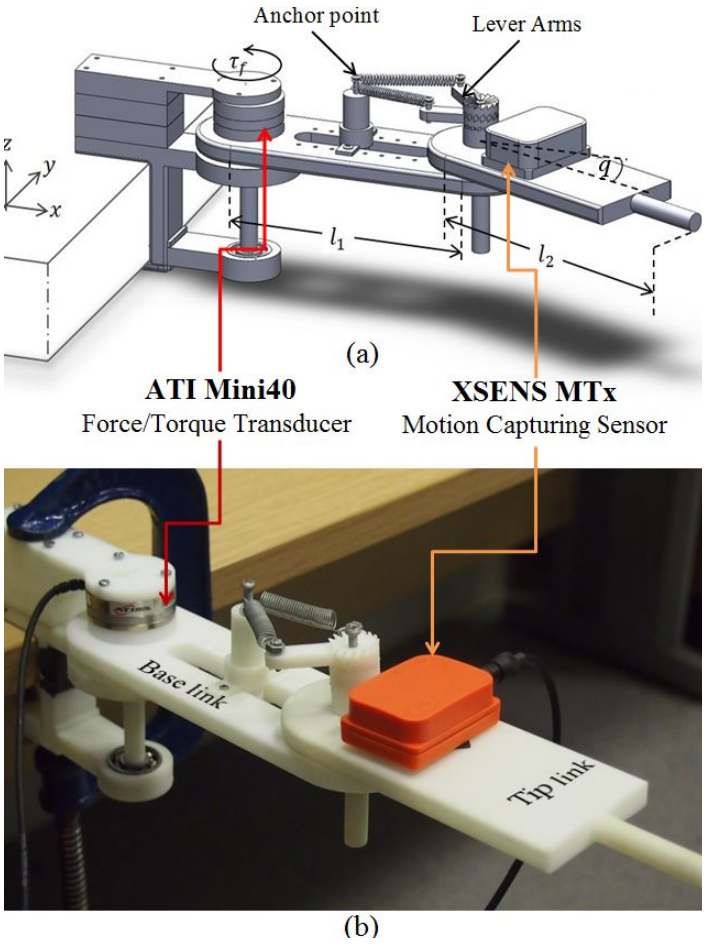

Fig. 5.1 (a) a design of two-links planar manipulator with a variable stiffness joint (VSJ). The rotational displacement of the tip link, q, is recorded using an XSENS MTx Motion Capturing sensor; whereas the torque experienced at the base of the manipulator during such movement is measured by ATI Mini40 6-axis Force/Torque Transducer, (b) a photo of the experimental platform attached on the table with a clamp.

and q^{sta} were recorded for 10 trials for each configuration of the stiffness element for statistic evaluation. The static torque ${\tau_f}^{sta}$ was measured at different pre-tension states, $r_a = 4$ cm to 8 cm at different q^{sta} values. Measurements were taken after leaving the system to settle down to a steady state (ex. after the vibrations in the springs were damped out). For each trial, the recorded data was mapped using a third order best fit polynomial function. Figure 5.2 (a) show the variability of the fitted torque data across 10 trials for each configuration of stiffness element, $r_a = 4$ cm to $r_a = 8$ cm.

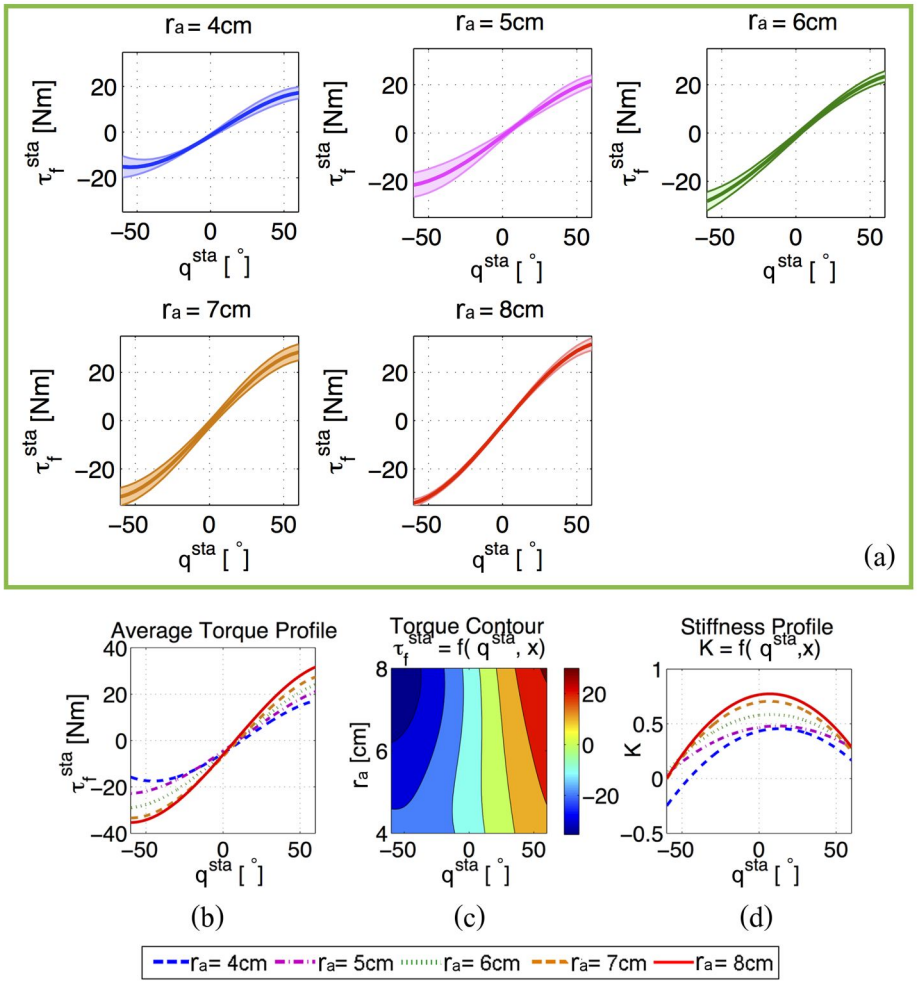

Fig. 5.2 (a) The variability of torque perceived at the base across 10 trials for different pre-tension states r_a. (b) best fit thrid order polynomials to ${\tau_f}^{sta}$ vs ${q}^{sta}$ primitives across different $r_a \in [4, \cdots, 8]$cm in blue, magenta, green, orange, and red lines respectively, (c) the corresponding contours of the approximated torque profile, (d) the rotational spring constant profile.

The average torque profile ${\tau_f}^{sta}$, from all 10 trials is shown in 5.2 (b), from which the corresponding contour representing the non-linear static memory primitives can be constructed. It should be noted that the experimental results shown in Figure 5.2 (c) is comparable to that obtained in numerical simulation shown in Figure 4.3 (a) (average probability of the hypothesis that the columns of Figure 5.2 (c) are the same as those in Figure 4.3 (a), is statistically significant in Mann-Whitney U test), confirming the validity of the analytical model presented in previous Chapter 4, Section 4.2.2.

From the relationship between the torque experienced at the base and the relative angular displacement of the tip link, the joint stiffness rating, $K_s(q^{sta})$, can be obtained from the tangent of the function of torque with respect to the angular displacement at any given q^{sta} as given by:

$$K(q^{sta}) = \frac{\partial {\tau_f}^{sta}}{\partial q^{sta}}. \tag{5.1}$$

The resulting rotational spring constant profile $K(q^{sta})$ is shown in Figure 5.2 (d).

Dynamic movement

As stated earlier, the main objective of this experiment was to explore the influence of internal impedance on dynamic behaviour of perception. Therefore, the dynamic torque, ${\tau_f}^{dyn}$, and angular displacement, q^{dyn} were recorded at different pre-tension states r_a, during dynamic movement. The dynamic movement trial was carried out by releasing the tip link from a certain angle, i.e. $q = 75°$. Data were recorded until the system was settled down to its steady state where $q = 0$. An example of such movement is illustrated in Figure 5.3. The measured torque versus rotational displacement trajectory was mapped using a third order best fit polynomial function as shown in Figure 5.4 (a) for each joint stiffness configuration, $r_a = 4, \cdots, 8$ cm.

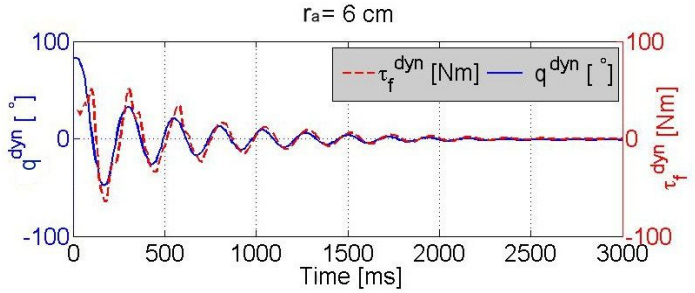

Fig. 5.3 ${\tau_f}^{dyn}$ and q^{dyn} profiles during the dynamic movement for pre-tension state $r_a = 6$ cm

5.3 Results

5.3.1 Perception information gain with transfer entropy

If τ_f was considered as a random variable, its entropy for a given q depends on the pre-tension state r_a. Therefore, the transfer entropy defined in equation (5.2) - additional information gained about the relationship between τ_f and q by changing the pre-tension state r_a - is a good indicator to search for an optimum r_a [159].

$$G = P(\tau_f, r_a, q) \log \frac{P(\tau_f | r_a, q)}{P(\tau_f | {r_a}^{ini}, q)}, \tag{5.2}$$

where $G \geq 0$ is the non-negative information gain, $P(\tau_f | r_a, q)$ is the probability distribution of dynamic torque over the pre-tension state r_a and angular displacement q constructed using 10-trials of static torque data, and ${r_a}^{ini}$ is an initial value of r_a. This implies that if information gain $G = 0$, the joint stiffness has no influence on the causal relationship between ${\tau_f}^{dyn}$ and q^{dyn}. In order to find an optimum pre-tension state r_a, the transfer entropy of the angle estimation based on the current torque measurement was computed given the current state of r_a. The estimation process then search for optimum r_a based on the maximum information gain (transfer entropy). The whole process is summarized in algorithm 5.1. The processes for finding maximum information gain are discussed in the following sub-sections.

Algorithm 5.1: Algorithm to find an optimum pre-tension state.

1. **Step 1:** Choose a set of torque data measured during a dynamic movement of the tip link for a randomly chosen initial pre-tension state ${r_a}^{ini}$.
2. **Step 2:** Randomly sample the angular displacement q^{dyn} of the tip link using the relationship corresponding to the ${r_a}^{ini}$, established in Figure 5.4 (a).
3. **Step 3:** Construct entropy profile based on ${\tau_f}^{dyn}$ retrieved from random parameters in *Step 1* and *Step 2*, together with the non-linear static memory primitives established in Figure 5.2 (b), and (c).
4. **Step 4:** From transfer entropy profile shown in Figure 5.4 (b), search for the best r_a that would maximize the transfer entropy G profile across r_a using search algorithms described in section 5.3.2 (Figure 5.5 and 5.6).
5. **Step 5:** Use the optimum pre-tension state ${r_a}^{best}$ to compute the best approximation q^{pred} of a 'real' q^{dyn} given only the torque reading, ${\tau_f}^{dyn}$ using the static memory primitives corresponding to the ${r_a}^{best}$, established in Figure 5.2 (b).

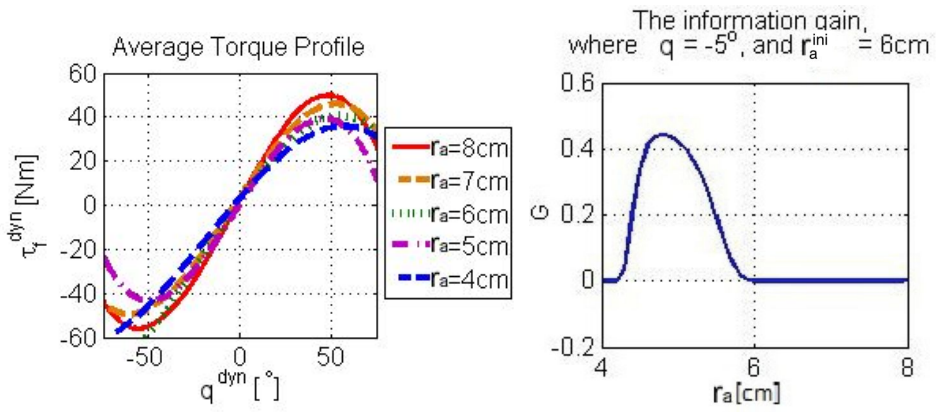

(a) (b)

Fig. 5.4 (a) the best fit third order polynomial functions for the measured dynamic torque profiles, (b) the information gain evaluation with the pre-tension state $r_a = 4 \cdots 8$ cm; the randomly selected initial pre-tension state ${r_a}^{ini} = 6$ cm; and the angular displacement of endeffector, $\theta_2 = -5°$.

5.3.2 Optimization of joint stiffness for optimum proprioception

In this section, the problem of optimizing the joint stiffness for optimum proprioceptive information based on the maximum information gain metrics is investigated. According to the standardized optimization problem [162], this problem can be stated as:

$$\max\left(G(r_a, \tau_f)\right) \tag{5.3}$$

subjected to

$$\min\left(t\right), \tag{5.4}$$

where t represents number of iterations taken for the optimization process to reach the convergence. In this chapter, two different optimization methods were compared, namely: Newton-Raphson optimization method (requires gradient information) and the Hooke-Jeeves pattern search method (does not require gradient information), to search for the best r_a that maximizes transfer entropy G to arrive at a best estimate for q given the torque measured at the base τ_f.

Newton-Raphson optimization

Newton-Raphson optimization method is a technique to find an extrema in a solution space of a function based on a local gradient [160].

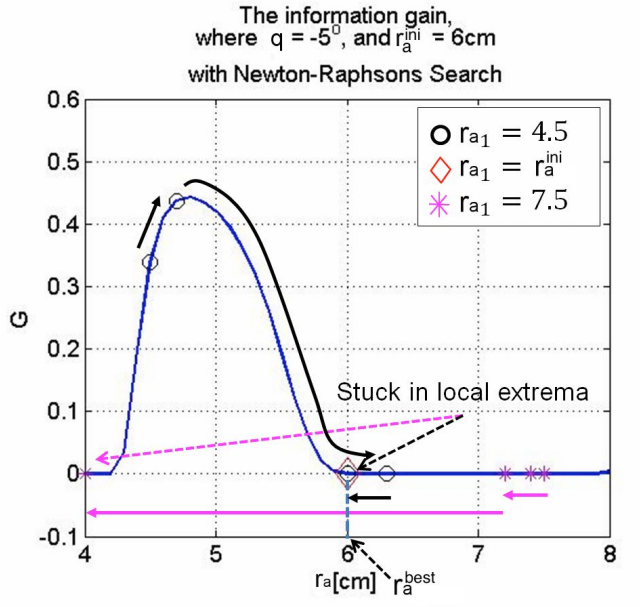

Fig. 5.5 Implementation of Newton-Raphsons optimization method on a transfer entropy profile computed at $q = -5°$, and ${r_a}^{ini} = 6$ cm. The algorithm starts from three different initial points, namely: $r_{a1} = 4.5$ cm (black circle), ${r_a}^{ini}$ (red trapezoid), and 7.5 cm (magenta star) respectively. The search algorithm finishes the iteration in the local minima for all three starting points. Therefore, utilizing this approach yields ${r_a}^{best} \approx 6$.

Figure 5.5 depicts this approach in finding the optimum gain when $q = -5°$, and ${r_a}^{ini} = 6$ cm as an example. The search algorithm for the optimum parameter jumped around across iteration and the solution for the ${r_a}^{best}$ converged to the local minima of the gain profile resulting in ${r_a}^{best} = 6$ cm.

Hooke-Jeeves Pattern Search

Hook-Jeeves Pattern Search is a directional search algorithm to obtain the point in the solution space with best fitness. The algorithm was developed by Hooke and Jeeves in 1961 and can be found in *Appendix B* of their paper [161].

Hooke-Jeeves Pattern Search is suitable for only unimodal search spaces. Handling a multimodal function with this method may cause the algorithm to get stuck in local maxima. This problem can be minimized by introducing the same dual search approach. An example of this Hooke-Jeeves Pattern Search is shown in Figure 5.6 with the parameter of: $q = -5°$, and ${r_a}^{ini} = 6$ cm.

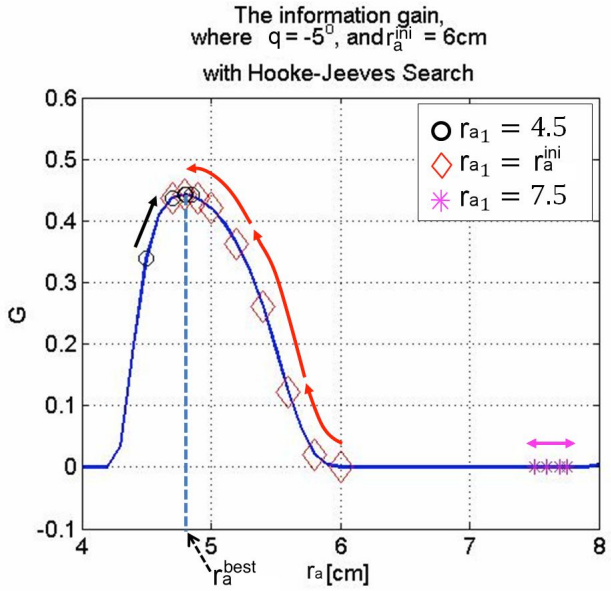

Fig. 5.6 Implementation of Hooke-Jeeves pattern search method on a transfer entropy profile computed at $q = -5°$, and ${r_a}^{ini} = 6$ cm. The algorithm starts from three different initial points, namely: $r_{a1} = 4.5$ cm (black circle), ${r_a}^{ini}$ (red trapezoid), and 7.5 cm (magenta star) respectively. While, the algorithm with starting point, $r_{astart} = 7.5$, gets stuck in the local minima; the rest algorithms converges to the optimum point, ${r_a}^{best} \approx 4.8$, of which G is at the maximum.

The algorithm converged to its maxima of the transfer entropy profile from two starting points, namely: $r_{a1} = 4.5$ cm (black circle), and $r_{a1} = r_a^{ini}$ (red trapezoid); whereas the algorithm got stuck in the local minima for the starting point, $r_{a1} = 7.5$ cm. From this, the optimum stiffness configuration parameter was obtained: ${r_a}^{best} \approx 4.8$ cm.

5.3.3 Results discussion

The performance of each algorithm was evaluated by the average error in approximation of the q state. Hooke-Jeeves pattern search method outperforms the Newton-Raphsons

optimization approach in term of the average error of approximation of q as shown in Figure 5.7 (a). Furthermore, though Hooke-Jeeves optimization required on average more iterations to converge, its corresponding error deviation (shown in error bar) was overall smaller than that of Newton-Raphson Optimization as shown in Figure 5.7 (b).

It is important to note that the experimental results in the optimization part of this chapter was a non-real time simulated case. Therefore, the computational cost appearing here was purely based on the number of iterations alone and not the real-time computational costs. However, since the optimization problem stated in this chapter was relatively simple, which involves the maximization of the information gained; therefore, the number of iterations can be used to reflect the computational costs in this instance.

This chapter provides the experimental evidence as to how the nonlinear memory primitives of embodiment and kinematic variables could be exploited to enhance the accuracy of the estimation of the internal states of the system during the dynamic behaviours through the modulation of the internal impedance. Transfer entropy of embodied perception of the internal state - deflection angle of the McKibben type pivot joint in this case - was used as an indicator in searching for an optimal level of pre-tension state for accurate perception. Alternative approaches were compared to enable real-time search of the optimal internal impedance level, namely: Newton-Raphsons Optimization; and Hooke-Jeeves pattern search approach.

5.4 Application Discussion: Embodied haptic perception of soft object

One of the applications that can exploit the benefit of having the ability to change the internal stiffness of the body in perception, is inspired by biological counterparts like humans during the exploration of the environment using haptic feedback. That is embodied haptic perception. During such activity, human performs muscle activity regulation in both muscle and spindles to condition the proprioceptive feedback. This physical examination of soft object using haptic feedback can be seen in variety of applications like manual palpation

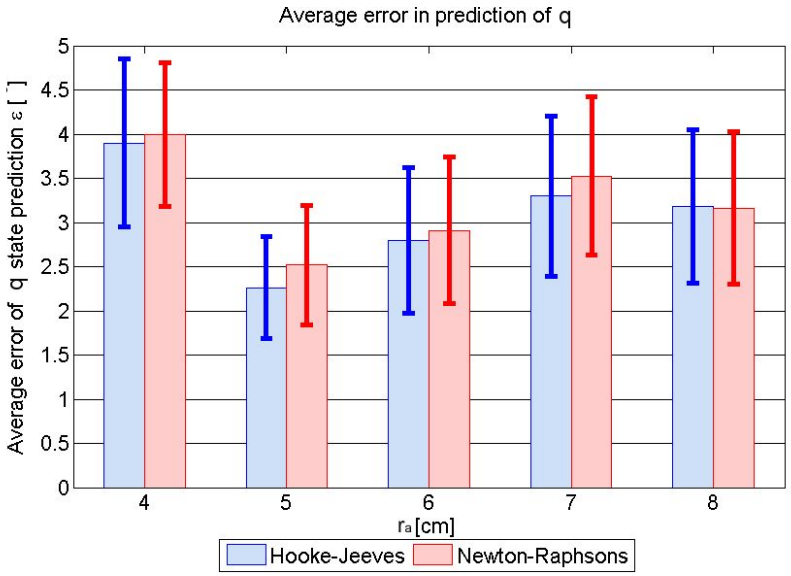

(a)

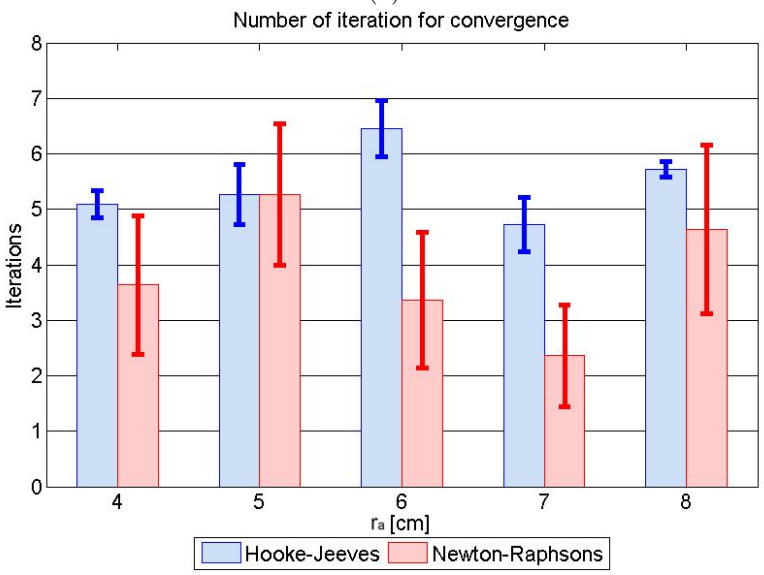

(b)

Fig. 5.7 (a) The average error of angular displacement, ε, is taken from the average error of prediction of state, q^{pred}, with respect to the dynamic angular displacement q^{dyn}, ranging from $-10°$ to $10°$, across ${r_a}^{ini}$. The average error along with corresponding error bars produced using Hooke-Jeeves and Newton-Raphsons approach are shown in blue and pink bars respectively, (b) the average number of iterations required until the alternative algorithms - Hooke-Jeeves pattern search (blue bars) and Newton-Raphson optimization (pink bars) - converge with the error bars.

of soft tissue in surgery, security, quality assurance in food industry, entertainment, and etc. In this discussion, the focus is mainly concentrating on the detection of mechanical stiff inclusion inside a sample soft tissue. In this section, the possible application of using the robotic manipulator with variable stiffness as a soft robotic probe to explore the soft object is discussed.

The purposes of this experiment were to examine: 1) the influence of the internal impedance control on the detection of the hard nodule embedded in soft tissue; and 2) the dynamic torque response and its variability during the interaction with soft tissue with stiff-inclusion given different levels of probe's stiffness. From the results of the experiments with the manipulator with VSJ discussed earlier in Section 5.2.2, it can be seen that there are levels of non-linearity in the relationship between the stiffness of the body and proprioception (Figure 5.2) . This relationship can be used to construct the entropy for the information transfer to maximize the information gain in the embodied perception. This in-turn allows the regulation of the internal impedance to accurately predict the internal kinematic variable of the body itself. Using the similar principle underlying this relationship, this section investigates as to whether this benefit can also be used to enhance the information during the interaction with external environment.

5.4.1 Experiments

The probe used in this experiment was taken directly from the two-link robotic manipulator with VSJ shown in Figure 5.1. In this experiment, the platform was mounted on the ANT130 two-axis linear stage (Aerotech Inc., resolution of 1 nm) installed up side down as shown in figure 5.8 (a). This manipulator platform was used as a probing device for detection and localisation of stiff abnormalities embedded in a soft tissue of ex-vivo porcine kidney.

In order to examine the effect of the joint stiffness on the perception during probing, the torque τ_f sensed at the base of the manipulator around z-axis was measured using a ATI Mini40 six axis force/torque (F/T) (SI-20-1 from ATI Industrial Automation, resolution around z-axis: $1.25e^{-4}$ Nm) transducer at 100 Hz. The linear stage was programmed to run by ensuring the stable contact between the manipulator's end-effector and the probed

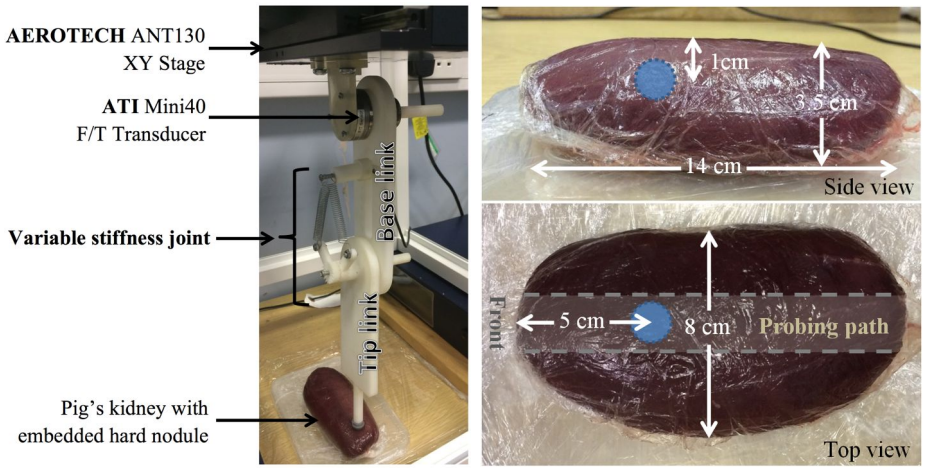

(a) (b)

Fig. 5.8 (a) A photo of an experimental setup, where the manipulator is attached under the ANT130 XY stage from AEROTECH. The torque experienced at the base of the manipulator during the interaction with ex-vivo porcine kidney, is measured by ATI Mini40 six axis force/torque transducer. (b) Ex-vivo porcine kidney used in the experiment. The kidney is 140 mm long, 80 mm wide, and 35 mm thick. The spherical hard nodule made from rubber with diameter of 12 mm is embedded at the depth of 10 mm from the surface and approximately 5 mm from the front of the kidney, where the probing activity starts.

soft-tissue, and the constant indentation of the device during the examination in each trial. The stiffness of the manipulator's joint was changed across trials to examine its effect on the information of the hard-nodule detection.

The probe was allowed to slide along the sample soft tissue at constant speed of 20 mm/s, in which the hard nodules are embedded at 10 mm depth (see figure 5.8 (b) for the dimension of the porcine kidney and the location of the nodules used in the experiment). During the interaction between the manipulator and the soft tissue, the torque information during the movement was recorded for 10 trials for each stiffness level governed by r_a, where $r_a = 4$ cm (low stiffness) to 8 cm (high stiffness).

5.4.2 Preliminary results

The torque information perceived for each stiffness level were averaged from 10 trials and shown in the first row of Figure 5.9 (a). The focus of this discussion was on the dynamic response of the measured torque during the interaction with unknown soft environment to

discern the physical property under different levels of internal stiffness. First, the variability of torque perceived across ten trials for each stiffness configuration was extracted as shown in second row of Figure 5.9 (a). During the interaction with the soft tissue at the location, under which the nodule was embedded, due to the change in the overall physical property of the environment, the torque response and the variability should be affected. Therefore, the gradient (shown in the last row of Figure 5.9 (a)) was extracted from the average torque profile, in order to find the variance change point.

The variance change point can be used to identify any changing point of variability in the signal. Therefore, any pair of variance change points (if they exist) could be used to determine the detection of a hard nodule. In this instance, the variance change point method was applied to the gradient of the average torque signal for each stiffness level. The detected points were indicated using black dots. The average location at which the variance change points were found is summarized in Figure 5.9 (b). It is important to note that, due to the change in the dynamic of the interaction between the probe with different joint stiffness levels and the tissue, the change in the torque response, which signifies the detection of a nodule, can experience a dynamic shift. The increasing trend of the detected datapoint was observed as the stiffness increases from low to high stiffness.

The average and standard deviation of peak torque response around the nodule's location found earlier was extracted and shown in Figure 5.9 (c). As the stiffness increased, the average torque response to the change of the physical property of the environment non-linearly increased; whereas the corresponding standard deviation decreased. These extracted peak torques from all ten trials for each stiffness level were confirmed to be normally distributed using Kolmogrov-Smirnov assessment for normality. The analysis of variance (ANOVA) was applied to the whole set of extracted peak torque to determine whether the stiffness of the probe can affect the dynamic torque response during the nodule's detection. The result from ANOVA test ($p < 0.05$) reveals that the probe's stiffness level plays statistically significant role in the torque response during the palpation to detect the nodule.

These preliminary results illustrate that the torque perceived at the base of the probe can be influenced by the variation of probe's internal stiffness during the interaction with a soft

tissue. The relationship between the torque felt and probe's stiffness level is non-linear. Since the variability experienced in the system is non-deterministic and can arise both individually and collectively from several sources such as the probe, the environment, and the interaction between them. These brought into question as to how the non-linear relationship can be exploited in order to enhance the estimation of the environment using the proprioceptive feedback from the sensor mounted at the base of the probe.

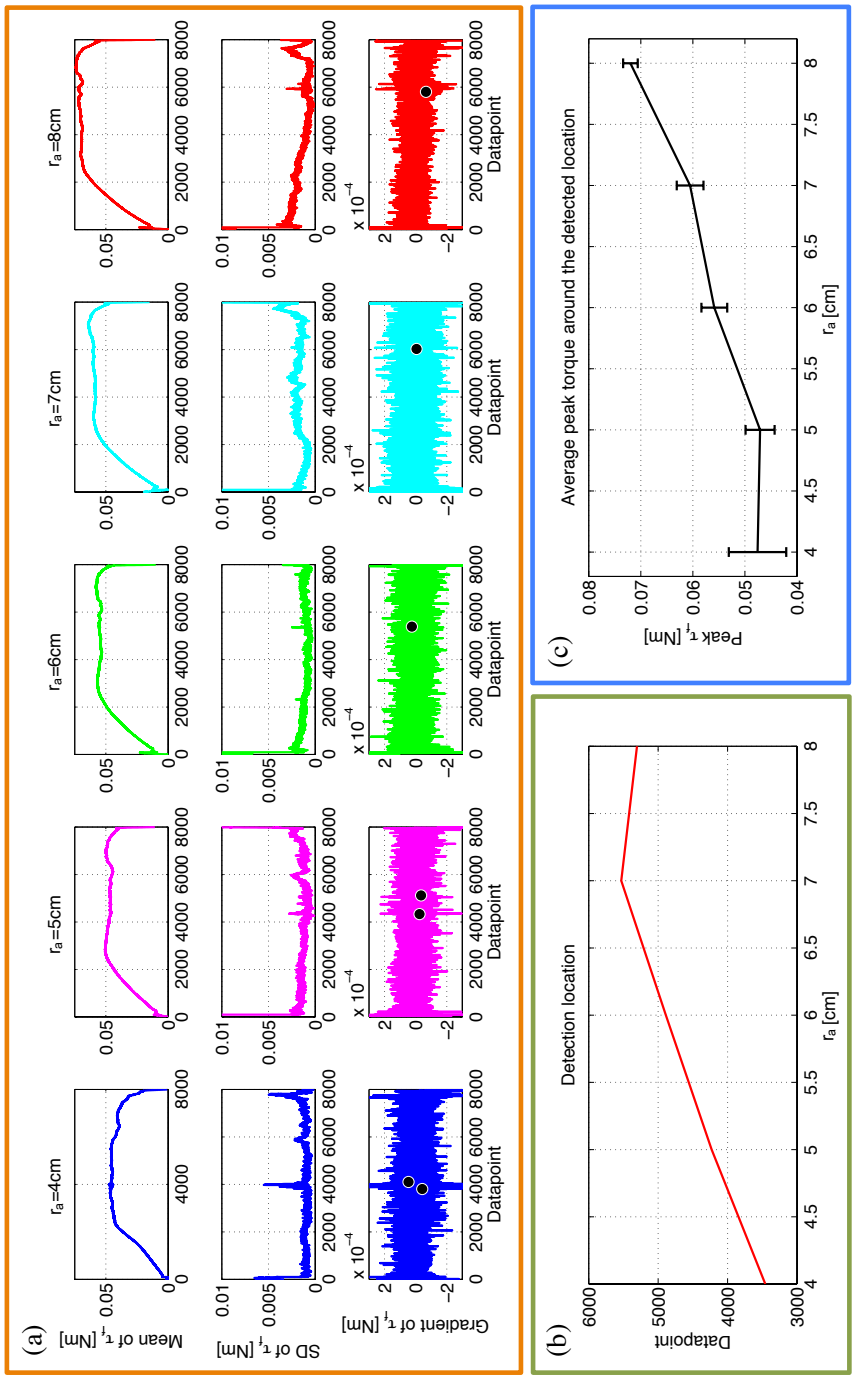

Fig. 5.9 (a) The average of dynamic torque response from the probe during 10 palpation trials over an ex-vivo porcine kidney with an embedded hard nodule given 5 levels of probe's stiffness (in each column). The first row represents the average torque response. The second row illustrates the corresponding standard deviation of the raw torque signals across 10 trials given different levels of stiffness. And the last row shows the decomposed gradient of the average torque response. The detection of the presence of the nodule is indicated by the variance change point in the gradient of the signal, which are shown in black dots. (b) summarizes the average detected location from the last row of Figure 5.9 (a) across stiffness levels. The average torque and corresponding standard deviation extracted at the nodule's detection location across ten trials for different stiffness level.

5.5 Discussion

This chapter discusses how a robot with controllable internal impedance can maximize information gain in proprioception by searching for an optimal stiffness under a nonlinear relationship between the entropy of sensor information and the impedance of the physical embodiment. In order to investigate this, a laboratory made two link planar manipulator with a McKibben type pivot joint (elbow) with controllable stiffness similar to the human arms was used. Then, this chapter poses the problem of using only torque data measured at the fixed base manipulator, to estimate the deflection at the McKibben type elbow caused by an external force at the free end. There was a unimodal nonlinear relationship between the transfer entropy of proprioception under varying stiffness - determined by the pre-tension state r_a - of the McKibben type pivot joint. This chapter calls it a nonlinear internal memory primitive that the robot can use to enhance proprioception.

The experimental evidence provided in this chapter suggests the use of the nonlinear internal memory primitives of the embodiment and kinematic variable to enhance the proprioception. The information gain metrics was used to indicate the optimum internal impedance state (the pre-tension state of the variable stiffness joint) to accurately estimate the internal variable (angular displacement of Mckibben type pivot joint). Two different approaches were used in real-time searching for the optimum pre-tension state of variable stiffness joint, which corresponds to the maximum information gain. The performance of searching algorithms were evaluated based on the average estimation error of the pivot joint angle. It was found that Hooke-Jeeves pattern search, on average, results in lower error. However, it requires higher number of iterations than the alternative Newton-Raphsons approach.

Based on the results shown in this chapter, it can be speculated that biological counterparts may also be using nonlinear memory primitives similar to the one demonstrated in this study to tune embodied proprioception. It would be interesting to study whether embodiment of muscle spindles (position and speed sensing) and tendons (force/torque sensing) could benefit from some real-time internal impedance regulating strategy, and the shapes of the

corresponding memory primitives; and therefore, how the regulations of these behavioral and internal stiffness variable would enhance the efficacy of the information gain in perception during the interaction with external environment. At the end of this chapter, the manipulator was used in the preliminary experiment as a variable stiffness probing device to detect the abnormality inside the ex-vivo porcine kidney. The preliminary results indicate that the torque felt at the base of the probe was subjected to the pre-tension state of the variable stiffness joint. Their relationship and variability hold the non-linear characteristics. In the experiment, this could arise from the dynamic interaction between the soft tissue and the tip of the probe, at which the dynamic torque felt is non-linearly conditioned by the state of internal impedance. This offers the unique opportunity to investigate this relationship in the transfer entropy domain to enhance the estimation of external environment. In the next chapter, this manipulator is used as a probing device to explore the directional information gain in a variable internal impedance probe for soft tissue abnormality identification.

Chapter 6

Information gain in a variable internal impedance probe for soft tissue abnormality identification

Abstract— *This chapter investigates the role of internal impedance of the finger (governing proprioceptive feedback) in the haptic perception information gain. Since, it is not easy to explore the role of stiffness control in biological finger using conventional biological approach, this chapter , instead, investigates this question using a robotic probe with a controllable stiffness Mckibben type joint. This chapter provides the experimental evidence to show that the probe's variable internal impedance can emerge useful dynamic interactions with the soft tissue to gain the information about the interacting soft silicone phantom. The results also suggested that the robotic probe's ability to control its internal impedance is preferred over the rigid one. Therefore these findings provide not only a novel theoretical basis to develop a more efficient biomimetic probe that can self-adapt for maximum information gain in tactile exploration of a soft tissue, but also explained as to why human counterparts regulate their muscle co-contraction state during the haptic exploration.*

6.1 Introduction

The previous chapter discussed the role of internal impedance control for maximising the information gain in embodied perception. The experimental evidences in Chapter 5 have signified that a robotic manipulator with controllable internal impedance can maximise information gain by searching for an optimal stiffness under a non-linear relationship between the entropy of sensory information and the impedance of physical embodiment structure. Furthermore, the results from this work also suggest that the accuracy of estimation of an internal kinematic variable can be enhanced by controlling its internal impedance.

This chapter presents a novel technique to exploit internal impedance control of a soft robotic manipulator described in Section 4.2 of Chapter 4 in soft tissue probing for abnormality identification. Unlike a stiff probe, where the detection of a hard nodule embedded in a soft tissue depends on the applied force and the indentation depth of the probe [163], this novel probe with a controllable joint stiffness mechanism can enhance haptic feedback. The development of this probe can provide the useful insight as to why biological counterparts actively control their internal impedance, like muscle co-contraction state, during the active haptic exploration [18]. The exploitation of such controllable stiffness can be foreseen in various applications, for instance, during minimally invasive surgery (MIS), where surgeon cannot manually palpate the soft tissue before taking a surgical site selection decision. In MIS even if the surgeon has MRI images beforehand, the tissues can move due to posture changes of the patient. Therefore, a final verification of the location has to be made prior to the actual surgery. Since current laparoscopic tools do not provide any haptic feedback, the chapter investigates the possibility of enhancing information gain about the location and depth of a hard nodule in a soft tissue using variable stiffness embodiment such that a force sensor mounted at the handle-end of the tool can detect the abnormality without having to be inserted inside the body. However, it is important to note here that the current design is not miniaturized enough to be tested in-vivo.

The purpose of the experiments presented in this chapter is to investigate how behavioral and environmental parameters can affect the interaction between the probe and a soft silicon

phantom. These parameters include probing velocity, probe's joint stiffness, and depth of nodule embedded in a soft phantom. Given different interaction conditions, this chapter explore how directional information flow can be modulated using information transfer entropy (KL-divergence) to enhance the information gain in the detection of nodules embedded in a soft silicon phantom.

The results from this chapter suggest that in the information metrics domain, the maximum directional information flow was observed during the transition from non-compliant to compliant probe and within the stiffness level of the probe; whereas little information is gained when changing from the compliant to rigid probe. This can be interpreted and used to explain that the ability of varying the internal impedance is necessary to gain perceptual information about the environment in both robotic probe and human counterparts, and that the soft variable stiffness structure is preferred over the rigid one. The results from this chapter indicate that different exploratory strategies, including the regulation of speed and stiffness, can be used in nodule's depth estimation for nodules buried at different levels. It is important to note here that the results obtained in this chapter cannot be generalised that there is an absolute solution to which stiffness level and probing speed velocity are suitable to estimate the properties of different environment. This agrees with the results shown in [41], where surgeons also employ different palpation strategies to locate the nodule in a soft tissue. However, the problem as to how the probe's behavioral variables are controlled during the exploratory process of the environment is beyond the scope of this chapter.

6.2 Experimental setup and methodology

6.2.1 Experimental setup

In this experiment, the manipulator with variable stiffness joint explained in Section 4.2 was used as a probing device similar to the setup shown in the preliminary experiment in Section 5.4. The probe platform is mounted on the ANT130 two-axis linear stage (Aerotech Inc., resolution of 1nm) installed up side down as shown in Figure 6.1. ATI Mini40 6-axis force/torque transducer (SI-20-1 from ATI Industrial Automation, resolution around z-axis:

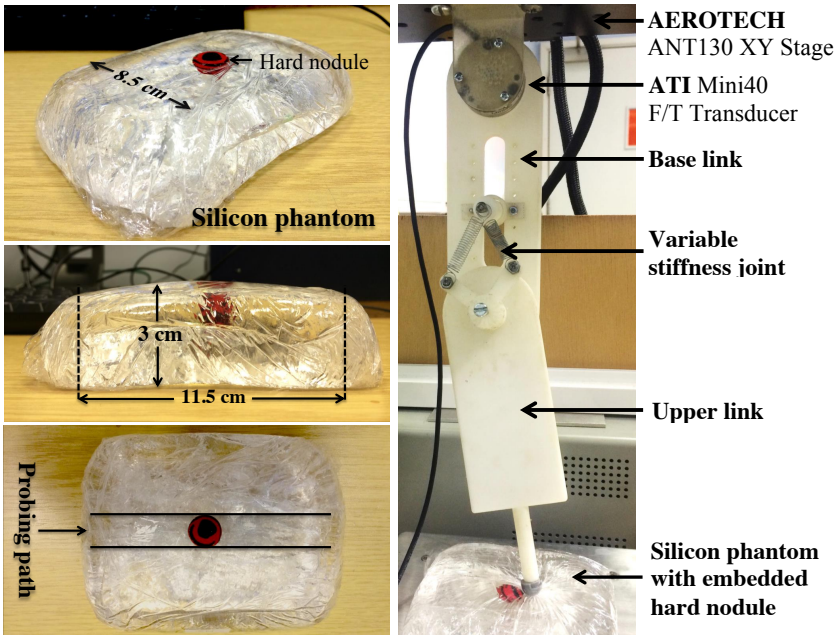

(a) (b)

Fig. 6.1 (a) A soft silicon phantom fabricated using soft clear silicon elastomer gel replicating a soft tissue with a spherical plastic bead of size 15 mm diameter embedded inside at different depths. (b) A photo of an experimental setup, where the manipulator is attached under the ANT130 XY stage from AEROTECH, US. The torque experienced at the base of the manipulator during the interaction with soft silicone phantom with embedded hard nodule, is measured by ATI Mini40 six axis force/torque transducer.

$1.25e^{-4}$ Nm) is mounted at the base of the probe capturing torque data during palpation at frequency of 1000 Hz. The identical set of soft silicon phantoms to those presented in Section 3.2.1 were used to replicate the soft tissue as the physical properties of the fresh animal's organs can change over a period of time. Silicon phantoms were made from a soft clear silicon elastomer gel RTV27905 from Techsil. The process of fabricating the phantom is identical to that described in Section 3.2.1. In this experiment, three silicon phantoms were used as samples, in which the nodules were embedded at the depth of 2, 4, and 8 mm from the exposed surface of the phantom to the top of the nodule.

6.2.2 Methodology

The purpose of this experiment is to examine and compare the influences of a non-compliant probe and a probe with controllable stiffness on the detection of a nodule buried in a soft

phantom at different depth. The influence was computed based on the directional information transfer obtained from measured torque during the interaction together with the knowledge of past experience in form of memory primitives. In the experiments, the effects of both compliant and non-compliant (in this chapter, this is referred to as "locked" joint.) probe during the "idle" and dynamic interaction with a soft silicon phantom were investigated. As for the compliant probe, the configuration stiffness of the joint, $\boldsymbol{\xi}$, was constrained to one variable, r_a (pre-tensional state), by fixing the opening angle of both lever arms to $\alpha = 55°$. In order to examine the effect of varying joint stiffness, i.e. varying r_a, (see Figure 6.1 (b)) on the perception during palpation, torque τ_f was measured at the base of the manipulator around z-axis of the transducer.

During the experiment, two different scenarios were examined, 1) "idle", and 2) dynamics. For the "idle" case ($v_{probe} = 0$), the probe was paused on top of the nodule location to allow the acquisition of torque signal. On the other hand, during the dynamic cases the probe was programmed to slide along a sample phantom, i.e. the blue path in Figure 6.1 (a), at different constant speeds of, v_{probe} =10, 20, and 30 mm/s, at which a nodule is embedded. The torque data was recorded across 50 trials for different joint stiffness levels (r_a = 4 cm, 5 cm, 6 cm, and a "locked" case), and different levels of probe sweeping velocity (PSV), v_{probe}, during the interaction with soft phantoms with nodule embedded at different depths. This resulted in a total of 48 unique interaction conditions between the phantom and the probe. The torque measurement and the control of the XY-stage movement was carried out by a program written in LabView 2012 application, National Instrument. Corp. through a data acquisition card PCIe-6320 (National Instrument. Corp.) and the Ensemble MP motion controller (Aerotech Inc.) respectively. The experimental conditions are shown in table 6.1.

Table 6.1 Experimental conditions

Nodule's depth d **[mm]**	**Stiffness** r_a **[cm]**	**probing speed** v_{probe} **[mm/s]**
2	{4, 5, 6, locked}	{10, 20, 30, "idle"}
4	{4, 5, 6, locked}	{10, 20, 30, "idle"}
8	{4, 5, 6, locked}	{10, 20, 30, "idle"}

6.3 Results

The average recorded torque information including the variability across 50 trials during the interaction between the probe and the area of the silicon phantom's surface, beneath which the nodule is embedded are shown in Figure 6.2 for the dynamic cases ($v_{probe} > 0$ mm/s) as well as the "idle" case. The recorded data was used to construct a set of probabilistic memory primitives given different internal impedance levels and environmental variables. These memory primitives represent the palpation experience of the probe and can be used in the information gain metrics in order to detect the presence of a hard nodule.

The measured torque information during the experiment was processed in MATLAB R2013b, The Mathworks, Inc. Firstly, all measured signals were filtered to remove the noise and to discriminate the torque sensed during the interaction at the location of hard nodule from that of normal soft silicone phantom. In this case, the discrete wavelet transform (DWT) method with Daubechie's mother wavelet (db10) was used to filter the raw torque signal, because the torque sensed as the probe swept over the nodule was subjected to the sudden changes. This is because of that DWT with Daubechie's mother wavelet is appropriate to detect sudden discontinuities in the signal under the time domain, in comparison with other signal filtering techniques [164]. The decomposition of the signal was carried out for 5 levels, as this returned the highest percentage energy of the decomposed signal (approximation).

In the "idle" case ($v_{probe} = 0$), settled torque information was obtained from each trial of decomposed torque signal perceived during interaction with soft silicone phantom with nodule embedded at different depth levels. The signals were averaged given different probe stiffness and nodule's depth levels. In the dynamic cases ($v_{probe} > 0$), for each torque signal perceived in each trial, the maximum torque was extracted at the exact location where the probe's tip swept on top of the nodule during interaction at different PSV and probe's stiffness levels.

The fitted distribution of the corresponding torque information across 50 trials given different experimental conditions are shown in Figure 6.2 (a). From these distributions, the mean and standard deviation of torque response, τ_f, can be summarized for different r_a, and v_{probe} as shown in Figure 6.2 (b), and (c). Figure 6.2 (b) illustrates that the average

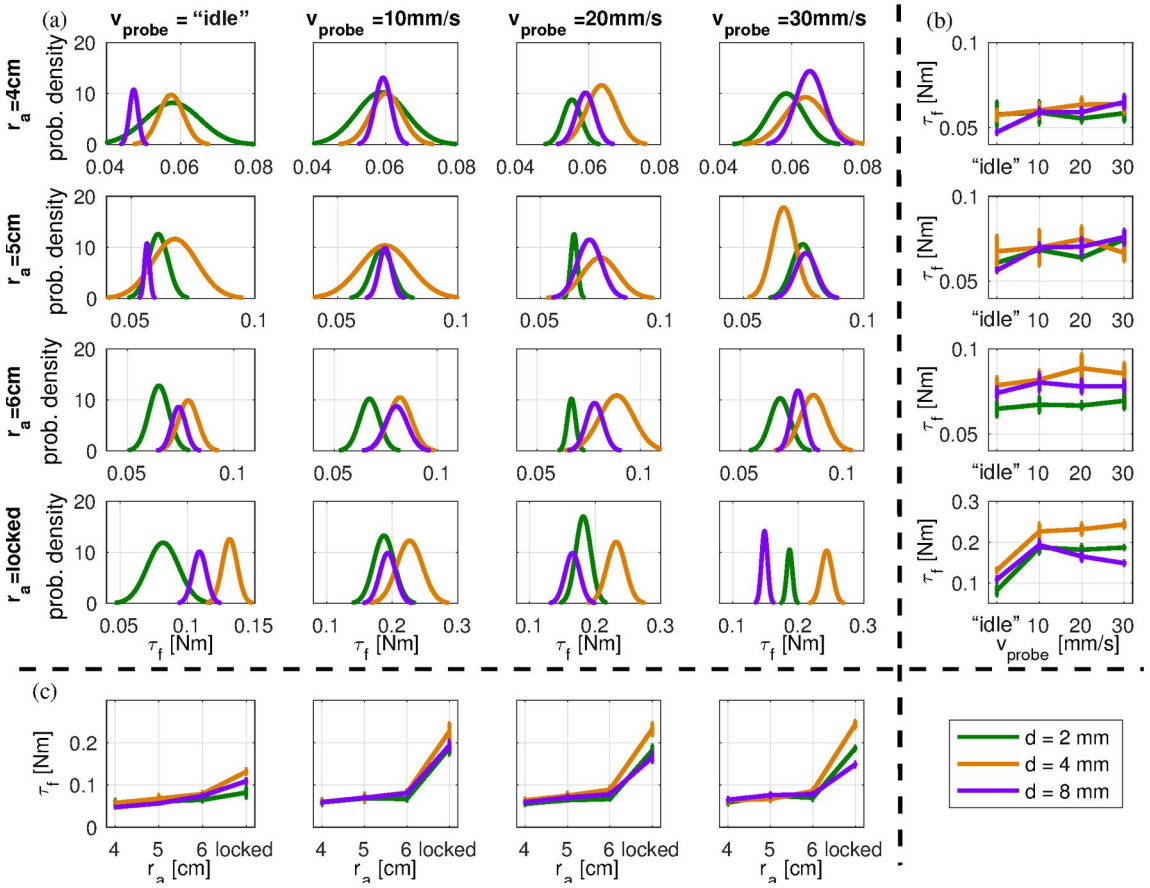

Fig. 6.2 (a) Fitted normal distribution for 50 trials of the torque measured at nodule location during palpation trials over silicone phantom with a nodule embedded at 2mm (green), 4mm (orange), and 8mm (purple), for different probing speeds (including "idle"), v_{probe} = "idle", 10, 20, and 30 mm/s, and different stiffness levels of compliant probe (including non-compliant probe), r_a = 4 cm, 5 cm, 6 cm, and 'locked'. Mean and standard deviation of τ_f for v_{probe} (x-axis) from each row in (a) are shown in (b) for different r_a. Mean and standard deviation of τ_f for r_a (x-axis) from each column in (a) are shown in (c) for different v_{probe}.

torque profiles for different depths of the nodule become less sensitive to the PSV level for the probe's stiffness of $r_a = 6$ cm. The analysis of variance (ANOVA) test was performed on the measured torque given different stiffness level, r_a, probe sweeping velocity, v_{probe}, and the depth of the nodule, d. The results from the test suggested that when $r_a < 6$ cm, the torque profiles are not statistically significantly different ($p < 0.05$) across various probing speed. However, when the probe is stiff, the torque profile becomes more sensitive to the probing speed. This could potentially lead to the illusive perceptions of the nodule's depth

at certain probing speeds. Figure 6.2 (c) shows this nonlinear sensitivity of torque to probing speeds, when the compliant joint of the probe is locked to make a stiff probe.

The main focus of this chapter was to investigate as to how the directional information flow is influenced by the variation in the compliancy of the probe and how these information could be used to predict or estimate the state of the environment. The information transfer entropy under Kullback-Liebler divergence was used as the indication of the directional information flow in different stiffness level transitions. Therefore, it was necessary to construct a set of memory primitives that can be used during the interaction with unknown phantom to allow the computation of information gain during the stiffness level transitions.

From 50 trials of torque information for each interaction condition, 30 trials were randomly sampled for memory primitives construction; while 20 trials were used as the test set to assess the influence of the probe's stiffness transition on the information gain. The examples of memory primitive landscapes are presented in Figure 6.3. Note that since the memory primitives are constructed based on the probability from randomly selected trials, the shape of the primitives may change according to the information obtained from selected learning.

6.3.1 Kullback Liebler divergence information gain metrics

Information transfer entropy or also known as relative entropy can be used to observe the directed information exchanges between two systems/variables, which quantifies the common influences of two coupled systems/factors [159]. In other words, mutual information between probe stiffness (random variable A (RV-A)) and torque sensor reading (random variable B (RV-B)) doesn't change with the exchange of variables, whereas, the transfer entropy from RV-A to RV-B is different from the transfer entropy from RV-B to RV-A. Kullback-Liebler (KL) divergence quantifies this transfer entropy.

The influence of changing the interaction conditions (probe's stiffness) on the measured torque was investigated based on information gain using Kullback Liebler (KL) transfer entropy. This approach can be used to examine the influence of changing probe stiffness (including the compliancy) during palpation.

The information gain function is

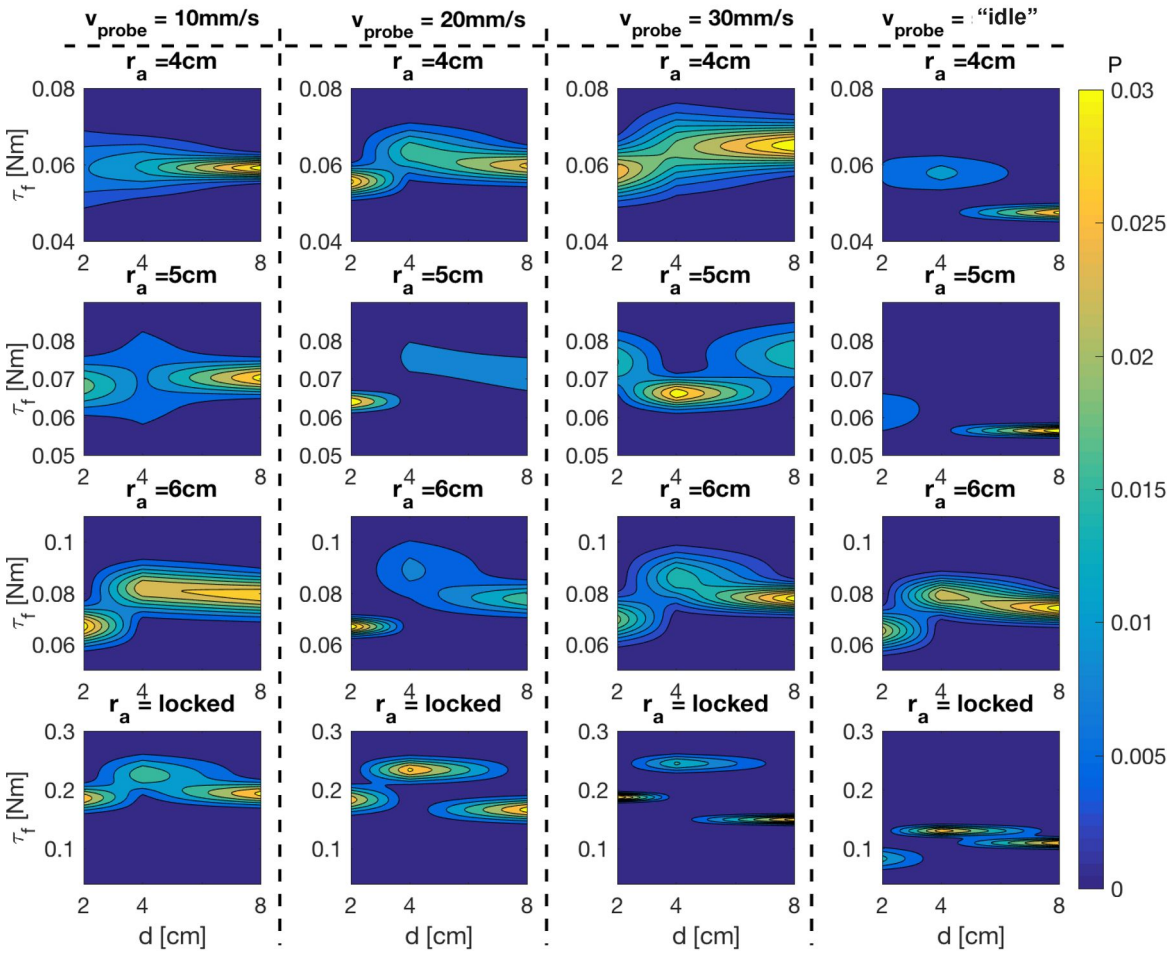

Fig. 6.3 Memory Primitives constructed from 30 randomly selected trials of wavelet decomposed base torque as a function of probe stiffness levels during palpation at different speeds on silicon phantoms with nodules embedded at $d = 2$ mm, 4 mm, and 8 mm, where each row represents the probe's stiffness level, r_a and each column represents the probe sweeping velocity, v_{probe}.

$$G = \sum_{m=1}^{M} P(d|\tau_f, r_a, v_{probe}) \log \frac{P(d|\tau_f, r_a, v_{probe})}{P(d|\tau_f^{ini}, r_a^{ini}, v_{probe})}, \tag{6.1}$$

where G is the measure of information gain from M datapoints, $P(d|\tau_f, r_a, v_{probe})$ is the probability of d given τ_f, r_a, and v_{probe}. τ_f is the measured torque value from the sensor during interaction with the phantom under different probe's stiffness, r_a and r_a^{ini}.

Using KL-divergence approach, different interaction conditions (probe's stiffness level) were compared with different initial stiffness levels to find the directional information gain

in each stiffness state transition, which in this case can be used to inform the exploratory process about the useful control behavior of the internal impedance. If τ_f is considered as a variable measured during interaction with an unknown soft silicone phantom (with embedded hard nodule), its entropy for a given depth of the nodule, d, is dependent on the state of probe's stiffness level r_a. Therefore, the Kullback Liebler (KL) transfer entropy defined in equation (6.1), which information gained, G, about the environment d, given the measured torque signal, τ_f, which is conditioned by the variation in probe's stiffness level r_a, is a good indicator to determine the criteria in the exploratory process and to search for the directional information flow given different stiffness level transition [159].

6.3.2 Influence of internal impedance control for hard nodule detection under information gain metrics

Algorithm 6.1 illustrates the process employed in this chapter to investigate the directional information gain during the transition of probe's stiffness level.

Algorithm 6.1: Directional information gain computation algorithm

```
function DirectionalInfoGainComputation (τ_{f,t∈[1:50]}(r_a, v_probe, d));
Input  : τ_{f,t∈[1:50]}(r_a, v_probe, d)
Output : Directional information gain
for each trial t ∈ [1 : 50] do
    Randomly select 30 trials of collected data to create memory primitives, φ;
    The rest 20 trials selected for test set, T;
    for each r_a, v_probe, and d do
        Create memory primitives shown in Figure 6.3;
    for each τ_f in T(v_probe, d, r_a^ini) do
        Compute P(d|τ_f, r_a^ini, v_probe) from φ.;
        for each τ_f in T(v_probe, d, r_a) do
            Compute P(d|τ_f, r_a, v_probe) from φ.;
            Compute G from Equation 6.1.;
Compute average G for all d, r_a^ini − r_a pair, and v_probe;
```

In order to obtain the average information gain, the process was repeated for 50 trials from the construction of memory primitives to the nodule's depth estimation stage for each of the three levels of known depth, i.e. 2, 4, and 8 mm from the rest 20 trials of measured

torque during palpation by the probe of different stiffness levels (including non-compliant one) at different speed (v_{probe} = 10, 20, 30 mm/s, and "idle"). Figure 6.4 shows the average directional information gain responses for each probe stiffness transition for various palpation speeds and different levels of nodule's depth.

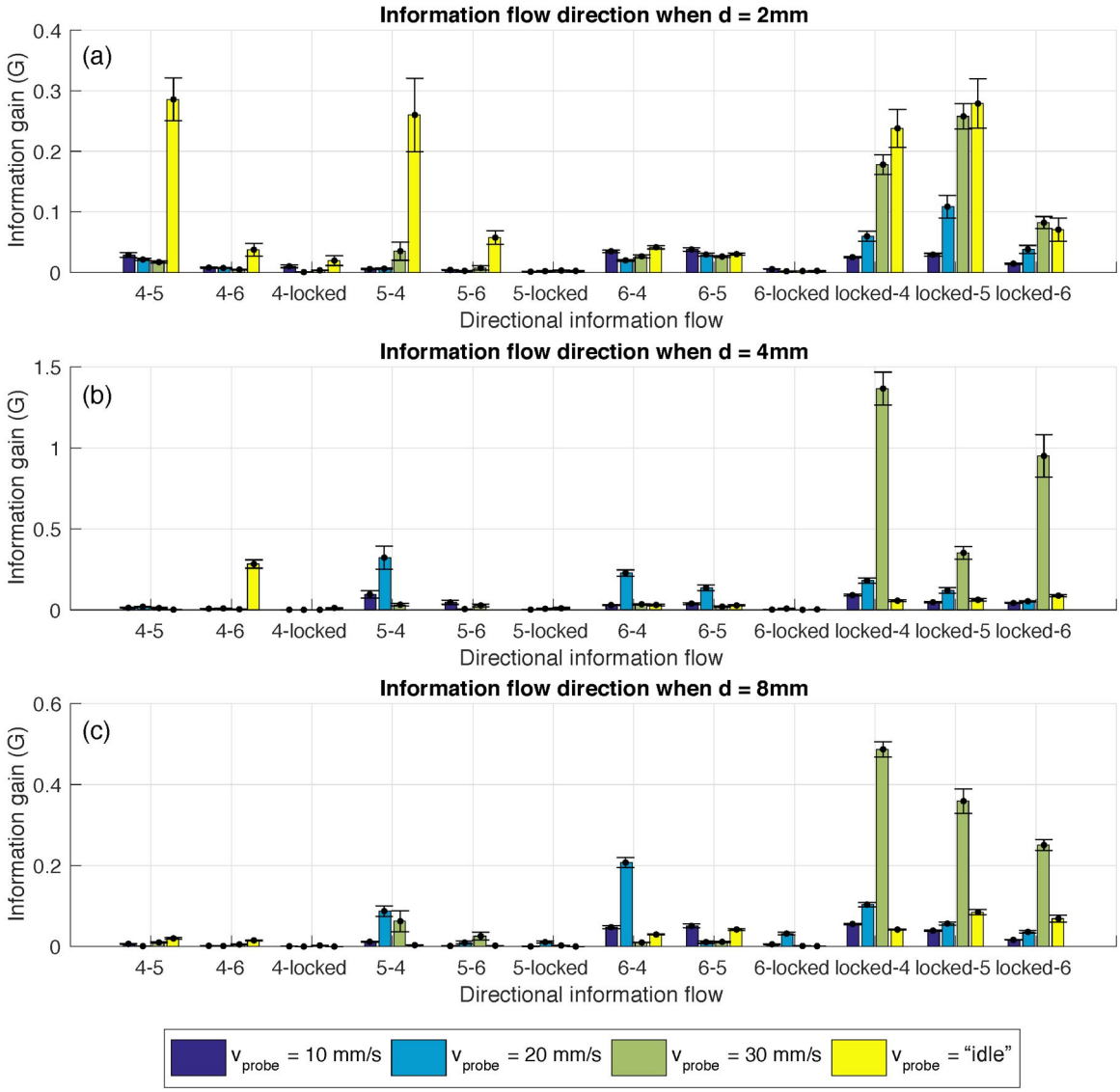

Fig. 6.4 Average information gain responses and corresponding standard error for different probe stiffness transitions for various palpation speeds (including "idle") and different level of nodule's depth, 2 mm (a), 4 mm (b), and 8 mm (c), where 'locked' represents the case when the joint is locked (non-compliant)

As can be seen in Figure 6.4, there are little to none additional information gained for the stiffness transfer from any compliant level to non-compliant. However, the additional information gain increases during the stiffness transfer among different stiffness levels and from non-compliant to compliant. This signifies that by moving or changing from non-compliant to compliant probe, more information about the environmental variable can be gained.

In general, this indication is very useful in determining whether or not a system or a process should carry on exploring the environment. From this particular case, it is clearly seen that by transfer the compliancy state of the probe from any compliant level to non-compliant state, little to none information is gained. This could be implied that there is no need for a probe to further explore the environment under the non-compliant state as no new information can be gained. On the other hand, the maximum information is gained by moving from the non-compliant to compliant state of the probe. This means that new information can be gained by moving from rigid state to compliant state. This chapter has provided the experimental evidence outlining the necessity of the controllable stiffness body during the exploration of the environment. The experimental evidence provided in this chapter could also help explain the reason as to why the actuation (changing muscle co-contraction state) is essential during exploration of the environment.

6.4 Discussion

This chapter investigates the influence of internal impedance control on the embodied perceptual information gain in tactile exploration of a soft tissue. A laboratory made two link planar manipulator with a McKibben type pivot joint controllable stiffness was used as a robotic probe. The experimental evidence suggested that the information gain responses depend on the influence from each behavioral and environmental variables and also the interactions among them.

In this chapter, the effect of probe's stiffness transition on information gain in KL-divergence was explored, which can be used for directing the behavior of the probe in exploratory process to estimate the depth of an embedded nodule in a soft silicone phantom

during palpation. 30 randomly selected trials from torque responses for each interaction condition are used to construct memory primitives; whereas the rest 20 trials are used as test conditions. Depending on the interaction conditions, the directional information transfer can be used as a guideline in the probe's stiffness modulation strategy (initial r_a, and final r_a) to gain the information about the environment. In order to deliver the average results, depth estimation process were repeated for 50 trials, in which new learning and test set were randomly selected for each trial, across different interaction conditions. In general, the average additional information gain is relatively higher for transitions from non-compliant to compliant and among compliant levels in comparison to those from compliant to non-compliant. This means that the exploratory process is more likely to gain information regarding the depth of the nodule by switching from non-compliant probe to compliant one.

From the experimental results, it is fair to conclude that both detection of a nodule and nodule's depth estimation depend on the interaction among all behavioral conditions of the probe, including the probe stiffness, palpation speed, and the environmental variables such as the stiffness distribution of nodule. It was also shown in [41] in surgeon's manual palpation, that there is variability in behavioral strategies and characteristics employed to locate hard nodule in a soft tissue. Therefore, this chapter highlights that a controllable stiffness robotic probe can offer flexibility to use a wider range of strategies, similar to what surgeons use during manual palpation to maximize the gain of palpation information by searching in the stiffness and probing speed space. However, development of such an autonomous strategy is beyond the scope of this chapter.

This chapter provides important guidelines to design a variable stiffness probe and construction of internal memory primitives to estimate information gain of changing the internal stiffness. Furthermore, these findings also contribute to our understanding in the role of embodiment in perception, which acts as a mediator between perception and action. The next chapter explores the possibility in implementing an autonomous real-time algorithm that can efficiently tune the stiffness and palpation speed of the probe by monitoring the information gain.

Chapter 7

Active Bayesian haptic perception of robotic probe

Abstract— *The previous chapter has discussed the effect of the internal impedance variation on haptic perception information gain in the task of identifying the abnormality in a soft tissue. It was shown that information regarding the presence of a hard nodule in soft silicone phantom can be enhanced through the regulation of the probe's joint stiffness. By tuning the behavioral variables of the probe, such as the joint's stiffness, the information gained regarding the environment can be maximised. This raises the question as to how these variables (probe's stiffness, indentation, and PSV) should be tuned or controlled given different environments during haptic exploration. Furthermore, the experimental results in Chapter 3 indicate that humans also regulate the stiffness of the MCP finger joint during haptic exploration to estimate the depth of a nodule embedded in a soft silicone phantom. The pattern from such muscle co-contraction regulation was extracted and presented in the form of a Markov decision matrix. This chapter uses the same haptic exploration case of estimating the depth of a nodule embedded in a soft silicone phantom as a case study to explore whether the robotic probe could exploit the similar human's stiffness control pattern to enhance the estimation. The soft robotic experiments showed that haptic information gain and hence the accuracy of estimating the depth of the hard nodule can be maximized by varying the internal stiffness of the soft probe.*

7.1 Introduction

This chapter used the task of estimating the depth of a hard nodule buried inside a soft object, i.e. soft silicone phantom, carried out by a robotic finger with variable stiffness and behavioral control to investigate their individual and integrative roles in the efficacy of information gain in active haptic perception. It was shown in a previous study [165] that an artificial tactile sensor can outperform the human's capability in the passive detection of a lump embedded inside a soft phantom. In the study, haptic perception of human was limited to that from the passive tactile sensation perceived through mechanoreceptors at the finger distal phalanges. However, human's active touch behavior was not considered in the study. It was shown in [103] that by controlling the exploration speed, orientation, and voluntary movement, the performance of the perception can be enhanced during the active touch. The experimental results presented in this Chapter 3 also suggest that apart from the voluntary movement of the finger, the voluntary muscle co-contraction also shows variability during manual palpation. Therefore it can be suspected that the regulation of finger's internal impedance plays an important role in human's proprioceptive information during active exploration.

This chapter investigates the role of internal impedance in proprioception using a soft robotic probe with a controllable stiffness Mckibben type joint to probe the soft silicone phantom. While Chapter 6 has confirmed the necessity for the soft robotic probe to attain its ability to control the stiffness rating of the body (joint's stiffness) in order to gain the information during the exploration of the environment; the results did not suggest the optimum levels of probe's stiffness to achieve the maximum estimation accuracy during the exploration of the environment. It was the transfer of joint's stiffness level strategy based on the directional information transfer that plays an important role in enhancing the information gained about the environment. The information gain during the transfer of joint's stiffness could potentially be used to help in determining the appropriate probe's stiffness modulation strategy during an automated active exploration.

The soft robotic probe used in this study represents an abstracted version of the human finger with automated joint's stiffness and behavioral (Probing sweeping velocity (PSV) and indentation) control mechanisms. The soft robotic probe comprises of a controllable stiffness joint and a force sensor at the base, so that the proprioceptive information at the force sensor is conditioned by the level of joint's stiffness and behavioral variables similar to how the biological finger's proprioceptive sensation functions. In the first part of experiments presented in this chapter (Experiment 1), the influence of variable internal stiffness on the efficacy in haptic perception was investigated. The stiffness of the soft robotic probe was controlled across trials according to the co-contraction strategy employed by human subjects. The human's co-contraction strategy was abstracted in the form of a Markov decision process from the electromyography (EMG) signals recorded from the human subjects presented in Chapter 3.

Furthermore, when people were asked to palpate a novel soft object to discern its physical properties such as texture, elasticity, and even non-homogeneity, they not only regulated co-contraction level of antagonistic muscles to control the mechanical impedance of fingers, but also the probing behavior, such as indentation and palpation velocity. It is suspected that such behavior tries to enhance haptic perception by regulating the function of mechanoreceptors at different depths of the fingertips and proprioceptive sensors such as tendon and spindle sensors located in muscles. Therefore, the second part of the experiment (Experiment 2) involved the regulation of the indentation level and probe sweeping velocity in addition to the internal stiffness. This experiment addresses the question as to whether a robotic probe with variable impedance, indentation, and probe sweeping velocity (PSV) can achieve a better estimation accuracy of a given environmental condition (i.e. depth of a nodule embedded inside a silicon phantom).

From the experimental results, it was found that: 1) The controllable stiffness soft robotic probe improved its accuracy of estimating the depth of a hard nodule in the same soft phantom by implementing the human's muscle co-contraction strategy obtained in Chapter 3, 2) The internal stiffness of the soft probe plays a statistically significant role in the accuracy of nodule's depth estimation, 3) A Bayesian learning framework combining the regulation of

internal stiffness, indentation level, and PSV can maximize the information gain and enhance the estimation accuracy, and 4) Experimental results to show that proposed algorithm can achieve on average 99% and 96% accuracy in estimating the nodule's depth in both active and passive perception respectively, when the nodule depth is one out of 3 known levels. The results were in line with the speculation in previous work [20], where a robotic manipulator can use transfer entropy to maximize sensory information gain of its own states by regulating the internal stiffness.

7.2 Experimental setup

The first objective of this chapter is to derive deeper insights into the human's muscle co-contraction strategy during manual palpation to estimate the depth of the hard nodule. In this study, a variable stiffness probe as an abstracted version of the human finger was used to isolate and study the effect of joint stiffness control on the tendon force/torque sensor located at the base shown in Figure 7.1 (a) as opposed to force measurement at the tip of the finger. Secondly, this chapter also investigates the influence of the variation of combinations of probe's internal stiffness, indentation level, and PSV, on real-time estimation of the depth of the hard nodule. The experiments described in this chapter exploited the variable behavioral probe explained in Chapter 4.3 and the identical set of soft silicone phantoms with the nodule embedded at three different depth levels, $d = 2$, 4, and 8 mm described in Chapter 3.2.

In the first experiment, the connecting link of the probe was kept constant at $l_o = 143$ mm. The total length of this probe when the angle of pivot joint, $q = 0$, was 293 mm. The distance between the surface of the soft silicone phantom and the XY plate is 290 mm. This resulted in the constant indentation, $i = 3$ mm. The complete course of probe's movement in each palpation trial is shown in Figure 7.1 (c), where the speed of the probe sweeping movement is kept at v_{probe} 20 mm/s. The only controlled parameter in the first experiment was the stiffness rating of the probe. The stiffness rating of the joint, K_s, can be expressed as

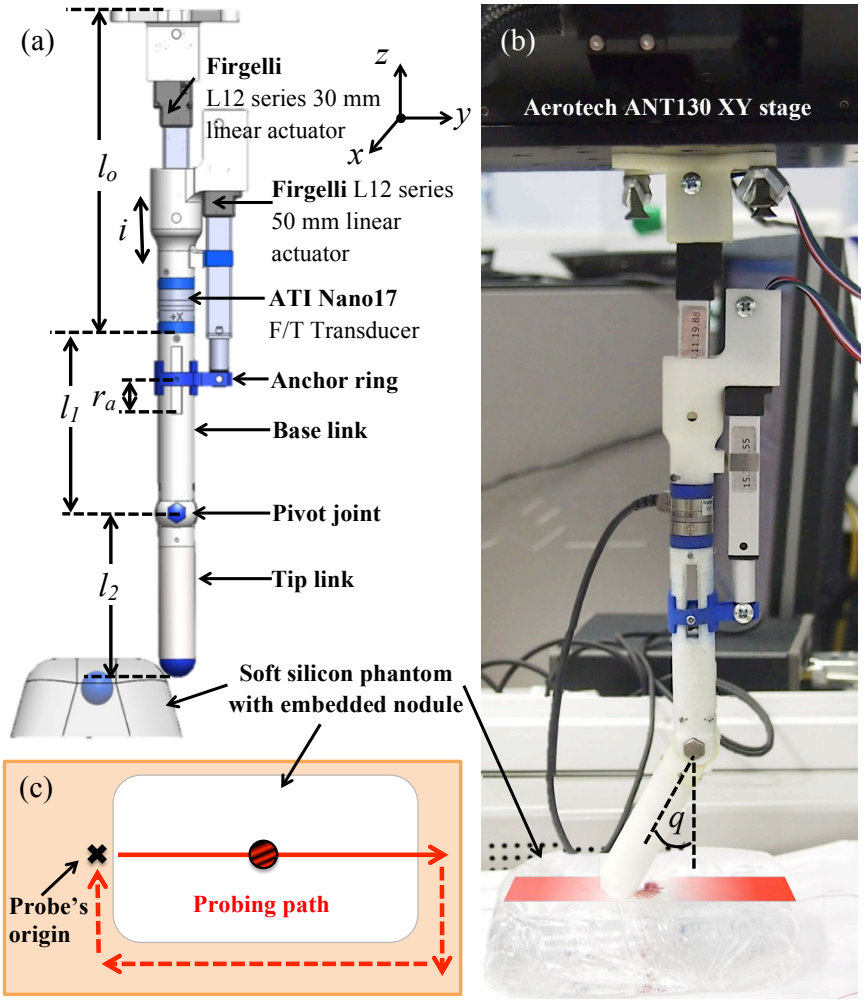

Fig. 7.1 (a) Probe's design. It comprises of a Firgelli L12 linear actuator to control the stiffness of the probe. ATI Nano17 F/T transducer is mounted at the top-end of the base link to measure the torque during the interaction with soft silicone phantom, (b) Photo of the complete experimental platform's design comprising of the variable stiffness probe mounted on XY-stage during palpation to estimate the depth of an embedded nodule. The red translucent path graphically imposed in the photo indicates the probing path in the experiment.

a function of rotational displacement, q, and the position of the anchor ring, r_a, as following:

$$K_s = 2r_a R k_s \cos(q), \tag{7.1}$$

where $R = 6.8$ mm is the radius of the pivot joint at which the microfilament is attached to. The analytical stiffness of the joint undergoing changes in the angular displacement, q, and the position of the anchor ring, r_a, is shown in Figure 7.2 (b). The relationship between the stiffness rating, K_s, and the angular displacement of the joint, q, was governed by the position of the anchor ring. This relationship became more linear within the probe's angular deflection space as the anchor ring approaches its origin at $r_a = 0$ mm. By changing the position of the anchor ring, the relationship between q and the angle-dependent stiffness rating of the joint can be controlled. Therefore, the joint stiffness rating of the probe was solely determined by the position of the anchor ring, r_a.

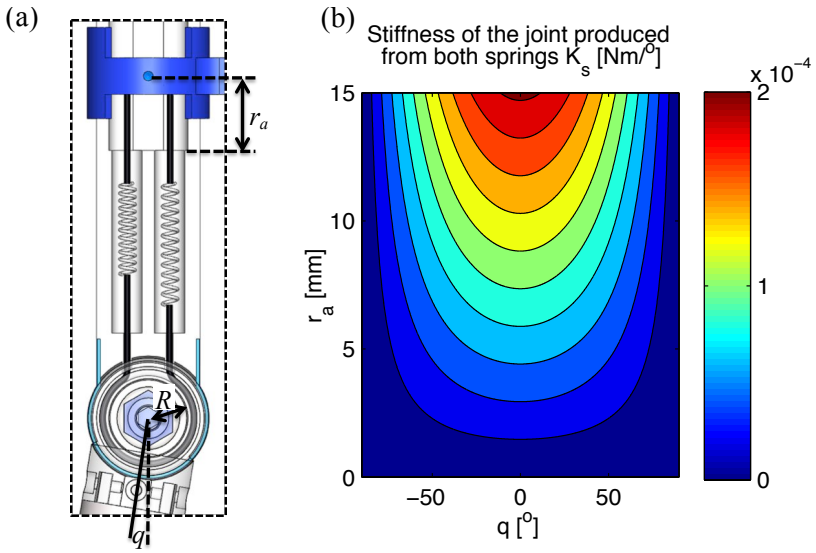

Fig. 7.2 (a) The exploded view of the Mckibben type joint mechanism with two springs located inside the base link. Both springs are attached to the common point at the middle of the pivot joint through a microfilament thread. The other ends of both springs were attached to the anchor ring. The displacement of the anchor ring from the resting position, r_a, was used to control the stiffness of the joint. (b) The analytical stiffness rating of the joint as the angular displacement of the pivot changes between -90° and 90° across the variation of the anchor ring's position.

In the second part of the experiments, the indentation level and the probe sweeping velocity (PSV), were also allowed to vary, in addition to the variation of internal stiffness of the probe. The indentation level can be controlled by controlling the linear actuator at the connecting link, l_o. The PSV can be controlled by the built-in controller of the XY-stage. The experimental conditions in the second part of the experiment can be found in Table 7.1.

Table 7.1 Experimental Conditions

Experimental variables	**Sym.**	**Values (Exp. 1)**	**Values (Exp. 2)**	**Units**
Probe's stiffness (anchor position)	r_a	{0,4,8,12,16}	{0,4,8,12,16}	mm
Relative distance between the tip of the probe at rest and the surface of phantom, i.e. inwards the phantom (indentation)	i	3	{3,5,7,9,11}	mm
Probe's velocity	v_{probe}	20	{10,20,30}	mm/s
Nodule's depth	d	{2,4,8}	{2,4,8}	mm
Distance between the XY plate and surface of soft silicone phantom	l_t	290	290	mm

In both experiments, in each probing trial, the probe was programmed to probe along the sample in a sweeping motion in the mono direction of red solid arrow line (shown in Figure 7.1 (c)) along the red path (shown in Figure 7.1 (b)). The position of the probe was controlled by the XY-stage. At the end of each trial, XY-stage was programmed to move the probe back to its origin position ("X" in Figure 7.1 (c)) through the red dotted path. The torque, τ_f , generated due to the interaction with soft tissue was measured at the rate of 1000 Hz around the F/T transducer's x-axis, which was parallel to the axis of the probe's pivot joint. The data acquisition only took place when the probe was palpating over the soft silicone phantom (red solid line in Figure 7.1 (c)). The measurement of τ_f and the control of r_a, i, and v_{probe} were carried out via a program written in LabView2012 application, National Instrument, Corp., through data acquisition cards PCIe-6320 and NI-USB6341, respectively.

Since human subjects spent some time regulating the level of muscle co-contraction and behavior during manual palpation, this chapter posed the hypotheses that stiffness and beahvioral variables regulation can exploit prior experience of proprioceptive sensors in known environments. Here, these hypotheses were tested using a laboratory made robotic probe that can regulate the internal stiffness, indentation level, and PSV, to improve the accuracy of estimating an environmental variable (the depth of a buried nodule in a soft phantom in this case), by exploiting memory primitives constructed in multiple internal stiffness levels (for first part of the experiment) and in multiple combinations of internal stiffness,

indentation, and PSV levels (for second part of the experiment) to maximize information gain in a Bayesian inferencing framework.

7.3 Methodology

7.3.1 Construction of probe's memory primitives

Similar to the human experiment described earlier in this thesis in Chapter 3, the robotic probe experiments were also divided into two parts. Firstly, the probe was allowed to explore the environment under different behavioral conditions for 25 trials. In this instance, the probing experience during the interaction with soft phantoms with nodules embedded at different depths is presented as 'memory primitives' in the form of a probability distribution of the measured quantity, τ_f, as a function of probe's internal stiffness, r_a, indentation level, i, and PSV, v_{probe} and the environmental parameter, i.e. the depth of nodule, d, over multiple learning trials. The recorded τ_f from each trial was post-processed in MATLAB R2013b application, MathWorks, Inc. to create the memory primitives.

Each measured torque signal recorded from the F/T transducer was first de-noised. The purpose of filtering the raw measured torque signal obtained from the sensor was to remove the noise as well as to discriminate the torque sensed during the interaction at the location of hard nodule from that of normal soft silicone phantom, which was subjected to the sudden changes in the torque signal. Therefore, discrete wavelet transform (DWT) with Daubechie's mother wavelet, $db10$, was used to decompose the raw torque signal for 5 decomposition levels. This was because, in comparison with other technique like fast Fourier Transform (FFT), DWT Daubechies is more appropriate to detect sudden discontinuities in the signal under the time domain [164]. From each de-noised torque signal, the peak torque at the nodule's location was extracted. Figure 7.3 shows an example of a of processed torque signal with shaded error bars representing standard deviation across different probe's stiffness levels r_a, given $i = 3$ mm and $v_{probe} = 20$ mm/s, from 25 trials during the interaction with phantom with nodule embedded at 8 mm. The peak torque was extracted from the processed torque signal around the location at which the probe went over the nodule (shown as 'o' in the

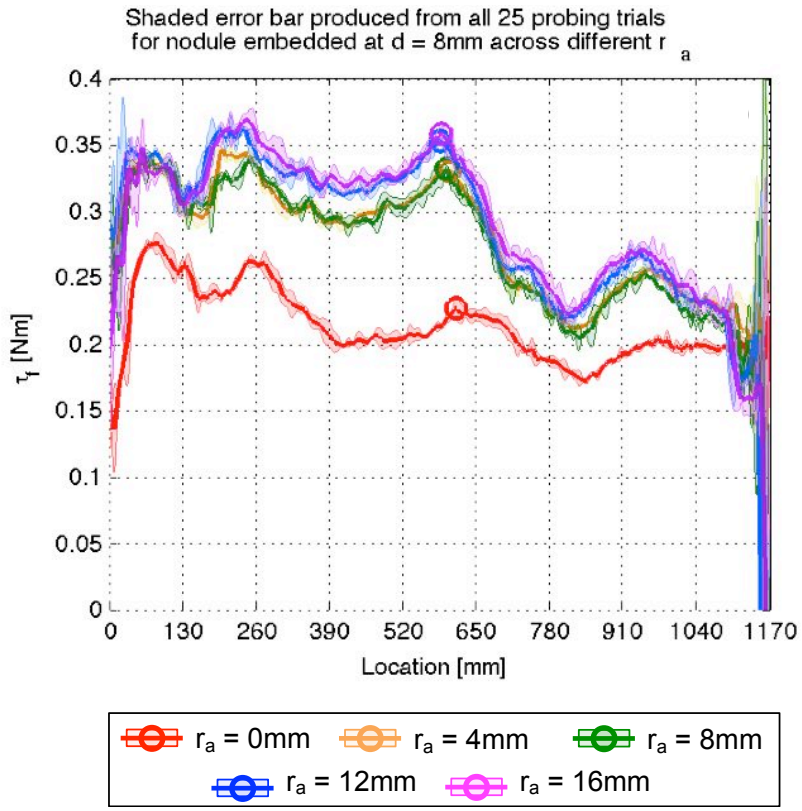

Fig. 7.3 The mean and shaded error bar across 25 trials of processed torque signal perceived during the interaction with soft silicon phantom with nodule embedded at $d = 8$ mm across different probe's stiffness levels, r_a, when $i = 3$ mm and $v_{probe} = 20$ mm/s. The peak torque at the nodule location is captured by taking the maximum around the area at which the nodule is embedded (shown in 'o').

Figure 7.3). The probability distribution of torque, $P(\tau_f|d, r_a, i, v_{probe})$, can be generated by fitting a normal distribution to the extracted peak torque data captured from all 25 trials given a unique combination of different nodule's depth, d, probe's stiffness, r_a, indentation level, i, and PSV, v_{probe}.

For Experiment 1, the memory primitives of peak torque were constructed across 5 levels of stiffness rating, r_a, during the interaction with soft phantoms with nodule embedded at 3 different depth levels, d. This results in a total of 15 unique interaction conditions. For each combination of given probe's stiffness and nodule's depth level, 25 palpation trials were repeated to construct the memory primitives of the probe. The memory primitives resulted from the training phase of the probe are shown in Figure 7.4.

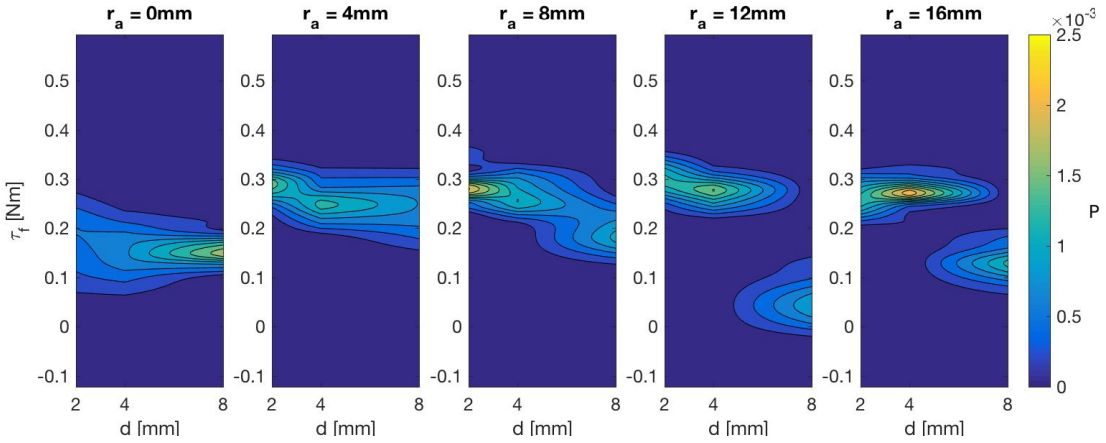

Fig. 7.4 Sample of memory primitives computed as probability function of the de-noised torque profiles from 25 learning trials given different probe's internal stiffness levels, denoted by r_a. Each of the memory primitives represents the probability of torque during the interaction with the probe with internal stiffness, r_a = 0, 4, 8, 12, and 16 mm respectively.

For Experiment 2, the memory primitives of peak torque were constructed across 5 levels of stiffness rating, r_a, 5 levels of indentation, i, and 3 levels of PSV, v_{probe}, during the interaction with soft phantoms with the nodule embedded at 3 different depth levels, d. This results in a total of 225 unique interaction conditions. For each combination of given probe's stiffness and nodule's depth level, 25 palpation trials were repeated to construct the memory primitives of the probe. Here, only 81 interaction conditions are depicted as examples of memory primitives from the probe's training phase as shown in Fig. 7.5 (a), (b), and (c).

7.3.2 Bayesian inferencing framework

From the non-linear relationship between the measured torque at the base, τ_f, the depth of buried nodule, d, and the behavioral variables of the probe, (r_a for Experiment 1, and r_a, i, and v_{probe} for Experiment 2) presented in the memory primitives, an appropriate stochastic machine learning technique can be implemented to understand the role of varying the probe's stiffness in solving the nodule's depth estimation problem during robotic palpation. It was found in [166] that the machine learning algorithm that holds the closest characteristics to that occurs in the central nervous system in the brain for solving the interpretation and the estimation problem is "Bayesian" decision process. This involves the systematical recruitment

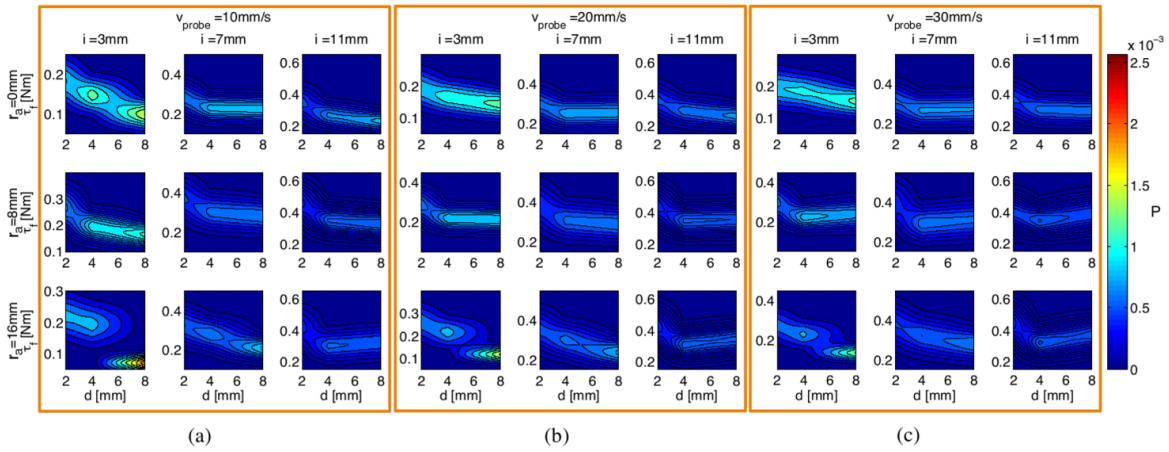

Fig. 7.5 The sample of memory primitives shown here consist of those when the PSV, $v_{probe} = 10, 20$, and 30 mm/s, in subfigures (a), (b), and (c), for the indentation level, i, of 3, 7, and 11 mm, and the stiffness of the joint denoted by r_a, of 0, 8, and 16 mm.

of prior beliefs and the likelihood from the past experience. Therefore, in this chapter, for the estimation of the nodule's depth using the robotics probe, Bayesian Inference approach was used to analyze the real-time captured peak torque data during the palpation over the nodule embedded inside silicone phantom.

This chapter explores the implementation of Bayesian inferencing approach in estimation of the nodule's depth given the different scenarios in controlling the behavioral variables, including keeping these variables stationary across iterations. The memory primitives constructed under the probe's stiffness space during the training phase were used to estimate the depth of the nodule. The iterative equation for Bayesian inferencing algorithm was as follows:

$$P_t(d|\tau_f) = \frac{P(\tau_f|d,\xi)P_{t-1}(d)}{\sum_{n=1}^{m} P(\tau_f|d_n,\xi)P_{t-1}(d_n)}, \tag{7.2}$$

where t is the current estimation iteration, n is the index of d, and $m = 3$ is the number of possible nodule depths. $P_t(d|\tau_f)$ represents the posterior probability distribution of nodule's depth given the measured torque, τ_f computed from the prior distribution $P_{t-1}(d)$ and the sampling or likelihood probability distribution of torque, $P(\tau_f|d,\xi)$ given depths and different set of behavioral variables (Experiment 1: $\xi = r_a$, and Experiment 2: $\xi = \{r_a, i, v_{probe}\}$) presented in the memory primitives, φ. The posterior computed at each iteration was then

used to update the probability distribution of the depth as a prior distribution in the next iteration. The initial prior of the function $P_{t=0}(d)$ had a flat distribution across different depths, reflecting the unbiased probability.

7.3.3 Kullback Liebler divergence

In general, the common influences of multiple coupled systems and factors can be quantified through the directed information exchanges by measuring the information transfer entropy, also known as relative entropy [159]. For example, the combination of internal stiffness, indentation level, and PSV; and the torque sensor reading can be assigned to be random variables (RV-A) and (RV-B) respectively. While the mutual information of two coupled variables between RV-A and RV-B does not change with the exchanges of variables; the transfer entropy from RV-A to RV-B is not identical to that from RV-B to RV-A. Transfer entropy can be quantified using Kullback-Liebler (KL) divergence.

In particular, KL-divergence can be used to assess whether further information regarding the nodule's depth estimation can be gained by taking another action (further iteration in Bayesian nodule's depth estimation procedure). If a set of $P_t(d|\tau_f)$ computed at the end of each Bayesian iteration is considered as the hypothesis of the depth estimation, its entropy for a given torque measurement, τ_f, is dependent on a set of probing behavioral variables, ξ (stiffness, PSV, and etc.). KL-divergence defined in equation (7.3) represents the information gained, G_t, about the relationship between the hypothesis of depth estimation, $P_t(d)$, and τ_f across iterations of Bayesian Inference as well as across different combinations of probing behavioral variables. Therefore, KL-divergence is a good measure to quantify the gain of different actions underlying the changes in the behavior.

$$G_t = P_t(d|\tau_f) \log \frac{P_t(d|\tau_f)}{P_{t=0}(d)}, \tag{7.3}$$

$P_t(d|\tau_f)$ represents the probability distribution of depth estimation which is obtained from the Bayesian inference shown in Equation (7.2) at t^{th} iteration, and $P_{t=0}(d)$ represents the base hypothesis about the nodule's depth estimation.

Kullback-Liebler transfer entropy could be implemented in addition to the Bayesian Inference method to determine the number of measurements required to estimate the nodule's depth by computing the correlation distance δ, between information gain of the current hypothesis, G_t, and that of the prior hypothesis G_{t-1}, in relation to the base prior distribution $P_{t=0}(d)$, as shown in Equation (7.4).

$$\delta = \frac{(G_t - \bar{G}_t)(G_{t-1} - \bar{G}_{t-1})'}{\sqrt{(G_t - \bar{G}_t)(G_t - \bar{G}_t)'}\sqrt{(G_{t-1} - \bar{G}_{t-1})(G_{t-1} - \bar{G}_{t-1})'}}, \tag{7.4}$$

where

$$\bar{G}_t = \frac{1}{m}\sum_n G_{tn}. \tag{7.5}$$

The palpation process stopped at the point where the correlation distance was less than empirically specified threshold $T = 0.0005$, signifying that there was none to little change in the information gained across iterations. Therefore KL-divergence can be used as an indication as to whether the estimation process requires further iterations to obtain more information.

7.4 Experiment 1: Bayesian haptic perception under stiffness's framework

7.4.1 Bayesian haptic perception with information gain metrics with stationary probe's stiffness

The first experiment involved the implementation of Bayesian inferencing algorithm together with the Kullback-Liebler transfer entropy for nodule's depth estimation while the probe's stiffness was kept stationary. The iterative equation used in the estimation process is shown in Equation (7.2), where $\xi = r_a$. At the end of each iteration, the transfer entropy based on KL-divergence, G_t, shown in Equation (7.3) was computed to determine whether sufficient information was gained to make the estimation. The estimated depth was computed from the maximum likelihood found. The depth estimation procedure is shown in Algorithm 7.4.

Algorithm 7.1: Nodule's depth estimation algorithm using Bayesian Inference and KL divergence

function DepthEstimation $(\tau_f(d_r, r_a))$;
Input : Real time torque reading, $\tau_{f,t}(d_r, r_a)$
Output : Depth estimation accuracy
Create memory primitives;
for *each set of probe's stiffness,* r_a*, and actual nodule's depth,* d_r **do**
  $t = 0$;
  while $\delta > T$*, the threshold* **do**
    $t = t + 1$;
    Retrieve and process new $\tau_{f,t}$ given known probe's stiffness r_a from the sensor reading;
    Compute $P(\tau_{f,t}|d, r_a)$ from $\boldsymbol{\varphi}$;
    Recall prior distribution of hypothesis of nodule's depth $P_{t-1}(d)$;
    Compute $P_t(d|\tau_f)$ using Equation (7.2);
    Store posterior distribution as a prior distribution for the next iteration;
    Compute G_t using Equation (7.3);
    Compute correlation distance, δ, between G_t and G_{t-1}, using Equation (7.4) ;
  Find maximum depth likelihood from $P_t(d|\tau_f)$, which reflects the estimated depth, $d_{est} = \underset{m}{\operatorname{argmax}}(P_t(d|\tau_f))$;
Compute the nodule's depth estimation accuracy

Results

Figure 7.6 exhibits the example of the progression of the nodule's depth estimation (expected value and standard errors) across Bayesian inferencing iterations. As shown in these figures, the algorithm did not make any progress towards the convergence nor any change in the estimation as the Bayesian algorithm progressed. This may be resulting from the fact that the Bayesian inferencing algorithm was allowed to observe only in a single memory primitives by keeping the probe's stiffness stationary.

By implementing the Bayesian inference algorithm, an overall estimation accuracy of 66.7% with the accuracy of 80%, 60%, 60% for nodule embedded at d_r =2, 4, and 8 mm, respectively (shown in Figure 7.10, orange bars) was obtained. The result on the estimation accuracy exhibited similar trend to that obtained in human experiment in Chapter 3, where the depth of nodule embedded closer to the exposed surface of soft silicone phantom can be approximated more easily. It is important to note here that though the results show that on

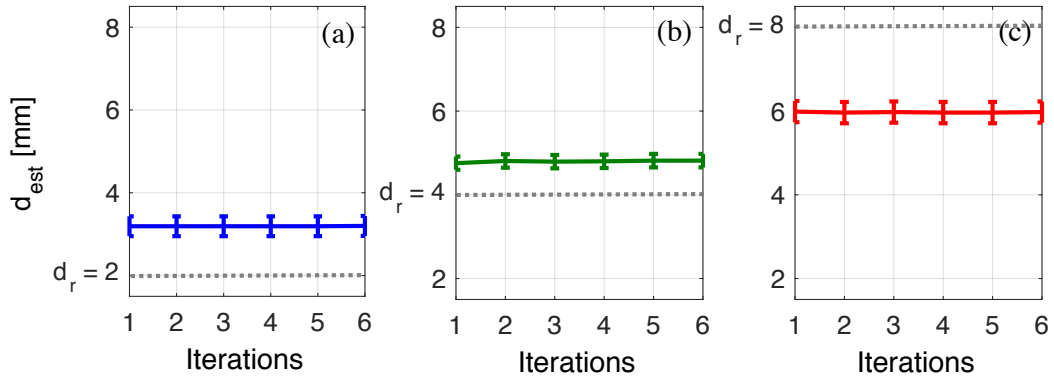

Fig. 7.6 The example of mean and standard errors of the estimated nodule's depth at each Bayesian iteration, across which the probe's stiffness remains stationary. The actual depths of the nodule assessed here include $d_r = 2$, 4, and 8 mm, shown in (a), (b), and (c) respectively. The actual depth is represented by dotted grey line.

average the robotic probe provides slightly enhanced nodule's depth estimation accuracy in comparison to those conducted by human (shown in Figure 7.10, green bars); it cannot be misinterpreted that the fixed stiffness strategy (performed by robotic probe) can outperform the human's finger stiffness control strategy. The differences in the absolute values of accuracy obviously came from the robot's ability to retrieve multiple memories with perfect accuracy and to be able to sense using an advanced sensor. The next section explores how human's strategy in estimating nodule's depth obtained in previous experiment can be implemented to increase the estimation accuracy.

7.4.2 Bayesian haptic perception with information gain metrics computed based on human's stiffness control strategy

This section explores whether the variation of probe's joint stiffness like human can improve the efficacy in the estimation of the nodule's depth. The extracted human's co-contraction strategy in palpation in the form of a Markov chains were implemented in the Bayesian haptic perception with variable probe's stiffness across iterations for nodule's depth estimation algorithm. Unlike the algorithm used in previous section where the estimation procedure was constrained by the exploration under a single memory primitive (fixed probe's stiffness) across iterations; this active Bayesian algorithm allowed change in the probe's stiffness across iterations. The probe's stiffness across each iteration was modulated based on the Markov

Table 7.2 Probe's stiffness equivalent to average human's co-contraction levels

Human's ave. co-contraction levels	0.1	0.2	0.3	0.4	0.5
Probe's internal stiffness, r_a **[mm]**	0	4	8	12	16

decision matrices obtained in Section 3.3.2 and current level of probe's stiffness. In order to utilize the Markov decision matrices, the levels of probe's stiffness available in memory primitives were corresponded with the co-contraction levels from the Markov decision matrices as shown in Table 7.2.

This section explores whether the accuracy of nodule's depth estimation can be enhanced by the modulation of probe's stiffness based on human's co-contraction strategy in palpation. In order to assess this, a similar estimation procedure as shown in Algorithm 7.2 was performed. At the end of each iteration, the probe's stiffness was controlled based on the Markov chain rule. This process was repeated for 100 trials for each phantom.

Algorithm 7.2: Nodule's depth estimation algorithm using Bayesian inference and KL divergence with human's co-contraction strategy

function DepthEstimation $(\tau_f(d_r, r_a))$;
Input : Real time torque reading, $\tau_{f,t}(d_r, r_{a,t})$
Output : Depth estimation accuracy
Create memory primitives;
for *each soft silicone phantom with actual nodule's depth,* d_r **do**
  $t = 0$;
  while $\delta > T$, *the threshold* **do**
    $t = t + 1$;
    Retrieve and process new $\tau_{f,t}$ given known probe's stiffness $r_{a,t}$ from the sensor reading;
    Compute $P(\tau_{f,t}|d, r_{a,t})$ from $\boldsymbol{\varphi}$;
    Recall prior distribution of hypothesis of nodule's depth $P_{t-1}(d)$;
    Compute $P_t(d|\tau_f)$ using Equation (7.2);
    Store posterior distribution as a prior distribution for the next iteration;
    Compute G_t using Equation (7.3);
    Compute correlation distance, δ, between G_t and G_{t-1}, using Equation (7.4);
    Compute next probe's stiffness level, $r_{a,t+1}$**, from** $M_{mk}(r_{a,t})$ using Equation (3.4);
  $d_{est} = \underset{m}{\text{argmax}}(P_t(d|\tau_f))$;
Compute the nodule's depth estimation accuracy

The graphical representation of the nodule's depth estimation process using Bayesian inference and KL divergence with human's co-contraction strategy is shown in Figure 7.7. The example of a single assessment trial as the estimation process progress with the posterior computation using Bayesian inference in each iteration including the computation of the likelihood function from the memory primitives are shown in Figure 7.8. The prior assumption at $t = 1$ represents the flat distribution P_0, signifying unbiased distribution at the beginning of the process. The process began in first iteration $t = 1$ by capturing the real-time torque, $\tau_{f,1}$ during the first palpation iteration given the arbitrarily chosen probe's stiffness level $r_{a,1}$. These information were then used to compute the likelihood function from memory primitives, $\boldsymbol{\varphi}$. The posterior was computed from the prior and the likelihood function in each iteration. At the end of each iteration the information gain, G_t, was computed and the correlation distance between current information gain and that from the previous iteration was computed to determine whether the process has gained new information. The estimation process (as shown in this example in Figure 7.8) ended at $t = 5$. At the end of the process, the estimated depth d_{est} was computed from the posterior distribution.

Results

Figure 7.9 depicts the average nodule's depth estimation across 100 estimation trials at each Bayesian inferencing iteration. Since, most of the estimation trials tend to converge within 5 Bayesian iterations or less, the converging progression of the nodule's depth estimation are presented up to 6^{th} Bayesian iterations. As shown in these figures, as the Bayesian inferencing algorithm progressed, the nodule's depth estimation converged towards the actual nodule's depth, although this happened at different rate. The rate of the convergence was directly proportional to the nodule's depth. As the nodule was buried deeper from the exposed surface, the higher the number of iteration was required for the algorithm to converge. On the contrary to the previous algorithm, where the probe's stiffness was kept stationary across iteration (shown in Figure 7.6), this algorithm was allowed to explore in multiple memory primitives by regulating the joint's stiffness based on human's stiffness control strategy.

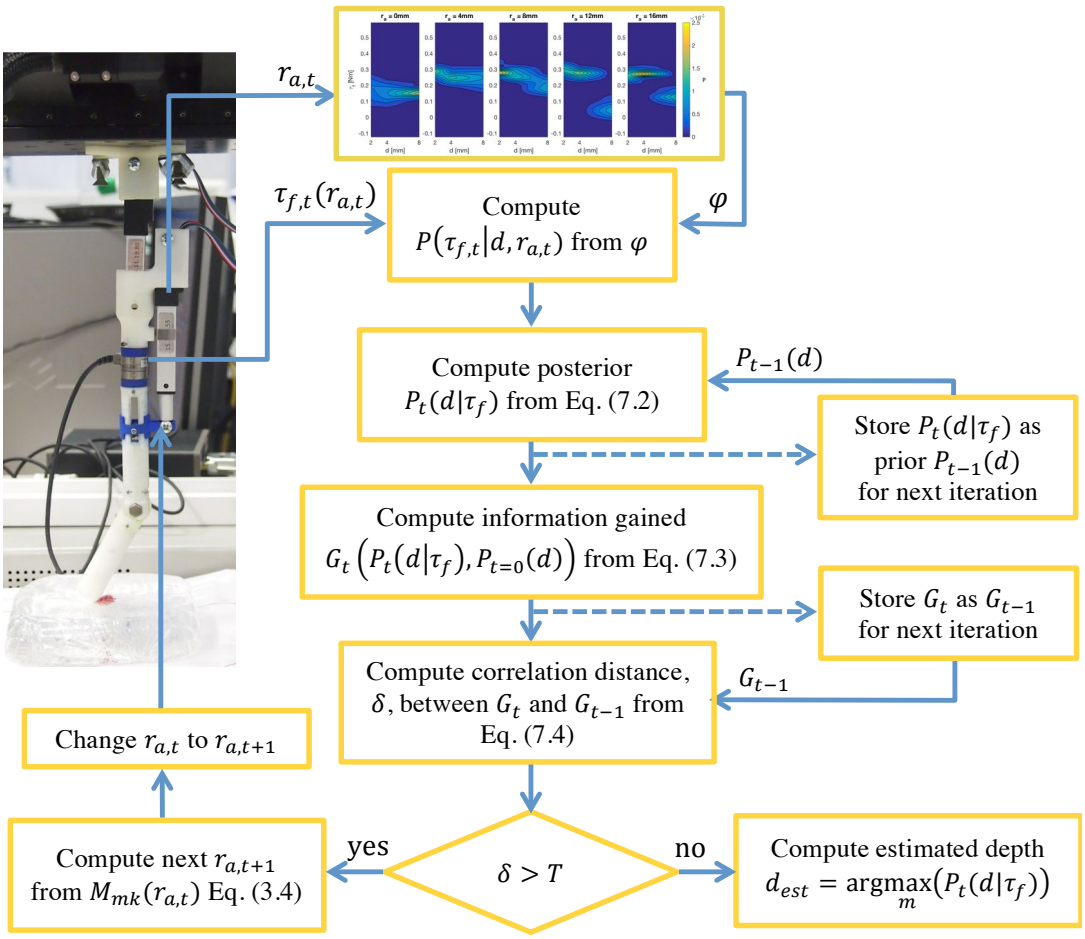

Fig. 7.7 Graphical representation of the nodule's depth estimation process using Bayesian inference and KL divergence with human's co-contraction strategy.

Therefore, this allowed the depth's estimation to converge towards the actual nodule's depth, d_r.

The overall average accuracy from 100 trials of nodule's depth estimation using Bayesian Inference with KL-Transfer Entropy together with the stiffness modulation based on average human's co-contraction strategy across iterations reaches slightly above 90% as shown in Figure 7.10 in blue bar. The estimation accuracy from all individual actual depths were also higher in comparison to those with stationary r_a (with overall accuracy of approx. 67%).

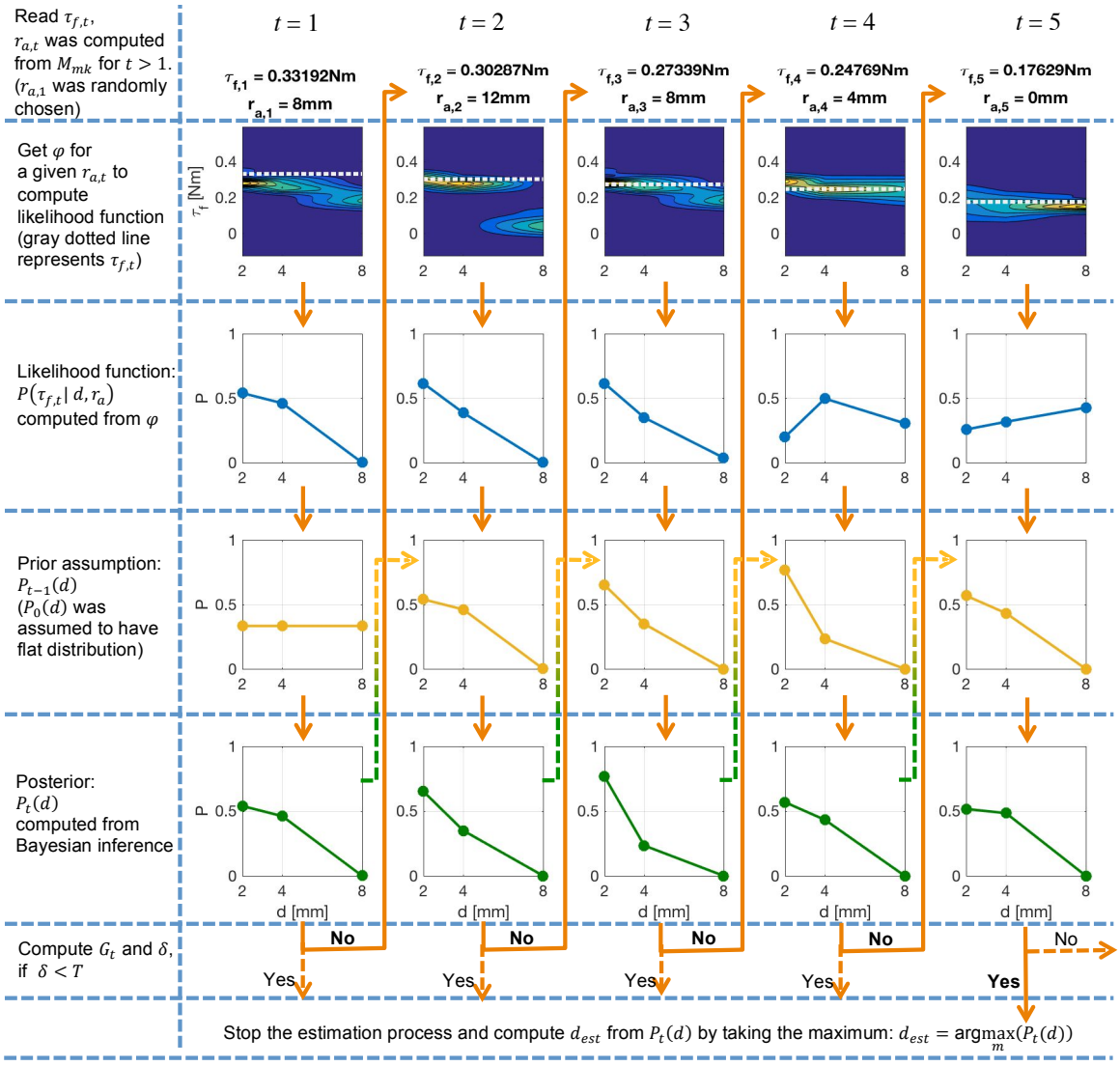

Fig. 7.8 In the first iteration of the nodule's depth estimation process, $r_{a,1}$ was randomly selected. Each iteration began by recording $\tau_{f,t}$ for given $r_{a,t}$. The chosen $r_{a,t}$ was used to select an appropriate set of memory primitive. The likelihood function was computed from the memory primitives as the probability of getting $\tau_{f,t}$ given $r_{a,t}$ for different d. The posterior was then computed from the likelihood and the prior. The process stops when the correlation distance δ of information gain G_t is less than specified threshold T.

7.4.3 Statistical analysis of the results

In addition, the ANOVA test was performed on the estimation result to assess the influence of the nodule's depth level and the probe's stiffness level, in the case where the probe's stiffness was kept stationary across iterations. The ANOVA revealed significant differences

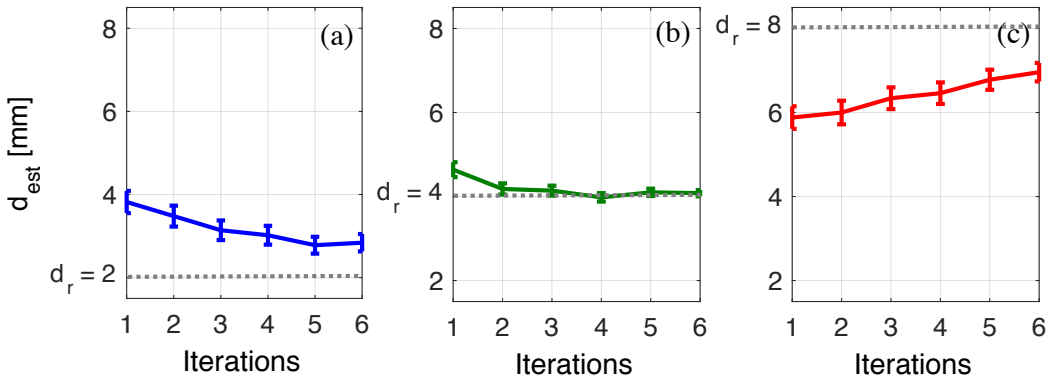

Fig. 7.9 The average of mean and standard errors of the estimated nodule's depth at each Bayesian iteration across 100 iterations with human's stiffness control strategy. The actual depths of the nodule assessed here include $d_r = 2$, 4, and 8 mm, shown in (a), (b), and (c) respectively. The actual depth is represented by dotted grey line.

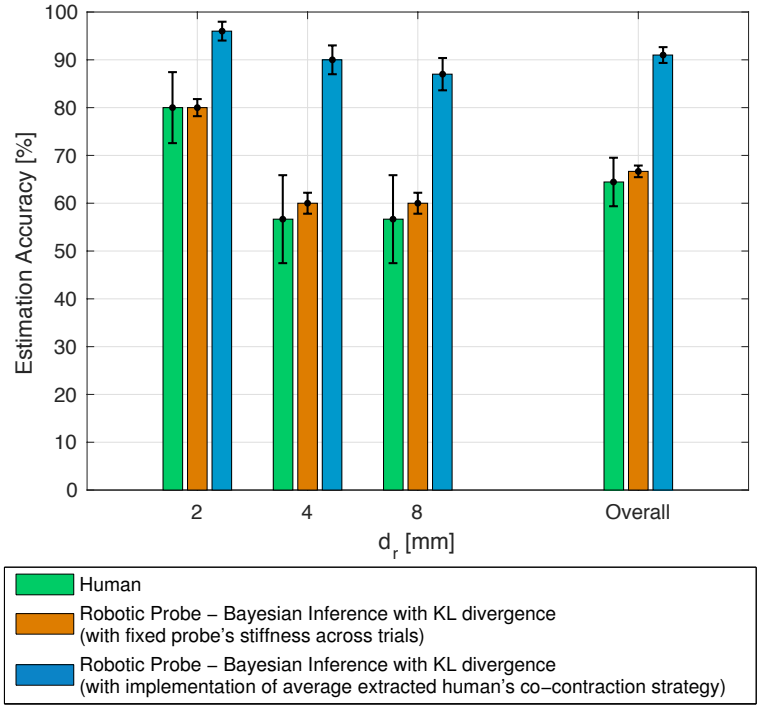

Fig. 7.10 Overall average nodule's depth estimation accuracy resulted from 1) average human's estimation across 6 subjects (shown in green), 2) the Bayesian Inference together with the KL-Transfer Entropy with fixed probe's stiffness across iterations (shown in orange), and 3) the Bayesian Inference together with the KL-Transfer Entropy with extracted human's co-contraction strategy (shown in blue).

between different nodule's depth levels ($p < 0.05$) as well as between the probe's stiffness level ($p < 0.05$). The interaction between the depth level and the probe's stiffness level was also

significant ($p < 0.05$). Post hoc comparisons using the Bonferroni correction revealed that for the estimation accuracy of the nodule embedded at 2 mm beneath the surface is statistically significantly higher than the other depth levels. For the cases, where nodule is embedded at 4 mm and below, the difference in the estimation accuracy was not significant. Post hoc comparison further suggests that the probe's stiffness level can be statistically separated into three groups based on the significant difference. The results suggest that the stiff probe (r_a = 16 mm) can statistically obtain higher accuracy when the probe's stiffness is fixed.

Multiple factor ANOVA with Bonferroni correction test was also performed on the nodule's depth estimation accuracy given different nodule's depths and different experiments (1. human (from Chapter 3), 2. robotic probe with static stiffness, and 3. robotic probe with variable stiffness generated from Markov stiffness probability transition matrices shown in Figure 3.3). Multiple factor ANOVA test revealed that the nodule's depth level had statistically significant influence on the estimation accuracy ($p < 0.05$), and the type of experiments also statistically significantly influenced the depth estimation results ($p < 0.05$). However, the interaction between these factors did not have statistically significant influence on the nodule's depth estimation ($p > 0.05$). Post hoc analysis reported that the estimation accuracy did not statistically significantly differ among the nodule's depth level of $d = 4$ mm and below; whereas depth level $d = 2$ mm yielded the most accurate estimation. The result from post hoc analysis also suggest that the result from the human experiment and the robotic probe with static stiffness did not differ statistically. On the other hand, the robotics probe can statistically significantly enhance the nodule's depth estimation accuracy when using variable stiffness strategy generated from Markov matrices as opposed to the static stiffness strategy ($p < 0.05$).

7.5 Experiment 2: Bayesian haptic perception under multiple behavioral variables framework

While it was evidently found in the first part of the experiments (Experiment 1) presented in this chapter that through the regulation of internal impedance can enhance the accuracy

during haptic perception; there may be some other behavioral factors that also contribute to the interpretation of the environment. It was observed that when people were asked to palpate a novel soft object to discern its physical properties, they did not only regulate co-contraction level of antagonistic muscles to control the mechanical impedance of fingers, but also the probing behavior, such as indentation and palpation velocity. It was suspected that such behavior tries to enhance haptic perception by regulating the function of mechanoreceptors at different depths of the fingertips and proprioceptive sensors such as tendon and spindle sensors located in muscles. Therefore, this experiment integrated both indentation level and probing velocity control, in addition to probe's stiffness control, to form 225 unique interaction conditions. The purpose of this experiment was to investigate whether in addition to stiffness control, the control of the probing exploratory strategy at multiple behavioral levels could enhance the efficacy of the information gain in enhancing the nodule's depth estimation.

7.5.1 Bayesian haptic perception with stationary behavioral variables

Table 7.1 shows different interaction conditions between the robotic probe and soft silicone phantom used to assess the performance of the Bayesian Inferencing Algorithm 7.3 to estimate d across 5 iterations. The assessment of the nodule's depth estimation was repeated for 10 trials in order to obtain the average accuracy of estimation. In each assessment trial, the memory primitives given different combinations of probe's interacting conditions were constructed from 25 randomly chosen learning trials.

Fig. 7.11 shows an example of a nodule depth estimation trial that consists of 5 iterations of Bayesian Inference for a given combination of probe's stiffness, indentation, and PSV. Each subplot shows the progression of the posterior probability of nodule's depth estimation starting from a flat distribution at $t = 0$ to a refined one at $t = 5$.

Result

The overall accuracy across 10 assessment trials in nodule depth estimation after each iteration and those for different nodule depth levels are shown in Fig. 7.12. On average, the overall

Algorithm 7.3: Nodule's depth estimation algorithm using Bayesian Inference

function DepthEstimation $(\tau_{f,t=1..5}(d_r, r_a, i, v_{probe}))$;
Input : Real time torque reading, $\tau_{f,t=1..5}(d_r, r_a, i, v_{probe})$
Output : Depth estimation accuracy
Define $P_{t=0}(d)$ as a flat distribution across different d;
for *each combination of* $\{r_a, i, v_{probe}\}$*, and actual nodule's depth,* d_r **do**
  for *each iteration* $t = 1..5$ **do**
    Retrieve and process new $\tau_{f,t}$ from the sensor reading, given known probing bahavior $\{r_a, i, v_{probe}\}$.;
    Compute $P(\tau_{f,t}|d, r_a, i, v_{probe})$ from $\boldsymbol{\varphi}$;
    Recall prior distribution of hypothesis of nodule's depth $P_{t-1}(d)$;
    Compute $P_t(d|\tau_f)$ using Equation (7.2);
    Store posterior distribution as a prior distribution for the next iteration;
    $d_{est} = \underset{m}{\text{argmax}}(P_t(d|\tau_f))$;

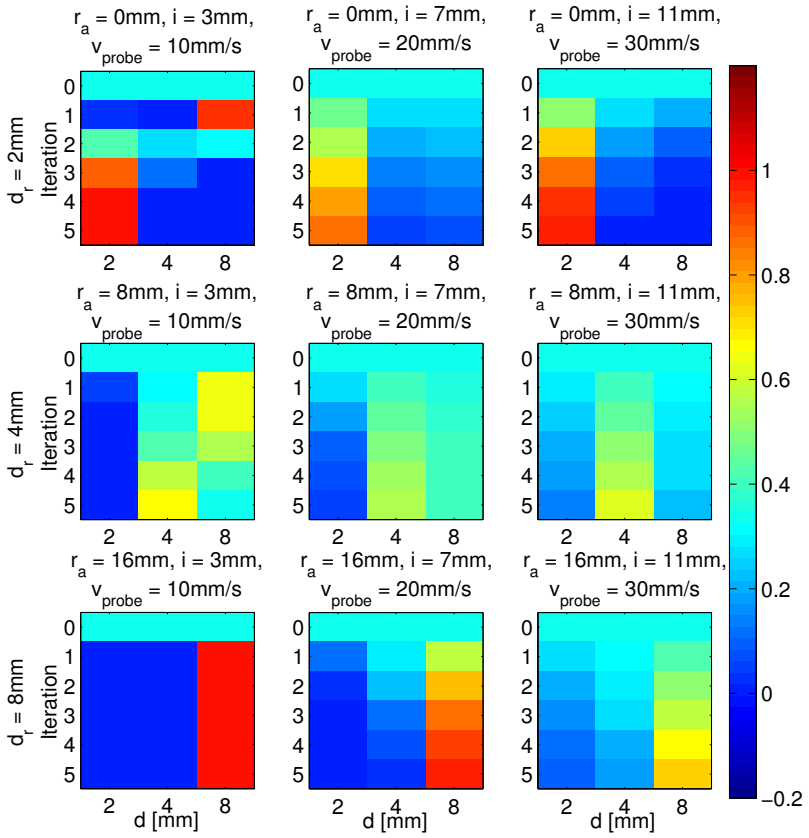

Fig. 7.11 Each plot depicts the distribution of depth estimation from the initially defined flat distribution at $t = 0$ to $t = 5$ given different combinations of probe's stiffness, indentation, and PSV. The real depths of nodule, d_r, assessed here were those known values associated with the memory primitives explained earlier.

nodule depth estimation accuracy increased from approximately 91% with standard deviation of 3.23% at the first iteration ($t = 1$) to 96% with standard deviation of 1.8% at ($t = 5$). The results showed that the estimation accuracy of nodule depth decreased as the nodule was buried deeper from the exposed surface from 99.3% at $d = 2$ mm to 95.2% and 94.2% at $d = 4$ and 8 mm, respectively. Higher iteration numbers caused the expected values of estimation accuracy for all depth ranges to increase and the standard deviations to decrease.

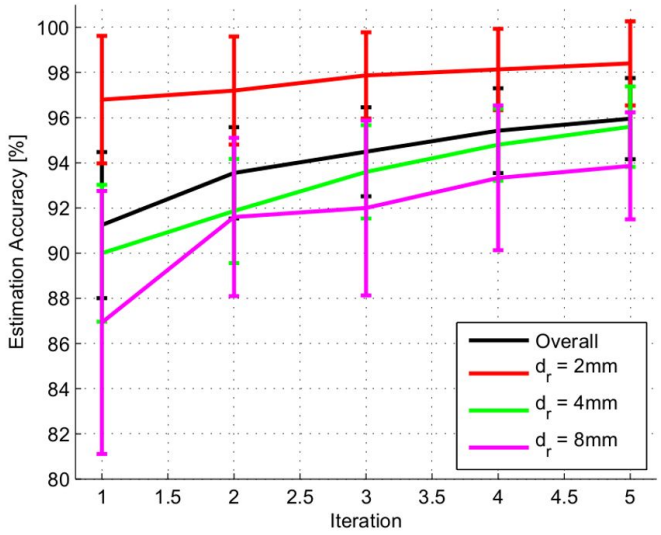

Fig. 7.12 The resulting overall nodule's depth estimation accuracy is shown in black line. The estimation accuracy for each actual depth, $d_r = 2, 4$, and 8 mm are shown in red, green and magenta lines respectively.

Further statistical analysis was performed to investigate the significance of r_a, i, and v_{probe}, on the depth estimation accuracy across all assessment trials. The Kolmogrov-Smirnov test showed that the nodule's depth estimation was not normally distributed ($p > 0.05$). Hence, the conventional Analysis of Variance (ANOVA) could not be performed. Therefore, a non-parametric Kruskal-Wallis method was applied. The resulting p-values from the test were $0.0002, 0.4715$, and 0.7394 for probe's stiffness, r_a, indentation, i, and PSV, v_{probe}, respectively over the course of 10 assessment trials across different combinations. Therefore, probe's stiffness, r_a, had statistically significant contribution towards the nodule's depth estimation accuracy (p-value < 0.05); while the variation of i and v_{probe} did not have significant influence.

The average accuracy in the estimation of nodule's depth given different probe's stiffness, r_a, indentation level ,i, and PSV, v_{probe} across 10 assessment trials are shown in Table 7.3, 7.4, and 7.5, respectively. It can be seen that the average nodule's depth estimation was slightly less accurate for the case when the joint of the probe was both stiffest and most relaxed; while it became most accurate when $r_a = 12$ mm. This suggests that the regulation of body's stiffness matters when making an estimation about the environment. Nonetheless, it is important to notice that the efficacy of $r_a = 12$ mm varied depending on the probing speed and the indentation used.

Table 7.3 Nodule's depth estimation accuracy across r_a

	r_a [mm] **(Probe's stiffness)**				
d_r [mm]	**0**	**4**	**8**	**12**	**16**
2	96.7%	98.7%	98.7%	99.3%	98.7%
4	90.7%	97.3%	93.3%	98.7%	98%
8	95.3%	73.3%	92.7%	100%	98%
Overall	94.2%	93.1%	94.9%	99.3%	98.2%

Table 7.4 Nodule's depth estimation accuracy across i

	i [mm] **(Indentation)**				
d_r [mm]	**3**	**5**	**7**	**9**	**11**
2	94.7%	100%	100%	99.3%	98%
4	96%	94.7%	90%	98.7%	98.7%
8	79.3%	96%	90%	98.7%	95.3%
Overall	93.3%	96.9%	93.3%	98.9%	97.3%

Table 7.5 Nodule's depth estimation accuracy across v_{probe}

	v_{probe} [mm/s] **(probing vel.)**		
d_r [mm]	**10**	**20**	**30**
2	97.6%	100%	97.6%
4	96.4%	94.4%	96%
8	88%	96%	97.6%
Overall	94%	96.8%	97.1%

Furthermore, Figure 7.11 suggests that the posterior distribution of nodule's depth estimation can converge at different rates depending not only on the combination of r_a, i, and

v_{probe}, but also on the noise level of real-time sensor measurements in each iteration and the chosen memory primitives in the likelihood function. This leaded to the question as to how the number of iteration/exploration required to make an accurate estimation of the nodule depth can be determined. This question can be addressed by computing the information transfer entropy in each iteration.

7.5.2 Bayesian haptic perception with information gain metrics with stationary behavioral variables

In addition to the Bayesian Inference method for estimating the depth of the nodule from the real-time captured torque data, here Kullback Liebler divergence was implemented at the end of each Bayesian iteration to determine whether further measurement was required to accurately estimate the nodule's depth. This additional process was carried out by computing the correlation distance, δ, (using Equation (7.4)) between information gain from the current hypothesis, G_t, and that from the prior hypothesis, G_{t-1}, in relation to the base prior distribution, $P_{t=0}(d)$. No further measurement was necessary to make an accurate estimation when the correlation distance, δ, was less than the empirically specified threshold of $T = 0.0005$. This signified that there was negligible change in the information gained across the iterations and the distribution of the nodule's depth estimation hypothesis has converged. The depth estimation procedure is shown in Algorithm 7.4. Similar to the process presented in previous section, the assessment of the nodule's depth estimation was repeated for 10 assessment trials to obtain the average accuracy in the estimation. In each assessment trial, the memory primitives given different combinations of probe's interacting conditions were constructed from 25 randomly chosen learning trials.

Result

With the implementation of KL-divergence in addition to the Bayesian Inference algorithm, the nodule's depth estimation process required on average of only 2.8 iterations with standard deviation of 1.2 iterations to converge. While the number of iterations required for convergence was kept to minimum; the nodule's depth estimation accuracy still reached within the

Algorithm 7.4: Nodule's depth estimation algorithm using Bayesian Inference and KL divergence

function DepthEstimationKL($\tau_f(d_r, r_a, i, v_{probe})$);
Input : Real time torque reading, $\tau_{f,t}(d_r, r_a, i, v_{probe})$
Output : Depth estimation accuracy
Define $P_{t=0}(d)$ as a flat distribution across different d;
for *each combination of* $\{r_a, i, v_{probe}\}$*, and actual nodule's depth,* d_r **do**
    $\delta = 1$ Initialize correlation distance to 1;
    $t = 0$ Initialize the number of iteration to 0;
    $G_0 = 0$ Initialize the information gain at $t = 0$ to 0;
    while $\delta > T$ **do**
        $t = t + 1$;
        Follow Step 5-9 in Algorithm 7.3;
        Compute G_t using Equation (7.3);
        Compute δ between G_t and G_{t-1}, using Equation (7.4);
    $d_{est} = \underset{m}{\text{argmax}}(P_t(d|\tau_f))$;
Compute the nodule's depth estimation accuracy.

comparable range to that with fixed 5-iterations in the inferencing algorithm presented in Algorithm 7.3. On average the overall depth estimation accuracy was approximately 96.2% as shown in Fig. 7.13 (orange bars). The accuracy of nodule's depth estimation for each actual depth were approximately $98.4\%, 95.3\%$, and 94% for $d_r = 2, 4$, and 8 mm respectively. These results showed that this method minimized the number of explorations needed to make an accurate estimation about the depth of the nodule. Therefore, it can be concluded that Bayesian Inference together with KL-divergence provides a real-time framework to estimate the convergence to an optimal estimate of nodule depth in the sense of information gain.

7.5.3 Active Bayesian haptic perception with information gain metrics

So far, Experiment 2 involved keeping r_a, i, and v_{probe} constant given a set of probing iterations in each estimation trial. However, biological counterparts like humans regulate the internal impedance more like a random variable within a given probing attempt. Therefore, further experiments was carried out to explore whether the nodule's depth estimation accuracy can be enhanced by allowing changes in the combination of probe's stiffness, indentation

level, and PSV across trials. This allows the estimation process to explore in multiple search spaces (memory primitives).

Algorithm 7.5: Nodule's depth estimation algorithm using Bayesian Inference and KL divergence

```
function DepthEstimationKLR(τ_f(d_r, r_a, i, v_probe));
Input  : Real time torque reading, τ_{f,t}(d_r, r_{a,t}, i_t, v_{probe,t})
Output : Depth estimation accuracy
Define P_{t=0}(d) as a flat distribution across different d;
for each actual nodule's depth, d_r do
    Follow Step 4-6 in Algorithm 7.4;
    while δ > T do
        t = t + 1;
        Randomly select combination of {r_{a,t}, i_t, and v_{probe,t}};
        Follow Step 9-11 in Algorithm 7.4;
    d_est = argmax_m(P_t(d|τ_f));
Compute the nodule's depth estimation accuracy.
```

In order to address this, a similar estimation algorithm to that shown in Algorithm 7.4 was repeated. However, instead of the static combination of probe's stiffness, indentation level, and probe sweeping velocity; these variables were allowed to arbitrarily vary across iterations in the nodule's depth estimation process. The nodule's depth estimation process was repeated for 100 trials for each artificial soft silicone phantom with nodule embedded at $d_r = 2, 4$, and 8 mm. The estimation procedure is shown in Algorithm 7.5. At the beginning of the estimation procedure, the process randomly selected the probe's stiffness, indentation level, and PSV combination. In each iteration, this combination was arbitrarily varied to allow the exploration in the other memory primitives to infer the previous posterior.

Result

The nodule's depth estimation result from the implementation of the Bayesian Inference with dynamic probing shown in Algorithm 7.5 are shown in blue bar in Fig. 7.13. The overall average accuracy from 100 trials using this algorithm as the estimation hypothesis converged, reached 99% with standard deviation of 0.5%. For each individual depth level, the average estimation accuracy were all significantly higher; while the corresponding standard deviations

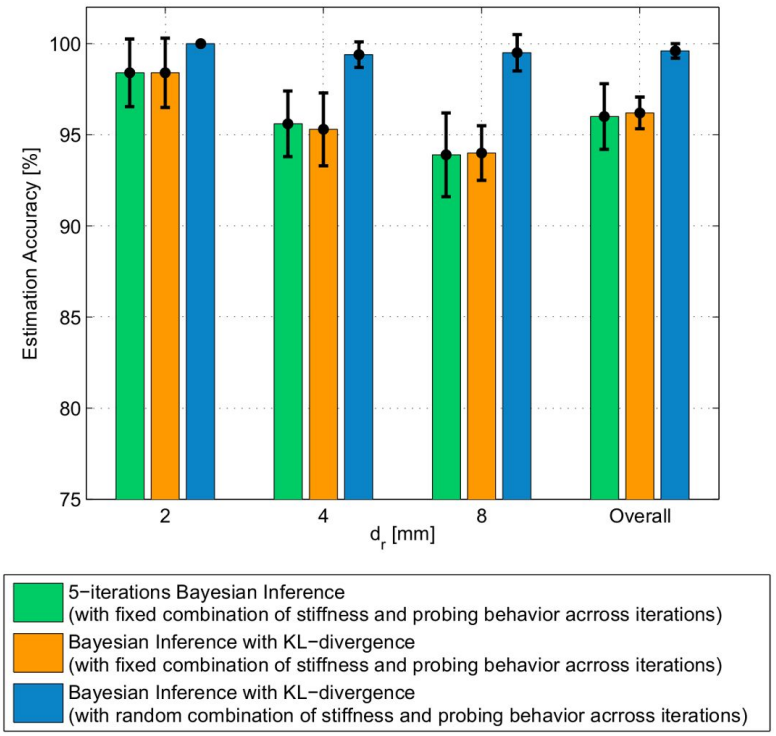

Fig. 7.13 1) 5-iteration Bayesian inference without KL-divergence (shown in green), 2) the Bayesian Inference together with the KL-Transfer Entropy with fixed probe's stiffness , indentation level, and PSV (shown in orange), and 3) the Bayesian Inference together with the KL-Transfer Entropy with random probe's stiffness, indentation level, and PSV (shown in blue).

were lower compared to those from the Bayesian inference with static set of probe's stiffness, indentation level, and PSV combinations. The result from this assessment also confirmed the initial hypothesis that the average number of iterations required to perform accurate depth estimation was kept to a minimum at approximately 3 iterations with standard deviation of 1.3 iterations.

7.6 Discussion

This chapter investigated both individual and collective role of the probe's internal stiffness, indentation level, and PSV in the accuracy in interpreting and estimating an environmental feature (depth of a nodule) by controlling a soft probe. The purposes of the experiments

presented in this chapter were: 1) to understand the necessity for the internal impedance regulation in biological as well as artificial active haptic perception, and 2) to investigate the influence of multiple behavioral variable probe in active haptic perception as well as to explore the possible implementation of such concept in the soft robotic probe. The soft robotic probe used in both experiments presented in this chapters comprised of a variable stiffness joint and an indentation level control mechanism. The probe structure was mounted under an XY-stage allowing the planar movement.

The non-linear relationship between the probe's measured torque, its internal variables, and the environment (depth of nodule in silicon phantom) were presented in the form of a probabilistic distribution given different combinations of probe's internal stiffness, indentation level, and PSV. In this thesis, these conditional probability distributions are referred to as 'memory primitives'. These 'memory primitives' functioned as likelihood functions in a Bayesian framework to estimate the depth of a nodule in the soft tissue phantom.

In Experiment 1, the robotic probe with the implementation of human's co-contraction strategy was compared with the case, where the robotic probe attained the stationary stiffness level across Bayesian iterations. The experimental results showed that the efficacy of haptic perception does not depend only on the configuration of the finger as reported in previous studies [165] on passive perception, but also on the way internal impedance of the finger was regulated. The results from the experiment with human subjects presented in Chapter 3 suggested that humans perform active exploration during manual palpation. Using the robotic probe, it was shown that active probing allows the integration of knowledge available so far with new evidence accompanied by active regulation of bodily parameters like the joint stiffness. With active stiffness control probing strategy presented in Section 7.4.2, the robotic probe can improve accuracy in estimation from approximately 70% to 90% through active exploration in a Bayesian inferencing framework, when the nodule's depth is one out of 3 known discrete depths. Active Bayesian haptic perception in a robotic probe involves stiffness variation following a Markov decision process identified using human muscle co-contraction data. The increase in accuracy is mainly due to the ability of the estimation process to search in multiple memory primitive spaces as opposed to a single one in case of the passive mode.

Therefore, it can be concluded that the internal impedance control plays an important role in robotic haptic perception and in that of the biological counterparts.

However, during human's manual palpation, the palpating behavior did not solely emerge from the regulation of muscle co-contraction alone, but also the other behavioral variables, like the indentation and the speed as well. This chapter posed the hypothesis that the regulation such behaviors can also be used to enhance the haptic perception as well. In addition to the probe's joint stiffness regulation, Experiment 2 also integrated the control of indentation and probe sweeping velocity during the depth estimation process as well.

The purpose of the Experiment 2 was to investigate the question as to how the probe with controllable stiffness, indentation level, and PSV can exploit its past experience of palpation to estimate the depth of a nodule embedded inside a soft tissue in real time. The experimental results suggested that the implementation of Bayesian Inference allows the algorithm to accurately estimate the depth of a nodule from the measured torque real-time. Furthermore, KL-divergence was introduced to determine whether further iteration of measurement was required to make an accurate estimation by comparing the information gained in the current iteration to that of the previous iteration. It was shown that on average the estimation processes using Algorithm 7.4 and 7.5 required approximately 3 iterations to converge in order to obtain comparable and better (in the latter) estimation accuracy. Allowing the combination of probe's internal stiffness, indentation level, and PSV to randomly vary across iterations (allowing exploration in multiple memory primitives in each nodule's depth estimation process), resulted in a convergence to the global optimum with a minimum number of iterations. The results showed that, this could enhance the average depth estimation accuracy to almost 100% with higher repeatability (smaller standard deviation).

In summary, the results from both sets of experiments suggest that by allowing the estimation process to vary the robotic probe's behavioral variables across estimation iteration, the estimation accuracy of an embedded nodule's depth can be significantly enhanced in comparison to maintaining the probe's behavioral variables across iteration, when the nodule's depth is one out of 3 known depths. It is important to note that the estimation accuracy also depends on the quality of the memory primitives constructed from the torque information

during learning trials. In addition, the accuracy in the nodule's depth estimation can drop if the depth was continuous.

Chapter 8

Conclusion

Morphological computation in biological systems, as well as in artificial systems, like robots for instance, is not solely responsible for the actuation but also for perception. For example, when people are asked to estimate the weight of an object on the hand, they do not hold the object with the static hand and arm. But the weighing activity of humans involve the movement of the arm, generally by bobbing the object up and down to estimate the weight. By performing such activities, humans change their co-contraction level, i.e. internal impedance, to condition the proprioception based on the co-contraction levels and the movement of the overall structure of the arm. This process is often referred to as "active sensing", which also very much involves the changes or control in the properties of the sensory receptors.

The nature of sensorimotor networks in biological system has been greatly influencing the design and approach towards the biologically-inspired artificial systems. For example, it has been shown that the understanding of the co-ordination of motor and sensory correlation patterns in human (often referred to as "synergy") could well lead to an advancement and optimization of design of artificial system like wearable device, such as glove-based "Hand Pose Reconstruction" system [167]. Furthermore, it was shown in [140] that humans can exploit stiffness synergy from their muscle pair controlling the impedance of the fingers' joints to control stable robotics hand's grasping.

In addition to the contribution of internal impedance control in enhancing the efficiency and stability in action, this thesis has explored the role of internal impedance control in

proprioception and in an embodied haptic perception. The purposes of this thesis is to understand the action-perception coupling in proprioceptive cue in biological system, as well as to investigate possible approach for the artificial system like robot to benefit from such concept during active haptic exploration of the environment. This thesis has taken the task of soft object palpation to discern the physical property as a case study. This was to simulate the scenario of medical manual palpation performed by surgeons to locate tumors inside soft tissue. Medical literatures [135, 136] show that T-1 stage tumors can be modeled as spherical shape hard nodules. Since the focus of this thesis was to highlight the importance of the internal impedance of the probe in detecting a hard nodule in a soft tissue, the study presented in this thesis was limited to a spherical acrylic hard nodule buried at depths up to 8mm. This scenario represents the conditions of a typical manual tumor localizing procedure for a T-1 stage tumor.

First, this thesis introduced the study of the human's internal impedance control during haptic perception in the manual palpation task to estimate the depth of stiff abnormality embedded inside soft silicone phantom in **Chapter 3**. It was found that human subjects regulated their muscle co-contraction during the active exploration of soft phantom to discern the stiff-abnormality from the soft phantom. The human's muscle co-contraction strategy given different nodule's depth was extracted and presented in form of Markov decision matrix. It was found from the Markov matrices that there exists a relationship between the muscle co-contraction strategy and the property of the environment. Though it was understood from this study that humans regulate their muscle co-contraction governing the stiffness of the joint to condition the haptic feedback during the exploration, the influence of the joint stiffness control in haptic perceptual information gain was not fully understood. Therefore, this thesis exploited the alternative robotic approach to understand this phenomena.

This thesis used the robotic manipulator with variable joint stiffness and robotic probe with multiple behavioral variable described in **Chapter 4** to investigate the role of internal impedance in the information gain in proprioception. In the experiment presented in **Chapter 5**, the information gain metrics was used to indicate the appropriate joint stiffness to estimate the angular displacement (proprioception) from the torque felt at the base alone. It was

found that the ability of the robotic manipulator to adjust its compliancy level can lead to accurate estimation of its own internal variables. Therefore, it was interesting to further explore the influence of internal impedance on the perception of external environment.

Taking similar task of discerning physical properties of soft object as a case study, this thesis used the same robotic manipulator with variable joint stiffness as a variable stiffness probe. The experiment presented in **Chapter 6** involved the investigation of the role of internal stiffness control of the robotic probe during palpation on soft silicone phantom under the information gain metrics framework. It was found that the information gain responses depend on the influence from the probe's stiffness and environmental variables and also the interactions among them. In general, the average directional information gain was relatively higher for transitions from non-compliant to compliant and among compliant levels in comparison to those from compliant to non-compliant. This signifies that the exploratory process was more likely to gain information regarding the depth of the nodule by switching within the compliancy levels and from non-compliant probe to compliant one. These findings led to the question as to how this phenomenon can be used in an appropriate machine learning algorithm with different probe's stiffness control algorithm, in order to accurately estimate the property of the environment.

In the last set of experiments presented in this thesis in **Chapter 7**, the Bayesian inferencing approach was used to allow the estimation of the depth of a hard nodule embedded inside soft silicone phantom, similar to the experiment carried out by human subjects. The extracted human's muscle co-contraction strategy was implemented together with Bayesian inferencing algorithm and compared with the stationary probe's stiffness algorithm. It was found that by allowing the probe to regulate its stiffness level corresponding to those found in human based on Markov matrices, the accuracy of depth estimation can be statistically significantly increased. In addition to the probe's behavioral control at the stiffness level, the regulations of both indentation and probe sweeping velocity were also integrated in this study. The experimental results suggest that by allowing the process to arbitrarily emerge the unique combination of probe's behavioral variables in each Bayesian iteration during the depth estimation process, the estimation accuracy can be significantly increased

in comparison to that with static behavior. The information gain metrics was used in the Bayesian algorithm to determine the sufficient information gained in each iteration in order to control exploratory iterations.

In general, this thesis exploits the robotic probe and manipulator as an abstracted version of human's finger. The focus was mainly on the antagonistic muscle co-contraction controlling a single joint and the corresponding tendon, which were represented by the antagonistic springs and the force/torque sensor respectively. However, human's muscle co-contraction behavior during palpation may arise from multiple sources apart from the regulation of MCP joint stiffness, since human's finger is composed of multiple joints. Nonetheless, in order to isolate and study the effect of joint stiffness control on the tendon force/torque sensor located at the base as opposed to force measurement at the tip of the finger, the design of the robotic probe with single variable joint stiffness used in the experiment represents an abstracted version of human's finger. Therefore, an exact replica of a finger with multiple parameters cannot conclude anything clear about this particular effect. In addition, during human's manual palpation, the movement of the finger was not constrained within a single plane. However, if the experiment with robotic probe was carried out in similar manner (with movement trajectory), the effect of the variation of joint's stiffness in the estimation of nodule's depth cannot be properly assessed. Therefore, the probing direction of the robotic probe was kept to one plane to focus on the effect of the joint stiffness alone in information gain. Once these individual effects are well understood, they provide a firm foundation to design more complex robotic probing behaviors, which is beyond the scope of this thesis.

The results presented in this thesis provide additional evidences to this phenomenon in terms of how humans might be regulating proprioception through stiffness control of the muscles that carry the proprioceptive sensors. It was shown in [31] that humans employ sensorimotor memory in order to coordinate sensory feedback and motor control in dexterous manipulation of object. It was shown in this thesis using robotic approach that the integration of sensory feedback with past proprioceptive memory through the variation of internal impedance can also enhance the accuracy of estimation of the environment.

Furthermore, the results also provided important explanations about the role of morphological computation in haptic based probing of a soft object, as well as providing guidelines to design and control variable stiffness probes for physical examination. Certainly, the operational implementation of this probe should be further developed depending on different applications.

In the future, if the nodule at the deeper depth is to be detected, the robotic probe with a larger stiffness range should be designed. However, detecting the nodule at deeper depth is beyond the scope of this thesis. The maximum depth of the nodule detectable given the capability of this device is 8 mm. The shape and size of the nodule was spherical with 15 mm diameter and detecting the nodule of different geometrical properties may require additional complexities of the probe, which is beyond the scope of this thesis. The difference in the stiffness between the nodule and the soft phantom in the experiments represent an apparent contrast of the stiffness. If the contrast becomes less apparent, the use of the probe of higher sensitivity may be necessary.

Nonetheless, the fact that controllable internal stiffness helps to gain proprioception information is still valid in such a tool. However, additional complexities arising from factors such as variable friction and irregular surface conditions, which are not addressed in this thesis should be further examined. Future studies can also involve temporal control of probe stiffness, indentation, and speed to better understand diverse probing strategies used by different classes of human participants as seen in [41]. It would also be interesting to further investigate the activity inside the brain in processing the information during human's manual palpation task, in order to verify whether humans recall some sort of memory primitives by activating the cerebral cortex, particularly prefrontal cortex in frontal lobe for processing the short-term memory and the parietal lobe involving the sensory information integration. Such experiments can be carried out by observing the ECG signal from different parts of the brain during the activity similar to what has been described in Chapter 3.

Additionally, while the functionalities of both tactile and proprioceptive sensations have been extensively studied in biology [168–170], the integrative view on how the stimuli perceived from these sensations are organized, regulated, exchanged, and processed are still not fully

understood. Therefore, it would be interesting to further explore the sensory coordination and how the information exchange or inference can enhance the perception and interpretation of the environment during active exploration of an artificial system, i.e. robotic device.

References

[1] M. Lungarella and O. Sporns, "Mapping information flow in sensorimotor networks," *PLoS Comput Biol*, vol. 2, p. e144, 10 2006.

[2] rA. B. Vallbo and R. Johansson, "Properties of cutaneous mechanoreceptors in the human hand related to touch sensation," *Hum Neurobiol*, vol. 3, no. 1, pp. 3–14, 1984.

[3] R. S. Johansson and rA. B. Vallbo, "Tactile sensory coding in the glabrous skin of the human hand," *Trends in Neurosciences*, vol. 6, pp. 27–32, 1983.

[4] O. Dangles, C. Magal, D. Pierre, A. Olivier, and J. Casas, "Variation in morphology and performance of predator-sensing system in wild cricket populations," *The Journal of experimental biology*, vol. 208, no. 3, pp. 461–468, 2005.

[5] M. H. Dickinson, C. T. Farley, R. J. Full, M. A. R. Koehl, R. Kram, and S. Lehman, "How Animals Move: An Integrative View," *Science*, vol. 288, pp. 100–106, Apr. 2000.

[6] A. Simpkins, "Robotic tactile sensing: Technologies and system (dahiya, r.s. and valle, m.; 2013) [on the shelf]," *Robotics Automation Magazine, IEEE*, vol. 20, pp. 107–107, June 2013.

[7] R. E. Burke, "Sir charles sherrington's the integrative action of the nervous system: a centenary appreciation," *Brain*, vol. 130, no. 4, pp. 887–894, 2007.

[8] A. W. Goodwin and H. E. Wheat, "Sensory signals in neural populations underlying tactile perception and manipulation," *Annu. Rev. Neurosci.*, vol. 27, pp. 53–77, 2004.

[9] I. Birznieks, P. Jenmalm, A. W. Goodwin, and R. S. Johansson, "Encoding of direction of fingertip forces by human tactile afferents," *The Journal of Neuroscience*, vol. 21, no. 20, pp. 8222–8237, 2001.

[10] A. Goodwin, V. Macefield, and J. Bisley, "Encoding of object curvature by tactile afferents from human fingers," *Journal of neurophysiology*, vol. 78, no. 6, pp. 2881–2888, 1997.

[11] C. E. Connor and K. O. Johnson, "Neural coding of tactile texture: comparison of spatial and temporal mechanisms for roughness perception," *The Journal of Neuroscience*, vol. 12, no. 9, pp. 3414–3426, 1992.

[12] M. Hollins and S. R. Risner, "Evidence for the duplex theory of tactile texture perception," *Perception & psychophysics*, vol. 62, no. 4, pp. 695–705, 2000.

[13] K. Overvliet, J. B. Smeets, and E. Brenner, "The use of proprioception and tactile information in haptic search," *Acta Psychologica*, vol. 129, no. 1, pp. 83–90, 2008.

[14] L. Rincon-Gonzalez, J. P. Warren, D. M. Meller, and S. H. Tillery, "Haptic interaction of touch and proprioception: Implications for neuroprosthetics," *IEEE Transactions on Neural Systems and Rehabilitation Engineering*, vol. 19, pp. 490–500, Oct 2011.

[15] R. Pfeifer, E. Al, R. Pfeifer, M. Lungarella, and F. Iida, "Self-organization, embodiment, and biologically inspired robotics," *Science*, vol. 318, 2007.

[16] H. Geyer and H. Herr, "A muscle-reflex model that encodes principles of legged mechanics produces human walking dynamics and muscle activities," *Neural Systems and Rehabilitation Engineering, IEEE Transactions on*, vol. 18, pp. 263–273, June 2010.

[17] Y. Blum, S. Lipfert, J. Rummel, and A. Seyfarth, "Swing leg control in human running," *Bioinspiration & biomimetics*, vol. 5, no. 2, p. 026006, 2010.

[18] N. Sornkarn and T. Nanayakkara, "Can a soft robotic probe use stiffness control like a human finger to improve efficacy of haptic perception?," *IEEE Transactions on Haptics*, 2016.

[19] M. Grunwald, *Human haptic perception: Basics and applications*. Springer Science & Business Media, 2008.

[20] N. Sornkarn, M. Howard, and T. Nanayakkara, "Internal impedance control helps information gain in embodied perception," in *2014 IEEE International Conference on Robotics and Automation (ICRA), 2014*, pp. 6685–6690, May 2014.

[21] N. Sornkarn and T. Nanayakkara, "The efficacy of interaction behavior and internal stiffness control for embodied information gain in haptic perception," in *2016 IEEE International Conference on Robotics and Automation (ICRA)*, pp. 2657–2662, May 2016.

[22] N. Sornkarn, P. Dasgupta, and T. Nanayakkara, "Morphological computation of haptic perception of a controllable stiffness probe," *PloS one*, vol. 11, no. 6, p. e0156982, 2016.

[23] A. Ranasinghe, N. Sornkarn, P. Dasgupta, K. Althoefer, J. Penders, and T. Nanayakkara, "Salient feature of haptic-based guidance of people in low visibility environments using hard reins," *IEEE Transactions on Cybernetics*, vol. 46, pp. 568–579, Feb 2016.

[24] H. B. Wegiriya, N. Sornkarn, H. Bedford, and T. Nanayakkara, "A biologically inspired multimodal whisker follicle," in *2016 IEEE International Conference on Systems, Man, and Cybernatics (SMC)*, October 2016.

[25] S. A. A. Guaman, N. Sornkarn, H., and T. Nanayakkara, "The role of morphological computation of the goat hoof in slip reduction," in *2016 IEEE/RSJ International Conference on Intelligent Robots and Systems (IROS)*, October 2016.

[26] C. Wolf and D. E. J. Linden, "Biological pathways to adaptability – interactions between genome, epigenome, nervous system and environment for adaptive behavior," *Genes, Brain and Behavior*, vol. 11, no. 1, pp. 3–28, 2012.

[27] A. PROSS, "The driving force for life's emergence: Kinetic and thermodynamic considerations," *Journal of Theoretical Biology*, vol. 220, no. 3, pp. 393 – 406, 2003.

[28] T. Ziemke, "What's that thing called embodiment?," in *Proceedings of the 25th Annual Meeting of the Cognitive Science Society*, pp. 1305–1310, Mahwah, NJ: Lawrence Erlbaum, 2003.

[29] R. Pfeifer and G. Gomez, "Understanding intelligence," 1999.

[30] T. Ziemke, "Disentangling notions of embodiment," in *Workshop on Developmental Embodied Cognition*, p. 83, Citeseer, 2001.

[31] Q. Fu, W. Zhang, and M. Santello, "Anticipatory planning and control of grasp positions and forces for dexterous two-digit manipulation," *The Journal of neuroscience*, vol. 30, no. 27, pp. 9117–9126, 2010.

[32] M. R. Gover, "The embodied mind: Cognitive science and human experience (book)," *Mind, Culture, and Activity*, vol. 3, no. 4, pp. 295–299, 1996.

[33] L. W. Barsalou, P. M. Niedenthal, A. K. Barbey, and J. A. Ruppert, "Social embodiment," *Psychology of learning and motivation*, vol. 43, pp. 43–92, 2003.

[34] D. Vernon, R. Lowe, S. Thill, and T. Ziemke, "Embodied cognition and circular causality: on the role of constitutive autonomy in the reciprocal coupling of perception and action," *Frontiers in psychology*, vol. 6, 2015.

[35] S. Hurley, "Active perception and perceiving action: The shared circuits model," *Perceptual experience*, pp. 205–259, 2006.

[36] M. Hoffmann and R. Pfeifer, "The implications of embodiment for behavior and cognition: animal and robotic case studies," *CoRR*, vol. abs/1202.0440, 2012.

[37] T. J. Prescott, M. E. Diamond, and A. M. Wing, "Active touch sensing," *Philosophical Transactions of the Royal Society of London B: Biological Sciences*, vol. 366, no. 1581, pp. 2989–2995, 2011.

[38] L. A. Jones and S. J. Lederman, *Human hand function*. Oxford University Press, 2006.

[39] S. J. Lederman and R. L. Klatzky, "Extracting object properties through haptic exploration," *Acta Psychologica*, vol. 84, no. 1, pp. 29 – 40, 1993. Tactile Pattern Recognition.

[40] G. Robles-De-La-Torre and V. Hayward, "Force can overcome object geometry in the perception of shape through active touch," *Nature*, vol. 412, pp. 445–448, 07 2001.

[41] J. Konstantinova, M. Li, G. Mehra, P. Dasgupta, K. Althoefer, and T. Nanayakkara, "Behavioral characteristics of manual palpation to localize hard nodules in soft tissues," *Biomedical Engineering, IEEE Transactions on*, vol. PP, no. 99, pp. 1–1, 2014.

[42] J. Morley, A. Goodwin, and I. Darian-Smith, "Tactile discrimination of gratings," *Experimental Brain Research*, vol. 49, no. 2, pp. 291–299, 1983.

[43] A. Jiang, G. Xynogalas, P. Dasgupta, K. Althoefer, and T. Nanayakkara, "Design of a variable stiffness flexible manipulator with composite granular jamming and membrane coupling," in *Intelligent Robots and Systems (IROS), 2012 IEEE/RSJ International Conference on*, pp. 2922–2927, Oct 2012.

[44] A. Jiang, A. Ataollahi, P. Dasgupta, K. Althoefer, and T. Nanayakkara, "A variable stiffness joint by granular jamming," in *ASME 2012 International Design Engineering Technical Conferences and Computers and Information in Engineering Conference*, pp. 267–275, August 2012.

[45] M. Haruno, D. M. Wolpert, and M. Kawato, "Mosaic model for sensorimotor learning and control," *Neural computation*, vol. 13, no. 10, pp. 2201–2220, 2001.

[46] V. C. Müller and M. Hoffmann, "What is morphological computation? on how the body contributes to cognition and control," *Artificial Life*, no. 2016/17, forthcoming.

[47] H. Hauser, R. M. Füchslin, and R. Pfeifer, "Morphological computation - the physical body as a computational resource," in *Opinions and Outlooks on Morphological Computation* (H. Hauser, R. M. Füchslin, and R. Pfeifer, eds.), ch. 20, pp. 226–244, Self-published, 2014.

[48] F. Iida, G. Gómez, and R. Pfeifer, "Exploiting body dynamics for controlling a running quadruped robot," in *ICAR'05. Proceedings., 12th International Conference on Advanced Robotics, 2005.*, pp. 229–235, IEEE, 2005.

[49] M. Ziegler, F. Iida, and R. Pfeifer, "Cheap" underwater locomotion: roles of morphological properties and behavioural diversity," *Proceedings of Climbing and Walking Robots*, 2006.

[50] P. Calvo and T. Gomila, *Handbook of cognitive science: An embodied approach*. Elsevier, 2008.

[51] R. H. Baayen, P. Milin, D. F. Đurđević, P. Hendrix, and M. Marelli, "An amorphous model for morphological processing in visual comprehension based on naive discriminative learning.," *Psychological review*, vol. 118, no. 3, p. 438, 2011.

[52] T. Trappenberg, *Fundamentals of computational neuroscience*. OUP Oxford, 2009.

[53] R. M. Füchslin, A. Dzyakanchuk, D. Flumini, H. Hauser, K. J. Hunt, R. H. Luchsinger, B. Reller, S. Scheidegger, and R. Walker, "Morphological computation and morphological control: steps toward a formal theory and applications," *Artificial Life*, vol. 19, no. 1, pp. 9–34, 2013.

[54] R. Pfeifer and G. Gómez, "Morphological computation–connecting brain, body, and environment," in *Creating Brain-Like Intelligence*, pp. 66–83, Springer, 2009.

[55] H. Hauser, A. J. Ijspeert, R. M. Füchslin, R. Pfeifer, and W. Maass, "Towards a theoretical foundation for morphological computation with compliant bodies," *Biological cybernetics*, vol. 105, no. 5-6, pp. 355–370, 2011.

[56] H. Hauser, A. J. Ijspeert, R. M. Füchslin, R. Pfeifer, and W. Maass, "The role of feedback in morphological computation with compliant bodies," *Biological cybernetics*, vol. 106, no. 10, pp. 595–613, 2012.

[57] G. Carbone, "Stiffness analysis and experimental validation of robotic systems," *Frontiers of Mechanical Engineering*, vol. 6, no. 2, pp. 182–196, 2011.

[58] N. Hogan, "Impedance control: An approach to manipulation, part i - theory," *Journal of Dynamic Systems, Measurement, and Control*, vol. 107, no. 1, pp. 1–7, 1985.

[59] N. Hogan, "Impedance control: An approach to manipulation: Part ii-implementation," *Journal of Dynamic Systems, Measurement, and Control*, vol. 107, no. 1, pp. 8–16, 1985.

[60] N. Hogan, "Impedance control: An approach to manipulation: Part iii-applications," *Journal of dynamic systems, measurement, and control*, vol. 107, no. 2, pp. 17–24, 1985.

[61] F. Bianchi, G. Bartoli, K. Shoar, M. R. A. Fernandez, V. Pereno, J. Zirjakova, A. Jiang, and T. Nanayakkara, "Adaptive internal impedance control for stable walking on uncertain visco-elastic terrains," in *2012 IEEE/RSJ International Conference on Intelligent Robots and Systems*, pp. 2465–2470, Oct 2012.

[62] T. McGeer, "Passive Dynamic Walking," *The International Journal of Robotics Research*, vol. 9, no. 2, pp. 62–82, 1990.

[63] S. Collins, A. Ruina, R. Tedrake, and M. Wisse, "Efficient bipedal robots based on passive-dynamic walkers," *Science*, vol. 307, no. 5712, pp. 1082–1085, 2005.

[64] R. Tedrake, T. W. Zhang, and H. S. Seung, "Learning to walk in 20 minutes," in *Proceedings of the Fourteenth Yale Workshop on Adaptive and Learning Systems*, vol. 95585, 2005.

[65] D. N. Beal, F. S. Hover, M. S. Triantafyllou, J. C. Liao, and G. V. Lauder, "Passive propulsion in vortex wakes," *Journal of Fluid Mechanics*, vol. 549, pp. 385–402, Feb. 2006.

[66] J. Liu and H. Hu, "Biological Inspiration: From Carangiform Fish to Multi-Joint Robotic Fish," *Journal of Bionic Engineering*, vol. 7, pp. 35–48, Mar. 2010.

[67] M. Ziegler, M. Hoffmann, J. P. Carbajal, and R. Pfeifer, "Varying body stiffness for aquatic locomotion," in *2011 IEEE International Conference on Robotics and Automation*, pp. 2705–2712, Ieee, May 2011.

[68] S. Tafazoli, S. E. Salcudean, K. Hashtrudi-Zaad, and P. D. Lawrence, "Impedance control of a teleoperated excavator," *Control Systems Technology, IEEE Transactions on*, vol. 10, no. 3, pp. 355–367, 2002.

[69] S. Salcudean, K. Hashtrudi-Zaad, S. Tafazoli, S. DiMaio, and C. Reboulet, "Bilateral matched impedance teleoperation with application to excavator control," *IEEE control systems*, vol. 19, no. 6, pp. 29–37, 1999.

[70] N. Hogan, "Control of contact in robots and biological systems," *IEEE Engineering in Medicine and Biology Magazine*, vol. 11, pp. 81–82, Dec 1992.

[71] A. De Luca, A. Albu-Schaffer, S. Haddadin, and G. Hirzinger, "Collision detection and safe reaction with the dlr-iii lightweight manipulator arm," in *Intelligent Robots and Systems, 2006 IEEE/RSJ International Conference on*, pp. 1623–1630, IEEE, 2006.

[72] K. Mouri, K. Terashima, P. Minyong, H. Kitagawa, and T. Miyoshi, "Identification and hybrid impedance control of human skin muscle by multi-fingered robot hand," in *Intelligent Robots and Systems, 2007. IROS 2007. IEEE/RSJ International Conference on*, pp. 2895–2900, IEEE, 2007.

[73] G. Aguirre-Ollinger, J. E. Colgate, M. A. Peshkin, and A. Goswami, "Active-impedance control of a lower-limb assistive exoskeleton," in *Rehabilitation Robotics, 2007. ICORR 2007. IEEE 10th International Conference on*, pp. 188–195, IEEE, 2007.

[74] Y. Yang, L. Wang, J. Tong, and L. Zhang, "Arm rehabilitation robot impedance control and experimentation," in *Robotics and Biomimetics, 2006. ROBIO'06. IEEE International Conference on*, pp. 914–918, IEEE, 2006.

[75] A. H. A. Stienen, E. E. G. Hekman, H. t. Braak, A. M. M. Aalsma, F. C. T. van der Helm, and H. van der Kooij, "Design of a rotational hydroelastic actuator for a powered exoskeleton for upper limb rehabilitation," *IEEE Transactions on Biomedical Engineering*, vol. 57, pp. 728–735, March 2010.

[76] A. Blank, A. M. Okamura, and L. L. Whitcomb, "Task-dependent impedance improves user performance with a virtual prosthetic arm," in *Robotics and Automation (ICRA), 2011 IEEE International Conference on*, pp. 2235–2242, May 2011.

[77] J. W. Sensinger and R. F. Weir, "User-modulated impedance control of a prosthetic elbow in unconstrained, perturbed motion," *Biomedical Engineering, IEEE Transactions on*, vol. 55, no. 3, pp. 1043–1055, 2008.

[78] S. Ikemoto, Y. Nishigori, and K. Hosoda, "Advantages of flexible musculoskeletal robot structure in sensory acquisition," *Artificial Life and Robotics*, vol. 17, no. 1, pp. 63–69, 2012.

[79] C. Smith, A. Villanueva, and S. Priya, "Aurelia aurita bio-inspired tilt sensor," *Smart Materials and Structures*, vol. 21, no. 10, p. 105015, 2012.

[80] C. Lucarotti, M. Totaro, A. Sadeghi, B. Mazzolai, and L. Beccai, "Revealing bending and force in a soft body through a plant root inspired approach," *Scientific reports*, vol. 5, 2015.

[81] F. Boyer, V. Lebastard, C. Chevallereau, S. Mintchev, and C. Stefanini, "Underwater navigation based on passive electric sense: New perspectives for underwater docking," *The International Journal of Robotics Research*, vol. 34, no. 9, pp. 1228–1250, 2015.

[82] M. Fend, R. Abt, M. Diefenbacher, S. Bovet, and M. Krafft, "Morphology and learning-a case study on whiskers," in *Proc. 8th Int. Conf. on the Simulation of Adaptive Behavior*, pp. 114–122, 2004.

[83] S. G. Nurzaman, U. Culha, L. Brodbeck, L. Wang, and F. Iida, "Active sensing system with in situ adjustable sensor morphology," *PLoS One*, vol. 8, no. 12, p. e84090, 2013.

[84] L. Lichtensteiger, "Towards optimal sensor morphology for specific tasks: Evolution of an artificial compound eye for estimating time to contact," in *Intelligent Systems and Smart Manufacturing*, pp. 138–146, International Society for Optics and Photonics, 2000.

[85] L. Lichtensteiger, "Evolving task specific optimal morphologies for an artificial insect eye," in *Morpho-functional machines: the new species*, pp. 41–57, Springer, 2003.

[86] N. Franceschini, J.-M. Pichon, C. Blanes, and J. Brady, "From insect vision to robot vision [and discussion]," *Philosophical Transactions of the Royal Society B: Biological Sciences*, vol. 337, no. 1281, pp. 283–294, 1992.

[87] M. E. Diamond, M. von Heimendahl, P. M. Knutsen, D. Kleinfeld, and E. Ahissar, "'where'and'what'in the whisker sensorimotor system," *Nature Reviews Neuroscience*, vol. 9, no. 8, pp. 601–612, 2008.

[88] M. Fend, S. Bovet, and R. Pfeifer, "On the influence of morphology of tactile sensors for behavior and control," *Robotics and Autonomous Systems*, vol. 54, no. 8, pp. 686–695, 2006.

[89] F. Iida and R. Pfeifer, "Sensing through body dynamics," *Robotics and Autonomous Systems*, vol. 54, no. 8, pp. 631–640, 2006.

[90] M. Reinstein and M. Hoffmann, "Dead reckoning in a dynamic quadruped robot based on multimodal proprioceptive sensory information," *IEEE Transactions on Robotics*, vol. 29, pp. 563–571, April 2013.

[91] J. J. Gibson, "The senses considered as perceptual systems.," 1966.

[92] R. Shadmehr, M. A. Smith, and J. W. Krakauer, "Error correction, sensory prediction, and adaptation in motor control," *Annual review of neuroscience*, vol. 33, pp. 89–108, 2010.

[93] Y. Hatwell, A. Streri, and E. Gentaz, *Touching for knowing: cognitive psychology of haptic manual perception*, vol. 53. John Benjamins Publishing, 2003.

[94] A. M. Smith, G. Gosselin, and B. Houde, "Deployment of fingertip forces in tactile exploration," *Experimental Brain Research*, vol. 147, no. 2, pp. 209–218, 2002.

[95] J. Paillard and M. Brouchon, "A proprioceptive contribution to the spatial encoding of position cues for ballistic movements," *Brain research*, vol. 71, no. 2-3, pp. 273–284, 1974.

[96] S.-J. Blakemore, C. D. Frith, and D. M. Wolpert, "Spatio-temporal prediction modulates the perception of self-produced stimuli," *Journal of cognitive neuroscience*, vol. 11, no. 5, pp. 551–559, 1999.

[97] M. Hoffmann, K. Štěpánová, and M. Reinstein, "The effect of motor action and different sensory modalities on terrain classification in a quadruped robot running with multiple gaits," *Robotics and Autonomous Systems*, vol. 62, no. 12, pp. 1790–1798, 2014.

[98] J. K. O'Regan and A. Noe, "A sensorimotor account of vision and visual consciousness-authors' response-acting out our sensory experience," 2001.

[99] J. J. Gibson, "The ecological approach to visual perception.," 1979.

[100] C. Bell, *The hand: its mechanism and vital endowments, as evincing design*, vol. 4. Bell & Daldy, 1865.

[101] J. M. Loomis and S. J. Lederman, "Tactual perception," *Handbook of perception and human performances*, vol. 2, p. 2, 1986.

[102] J. J. Gibson, "Observations on active touch.," *Psychological review*, vol. 69, no. 6, p. 477, 1962.

[103] C. E. Chapman, "Active versus passive touch: factors influencing the transmission of somatosensory signals to primary somatosensory cortex," *Canadian journal of physiology and pharmacology*, vol. 72, no. 5, pp. 558–570, 1994.

[104] S. J. Lederman and R. L. Klatzky, "Hand movements: A window into haptic object recognition," *Cognitive psychology*, vol. 19, no. 3, pp. 342–368, 1987.

[105] R. L. Klatzky, S. J. Lederman, and C. Reed, "There's more to touch than meets the eye: The salience of object attributes for haptics with and without vision.," *Journal of experimental psychology: general*, vol. 116, no. 4, p. 356, 1987.

[106] F. De Vignemont, H. H. Ehrsson, and P. Haggard, "Bodily illusions modulate tactile perception," *Current Biology*, vol. 15, no. 14, pp. 1286–1290, 2005.

[107] C. K. Loo, L. A. Hall, D. I. McCloskey, and M. J. Rowe, "Proprioceptive contributions to tactile identification of figures: dependence on figure size," *Behavioural brain research*, vol. 7, no. 3, pp. 383–386, 1983.

[108] M. T. Turvey and C. Carello, "Obtaining information by dynamic (effortful) touching," *Philosophical Transactions of the Royal Society of London B: Biological Sciences*, vol. 366, no. 1581, pp. 3123–3132, 2011.

[109] V. G. Macefield, "Physiological characteristics of low-threshold mechanoreceptors in joints, muscle and skin in human subjects," *Clinical and Experimental Pharmacology and Physiology*, vol. 32, no. 1-2, pp. 135–144, 2005.

[110] N. Wang, G. J. Gerling, R. M. Childress, and M. L. Martin, "Quantifying Palpation Techniques in Relation to Performance in a Clinical Prostate Exam," *IEEE Trans. on Information Technology in Biomedicine: a Publication of the IEEE Engineering in Medicine and Biology Society*, vol. 14, pp. 1088–97, July 2010.

[111] B. Hughes and G. Jansson, "Texture perception via active touch," *Human Movement Science*, vol. 13, no. 3–4, pp. 301 – 333, 1994.

[112] R. Bajcsy, "Active perception," *Proceedings of the IEEE*, vol. 76, pp. 966–1005, Aug 1988.

[113] J. Aloimonos, I. Weiss, and A. Bandyopadhyay, "Active vision," *International Journal of Computer Vision*, vol. 1, no. 4, pp. 333–356, 1988.

[114] A. Andreopoulos and J. Tsotsos, "A computational learning theory of active object recognition under uncertainty," *International Journal of Computer Vision*, vol. 101, no. 1, pp. 95–142, 2013.

[115] P. Boonvisut and M. C. Çavuşoğlu, "Identification and active exploration of deformable object boundary constraints through robotic manipulation," *The International journal of robotics research*, vol. 33, no. 11, pp. 1446–1461, 2014.

[116] O. Van der Meijden and M. Schijven, "The value of haptic feedback in conventional and robot-assisted minimal invasive surgery and virtual reality training: a current review," *Surgical endoscopy*, vol. 23, no. 6, pp. 1180–1190, 2009.

[117] S. A. Stansfield, "A robotic perceptual system utilizing passive vision and active touch," *The International journal of robotics research*, vol. 7, no. 6, pp. 138–161, 1988.

[118] J. M. Reales and S. Ballesteros, "Implicit and explicit memory for visual and haptic objects: Cross-modal priming depends on structural descriptions.," *Journal of Experimental Psychology: Learning, Memory, and Cognition*, vol. 25, no. 3, p. 644, 1999.

[119] P. K. Allen and K. S. Roberts, "Haptic object recognition using a multi-fingered dextrous hand," in *Robotics and Automation, 1989. Proceedings., 1989 IEEE International Conference on*, pp. 342–347, IEEE, 1989.

[120] S. Takamuku, G. Gomez, K. Hosoda, and R. Pfeifer, "Haptic discrimination of material properties by a robotic hand," in *2007 IEEE 6th International Conference on Development and Learning*, pp. 1–6, July 2007.

[121] V. Chu, I. McMahon, L. Riano, C. G. McDonald, Q. He, J. M. Perez-Tejada, M. Arrigo, N. Fitter, J. C. Nappo, T. Darrell, and K. J. Kuchenbecker, "Using robotic exploratory procedures to learn the meaning of haptic adjectives," in *Robotics and Automation (ICRA), 2013 IEEE International Conference on*, pp. 3048–3055, May 2013.

[122] A. M. Okamura and M. R. Cutkosky, "Feature detection for haptic exploration with robotic fingers," *The International Journal of Robotics Research*, vol. 20, no. 12, pp. 925–938, 2001.

[123] A. M. Okamura, M. L. Turner, and M. R. Cutkosky, "Haptic exploration of objects with rolling and sliding," in *Robotics and Automation, 1997. Proceedings., 1997 IEEE International Conference on*, vol. 3, pp. 2485–2490 vol.3, Apr 1997.

[124] S. A. Stansfield, "Haptic perception with an articulated, sensate robot hand," *Robotica*, vol. 10, pp. 497–508, 11 1992.

[125] R. Klatzky and C. L. Reed, "Haptic exploration," in *Scholarpedia of Touch*, pp. 177–183, Springer, 2016.

[126] S. Ballesteros, J. M. Reales, L. P. de Leon, and B. Garcia, "The perception of ecological textures by touch: does the perceptual space change under bimodal visual and haptic exploration?," in *First Joint Eurohaptics Conference and Symposium on Haptic Interfaces for Virtual Environment and Teleoperator Systems. World Haptics Conference*, pp. 635–638, March 2005.

[127] R. D. P. Wong, R. B. Hellman, and V. J. Santos, "Spatial asymmetry in tactile sensor skin deformation aids perception of edge orientation during haptic exploration," *IEEE Transactions on Haptics*, vol. 7, pp. 191–202, April 2014.

[128] D. Trivedi, C. D. Rahn, W. M. Kier, and I. D. Walker, "Soft robotics: Biological inspiration, state of the art, and future research," *Applied Bionics and Biomechanics*, vol. 5, pp. 99–117, Dec. 2008.

[129] A. G. Harrell and B. T. Heniford, "Minimally invasive abdominal surgery: lux et veritas past, present, and future," *The American Journal of Surgery*, vol. 190, no. 2, pp. 239 – 243, 2005.

[130] S. J. Lederman and R. L. Klatzky, "Sensing and displaying spatially distributed fingertip forces in haptic interfaces for teleoperator and virtual environment systems," *Presence: Teleoperators and Virtual Environments*, vol. 8, no. 1, pp. 86–103, 1999.

[131] K. J. Saunders, C. A. Pilgrim, and H. S. Pennypacker, "Increased Proficiency of Search in Breast Self-examination," *Cancer*, vol. 58, pp. 2531–7, Dec. 1986.

[132] J. Konstantinova, M. Li, V. Aminzadeh, P. Dasgupta, K. Althoefer, and T. Nanayakkara, "Force-velocity modulation strategies for soft tissue examination," in *Intelligent Robots and Systems (IROS), 2013 IEEE/RSJ International Conference on*, pp. 1998–2003, Nov 2013.

[133] P. Puangmali, K. Althoefer, L. D. Seneviratne, D. Murphy, and P. Dasgupta, "State-of-the-Art in Force and Tactile Sensing for Minimally Invasive Surgery," *IEEE Sensors Journal*, vol. 8, pp. 371–381, Apr. 2008.

[134] A. Samani, J. Zubovits, and D. Plewes, "Elastic moduli of normal and pathological human breast tissues: an inversion-technique-based investigation of 169 samples," *Physics in medicine and biology*, vol. 52, no. 6, p. 1565, 2007.

[135] L. M. McManus and R. N. Mitchell, *Pathobiology of Human Disease: A Dynamic Encyclopedia of Disease Mechanisms*. Elsevier, 2014.

[136] W. A. Woodward, E. A. Strom, S. L. Tucker, M. D. McNeese, G. H. Perkins, N. R. Schechter, S. E. Singletary, R. L. Theriault, G. N. Hortobagyi, K. K. Hunt, *et al.*, "Changes in the 2003 american joint committee on cancer staging for breast cancer dramatically affect stage-specific survival," *Journal of clinical oncology*, vol. 21, no. 17, pp. 3244–3248, 2003.

[137] R. Drake, A. W. Vogl, and A. W. Mitchell, *Gray's anatomy for students*. Elsevier Health Sciences, 2014.

[138] A. Z. Hajian and R. D. Howe, "Identification of the mechanical impedance at the human finger tip," *Journal of biomechanical engineering*, vol. 119, no. 1, pp. 109–114, 1997.

[139] K. Akazawa, T. E. Milner, and R. B. Stein, "Modulation of reflex emg and stiffness in response to stretch of human finger muscle.," *Journal of Neurophysiology*, vol. 49, no. 1, pp. 16–27, 1983.

[140] A. Ajoudani, S. B. Godfrey, M. Bianchi, M. G. Catalano, G. Grioli, N. Tsagarakis, and A. Bicchi, "Exploring teleimpedance and tactile feedback for intuitive control of the pisa/iit softhand," *Haptics, IEEE Transactions on*, vol. 7, no. 2, pp. 203–215, 2014.

[141] J. Winkel and K. Jørgensen, "Significance of skin temperature changes in surface electromyography," *European journal of applied physiology and occupational physiology*, vol. 63, no. 5, pp. 345–348, 1991.

[142] E. Kupa, S. Roy, S. Kandarian, and C. De Luca, "Effects of muscle fiber type and size on emg median frequency and conduction velocity," *Journal of Applied Physiology*, vol. 79, no. 1, pp. 23–32, 1995.

[143] T. E. Milner, C. Cloutier, A. B. Leger, and D. W. Franklin, "Inability to activate muscles maximally during cocontraction and the effect on joint stiffness," *Experimental Brain Research*, vol. 107, no. 2, pp. 293–305, 1995.

[144] A. Ajoudani, S. B. Godfrey, M. Catalano, G. Grioli, N. G. Tsagarakis, and A. Bicchi, "Teleimpedance control of a synergy-driven anthropomorphic hand," in *2013 IEEE/RSJ International Conference on Intelligent Robots and Systems*, pp. 1985–1991, IEEE, 2013.

[145] K. Nazarpour, A. H. Al-Timemy, G. Bugmann, and A. Jackson, "A note on the probability distribution function of the surface electromyogram signal," *Brain Research Bulletin*, vol. 90, pp. 88 – 91, 2013.

[146] F. Richer, M. Martinez, M. Robert, G. Bouvier, and J.-M. Saint-Hilaire, "Stimulation of human somatosensory cortex: tactile and body displacement perceptions in medial regions," *Experimental brain research*, vol. 93, no. 1, pp. 173–176, 1993.

[147] K. Horch, S. Meek, T. G. Taylor, and D. T. Hutchinson, "Object discrimination with an artificial hand using electrical stimulation of peripheral tactile and proprioceptive pathways with intrafascicular electrodes," *Neural Systems and Rehabilitation Engineering, IEEE Transactions on*, vol. 19, no. 5, pp. 483–489, 2011.

[148] F. Iida and S. G. Nurzaman, "Adaptation of sensor morphology: an integrative view of perception from biologically inspired robotics perspective," *Interface Focus*, vol. 6, no. 4, 2016.

[149] A. Jardón Huete and S. Martinez de la Casa, "Human centered mechatronics," in *Advanced Mechanics in Robotic Systems* (N. E. Nava Rodríguez, ed.), pp. 75–90, Springer London, 2011.

[150] G. Pratt and M. Williamson, "Series elastic actuators," in *Intelligent Robots and Systems 95. 'Human Robot Interaction and Cooperative Robots', Proceedings. 1995 IEEE/RSJ International Conference on*, vol. 1, pp. 399–406 vol.1, Aug.

[151] K. Bharadwaj, T. G. Sugar, J. B. Koeneman, and E. J. Koeneman, "Design of a Robotic Gait Trainer using Spring Over Muscle Actuators for Ankle Stroke Rehabilitation," *Journal of Biomechanical Engineering*, vol. 127, no. 6, p. 1009, 2005.

[152] R. Ham, T. Sugar, B. Vanderborght, K. Hollander, and D. Lefeber, "Compliant actuator designs," *Robotics Automation Magazine, IEEE*, vol. 16, no. 3, pp. 81–94, September.

[153] K. Koganezawa, T. Nakazawa, and T. Inaba, "Antagonistic control of multi-dof joint by using the actuator with non-linear elasticity," in *Robotics and Automation, 2006. ICRA 2006. Proceedings 2006 IEEE International Conference on*, pp. 2201–2207, May.

[154] B.-J. Yi and R. Freeman, "Geometric characteristics of antagonistic stiffness in redundantly actuated mechanisms," in *Robotics and Automation, 1993. Proceedings., 1993 IEEE International Conference on*, pp. 654–661 vol.2, May.

[155] K. Hollander, T. Sugar, and D. Herring, "Adjustable robotic tendon using a 'jack spring' trade;," in *Rehabilitation Robotics, 2005. ICORR 2005. 9th International Conference on*, pp. 113–118, June-1 July.

[156] R. Van Ham, M. Van Damme, B. Verrelst, B. Vanderbourght, and D. Lefeber, "Maccepa, a mechanically adjustable compliance and controllable equilibrium state actuator: a 3 dof joint with two independent compliances.," *Prikladnaya Mekhanika*, vol. 43, no. 4, pp. 130–142, 2007.

[157] G. A. Holzapfel and R. W. Ogden, *Biomechanics of soft tissue in cardiovascular systems*, vol. 441. Springer, 2014.

[158] V. Swaminathan, K. Mythreye, E. T. O'Brien, A. Berchuck, G. C. Blobe, and R. Superfine, "Mechanical stiffness grades metastatic potential in patient tumor cells and in cancer cell lines," *Cancer research*, vol. 71, no. 15, pp. 5075–5080, 2011.

[159] T. Schreiber, "Measuring information transfer," *Phys. Rev. Lett.*, vol. 85, pp. 461–464, Jul 2000.

[160] T. Ypma, "Historical development of the newton–raphson method," *SIAM Review*, vol. 37, no. 4, pp. 531–551, 1995.

[161] R. Hooke and T. A. Jeeves, ""direct search" solution of numerical and statistical problems," *J. ACM*, vol. 8, pp. 212–229, Apr. 1961.

[162] G. Carbone, E. Ottaviano, and M. Ceccarelli, "An optimum design procedure for both serial and parallel manipulators," *Proceedings of the Institution of Mechanical Engineers, Part C: Journal of Mechanical Engineering Science*, vol. 221, no. 7, pp. 829–843, 2007.

[163] A. Talasaz and R. Patel, "Telerobotic palpation for tumor localization with depth estimation," in *Intelligent Robots and Systems (IROS), 2013 IEEE/RSJ International Conference on*, pp. 463–468, Nov 2013.

[164] A. Graps, "An introduction to wavelets," *IEEE Computational Science and Engineering*, vol. 2, pp. 50–61, Summer 1995.

[165] J. C. Gwilliam, Z. Pezzementi, E. Jantho, A. M. Okamura, and S. Hsiao, "Human vs. robotic tactile sensing: Detecting lumps in soft tissue," in *Haptics Symposium, 2010 IEEE*, pp. 21–28, IEEE, 2010.

[166] K. P. Körding and D. M. Wolpert, "Bayesian decision theory in sensorimotor control," *Trends in cognitive sciences*, vol. 10, no. 7, pp. 319–326, 2006.

[167] M. Bianchi, P. Salaris, and A. Bicchi, "Synergy-based hand pose sensing: Optimal glove design," *The International Journal of Robotics Research*, vol. 32, no. 4, pp. 407–424, 2013.

[168] B. B. Edin and J. H. Abbs, "Finger movement responses of cutaneous mechanoreceptors in the dorsal skin of the human hand," *Journal of neurophysiology*, vol. 65, no. 3, pp. 657–670, 1991.

[169] D. F. Collins, K. M. Refshauge, G. Todd, and S. C. Gandevia, "Cutaneous receptors contribute to kinesthesia at the index finger, elbow, and knee," *Journal of Neurophysiology*, vol. 94, no. 3, pp. 1699–1706, 2005.

[170] A. Moscatelli, M. Bianchi, A. Serio, A. Terekhov, V. Hayward, M. O. Ernst, and A. Bicchi, "The change in fingertip contact area as a novel proprioceptive cue," *Current Biology*, vol. 26, no. 9, pp. 1159–1163, 2016.

Appendix A

Ethical approval

This study was approved by King's College London Bio medical Sciences, Medicine, Dentistry and Natural and Mathematical Sciences research ethics committee (REC Reference number BDM/11/12-20).

A.1 Information sheet and consent form

The information sheet and consent form provided for human participants for the experiments described in Chapter 3 are as following:

INFORMATION SHEET FOR PARTICIPANTS

REC Reference Number: **BDM/11/12-20**

YOU WILL BE GIVEN A COPY OF THIS INFORMATION SHEET

Human's finger muscle activity during palpation

We would like to invite you to participate in this original research project if you are more than 18 years old, and do not suffer from any motor diseases (ex. Parkinson's). Priority is given to visually impaired people and those who have prior training in fire fighting in low visibility conditions. You will be given a trial with auditory noise to decide whether to continue or not. You should only continue to participate if you want to; choosing not to take part will not disadvantage you in any way. Before you decide whether you want to take part, it is important for you to understand why the research is being done and what your participation will involve. Please take time to read the following information carefully and discuss it with others if you wish. Ask us if there is anything that is not clear or if you would like more information.

The main objective of the study is to understand how humans modulate the finger's stiffness during palpation through adduction and abduction controlled by the cocontraction of Flexor digitorum superficialis (FDS) and Extensor digitorum communis (EDC) muscle pair to detect and estimate the depth of the abnormality presented inside a soft silicon phantom using an index finger from the dominant hand. Each participant will be given 5 1-minute-period learning trials for each of three different phantom samples with a hard nodule embedded at different depths. Participant will be informed about the depth information of the nodule in each phantom sample. The electromyography (EMG) quantified the activity of each muscle will be captured. After all learning, each participant will be given a short break to prevent any muscle fatigue before continuing the experiment in the estimation phase. During the depth estimation phase, the participant is blindfolded to denial the visual perception and is presented with one from the three different phantom samples used during learning at a time. Participant is then asked to palpate the soft silicon phantom using the index finger from his/her dominant hand to estimate the depth of the hard nodule. During the whole experiment, the participant will be attached with the EMG sensors to capture the muscle's activity.

- The experiment will be conducted in (room number to be decided). An experiment will last for a maximum of 1hour.
- EMG sensors will be attached to FDS and EDC muscle pair in the anterior and posterior of the dominant forearm to capture their voluntary cocontraction for the whole duration throughout the experiment. Your skin will have to be cleaned with alcohol before attaching sensors. If your skin is allergic to alcohol, the experiment will not proceed. There are no known after-effects of attaching EMG sensors to the skin.
- To minimize fatigue you will receive a 1-minute break every 5 minutes. However, you can also request for breaks more often if you feel any discomfort.
- In the learning phase, the participant is asked to explore the soft silicon phantom using the index finger for 5 trials with maximum 1 minute per trial for each phantom. The participant can stop before 1 minute mark if they feel confident about the experience collected.
- In the estimation phase, the participant is blindfolded and asked to palpate one of the three phantom samples used during the learning phase to estimate the depth of the nodule.
- Please wear loose clothing so that your skin can be easily cleaned and above mentioned sensors can be easily attached to the skin. We will take adequate precautions to cover your clothes to prevent any stains due to alcohol. You will also be given the option to wear a dress made available during the experiment.
- You have to wear laboratory suitable blindfolding mask in the 2nd phase of the experiment.
- You can withdraw the data up to one week from completion of the study. If you have any queries, please directly contact the principal investigator: Dr. Thrishantha Nanayakkara, Email: thrish.antha@kcl.ac.uk
- We will strictly follow the provisions of the Data Protection Act 1998, whereby, we will retain only the anonymised data such as handedness, sex, age for official records. They will be shared only among the researchers involved in this study.

Are you are happy to be contacted about participation in future studies? Yes ☐ No ☐

Your participation in this study will not be affected should you choose not to be re-contacted.

If you would like more information, please contact **Dr. Thrishantha Nanayakkara**
Email: thrish.antha@kcl.ac.uk
Telephone: 020-7848-2256,
Postal address: Room 1.23, Strand Building
Division of Engineering
King's College, University of London
Strand
London WC2R 2LS

Please complete this form after you have read the Information Sheet and/or listened to an explanation about the research.

Title of Study: Human's finger muscle activity during palpation

King's College Research Ethics Committee Ref: BDM/11/12-20

- **Thank you for considering taking part in this research. The person organising the research must explain the project to you before you agree to take part.**
- **If you have any questions arising from the Information Sheet or explanation already given to you, please ask the researcher before you decide whether to join in. You will be given a copy of this Consent Form to keep and refer to at any time.**
- **You can withdraw your data within one week from completion of the study.**
- **I understand that if I decide at any time during the research that I no longer wish to participate in this project, I can notify the researchers involved and withdraw from it immediately without giving any reason. *Yes* ☐ *No* ☐**
- **I consent to the processing of my personal information for the purposes explained to me. I understand that such information will be handled in accordance with the terms of the Data Protection Act 1998. *Yes* ☐ *No* ☐**
- ***Are you are happy to be contacted about participation in future studies? Yes* ☐ *No* ☐**

Participant's Statement:

I _____

agree that the research project named above has been explained to me to my satisfaction and I agree to take part in the study. I have read both the notes written above and the Information Sheet about the project, and understand what the research study involves.

Signed **Date**

***Are you are happy to be contacted about participation in future studies? Yes* ☐ *No* ☐**

RESEARCHER

I undertake to abide by accepted ethical principles and appropriate code(s) of practice in carrying out this study. The information supplied above is to the best of my knowledge accurate. I have read the Application Guidelines and clearly understand my obligations and the rights of participants, particularly in so far as to obtaining valid consent. I understand that I must not commence research with human

participants until I have received full approval from the ethics committee.

Signature …… **Date**……

STUDENT PROJECTS (including PhD) – SUPERVISOR AUTHORISATION

I confirm that I have read this application and will be acting as the student researcher's supervisor for this project. The proposal is viable and the student has appropriate skills to undertake the research. The Information Sheet and recruitment procedures for obtaining informed consent are appropriate and the ethical issues arising from the project have been addressed in the application. I understand that research with human participants must not commence without full approval from the ethics committee.

Name of Supervisor:

Signature …… **Date**……

MEDICAL SUPERVISION (if appropriate)

Name of Medical Supervisor:

Medical Supervisor's MDU/MPS (or other insurance provider) number:

……

Signature of Medical Supervisor:

…… **Date**……..

CONTACT DETAILS Give the details of the individual who should receive all correspondence concerning the application. Correspondence will normally be sent for the attention of the researcher. It is the responsibility of the researcher (and contact if different) to forward all copies of correspondence to the appropriate parties as required. Students should ensure that their supervisor is provided with copies of all correspondence.

Name: Thrishantha Nanayakkara

Full postal address:
Room 1.23, Strand Building
Division of Engineering
King's College, University of London
Strand
London WC2R 2LS

Telephone number: Tel: 020 7 848 2256

Email: thrish.antha@kcl.ac.uk

Please note that notification that approval is due to lapse is only sent to projects which are approved for two years or more (one year approvals will not be sent reminders and will need to remember to apply for an extension if a longer period of approval is required)